Exoplanets of low-mass stars

(mostly M dwarfs)

Today : **Advantages & Difficulties**

Friday : **Individual systems & Statistical properties**

Xavier Bonfils

M dwarfs

They are the most abundant stars in our Galaxy…
~70% of stars are M dwarfs

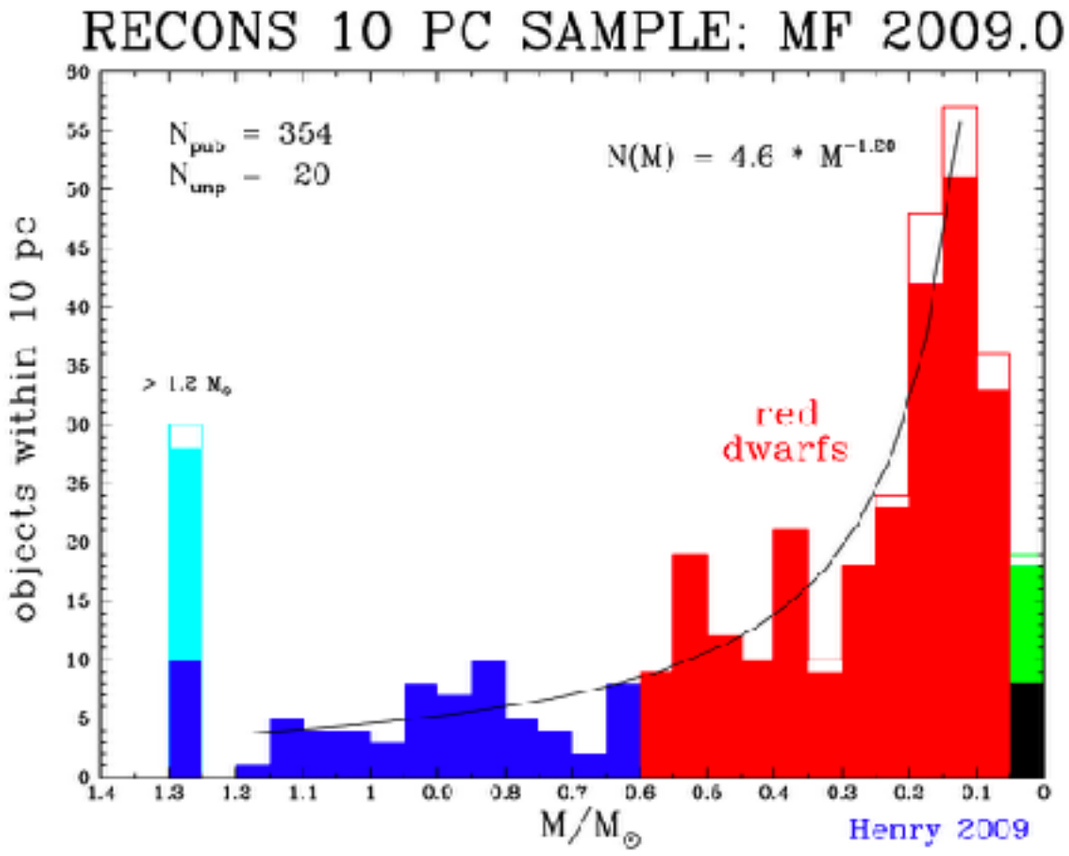

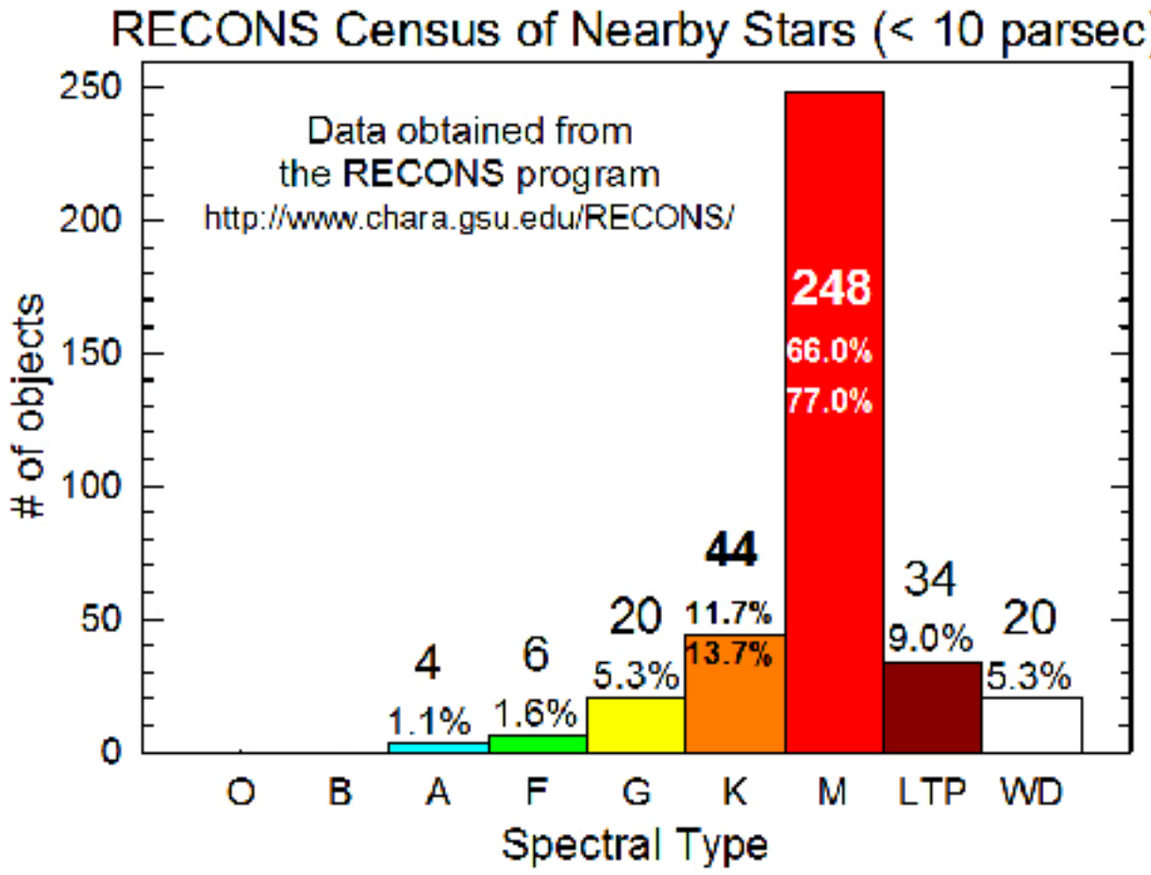

… and in other galaxies too (Dokkum & Conroy; 2010, Nat. 468, 940)

Xavier Bonfils

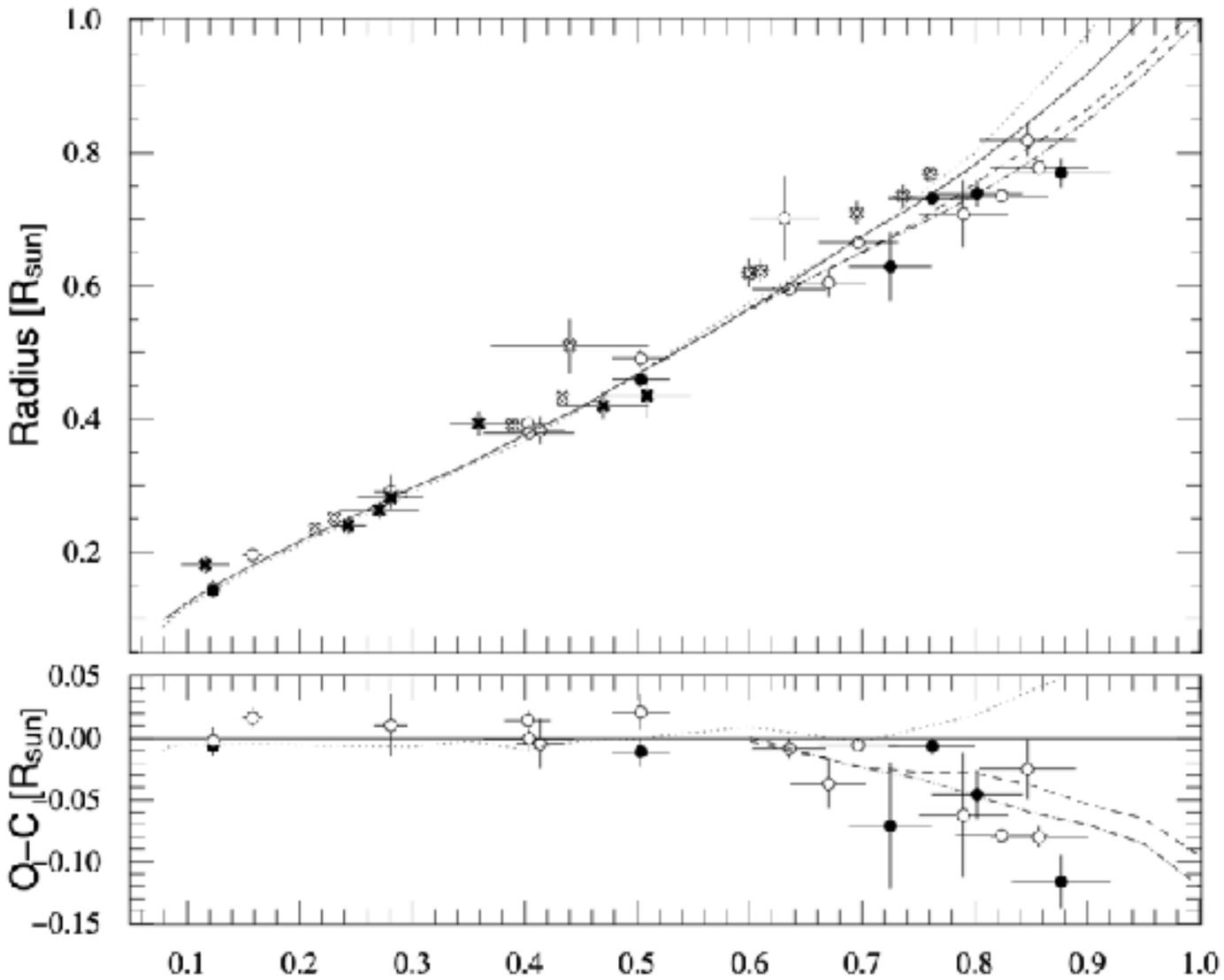

Fig. 8. Mass-radius relationship – masses and radii superimposed on 5 Gyr isochrones theoretical models (Baraffe et al. 1998). Our results appear as filled circles. Other long baseline interferometry measurements come from PTI (Lane et al. 2001), VLTI (Ségransan et al. 2003) and CHARA-FLUOR: Boyajian et al. (2008), di Folco et al. (2007), Kervella et al. (2008) and Berger et al. (2006) for GJ15A, all as empty circles. Solar metallicity with $L_{\rm mix} = 1.0H_{\rm P}$ (solid), $L_{\rm mix} = 1.5H_{\rm P}$ (dash) and $L_{\rm mix} = 1.9H_{\rm P}$ (dashdot) are shown as well as a metal deficient, [M/H] = −0.5 model with $L_{\rm mix} = 1.0H_{\rm P}$ (dot). Only radii measurements better than 10% are displayed. Solar-neighbourhood eclipsing binary measurements are represented as empty crosses, while OGLE-T transiting binaries are represented in filled crosses. Only residuals from long-baseline interferometry results are displayed.

M dwarfs

- low-mass stars

  $0.07\ \mathrm{M}_\odot \leq\ M_\star\ \leq 0.6\ \mathrm{M}_\odot$

- small

  $0.1\ \mathrm{R}_\odot\ \leq\ R_\star\ \leq\ 0.5\ \mathrm{R}_\odot$

(Demory et al. 2009, A&A 505, 205; see also Baraffe & Chabrier 1996, ApJ 461, 51)

Xavier Bonfils

M dwarfs

Lacaille 9352 (HD 217987, Gliese 887) is the brightest M dwarf with V = 7.32 mag

This is ~ limit of naked eye sensitivity, none of the star we see when gazing the sky are M dwarf (!)

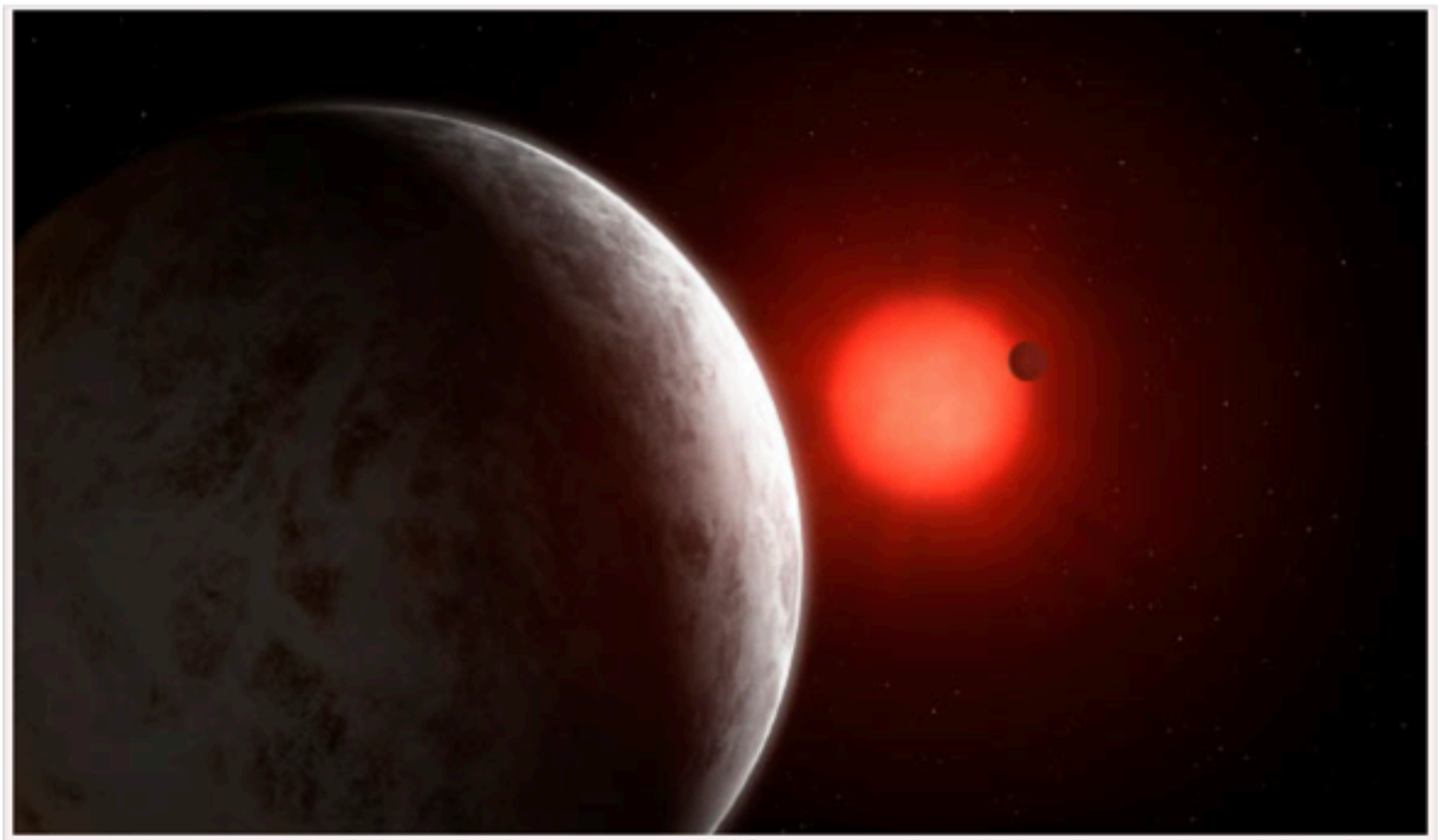

An artist's impression of the multiplanetary system of super-Earths orbiting the nearby red dwarf star Lacaille 9352. Image credit: Mark Garlick.

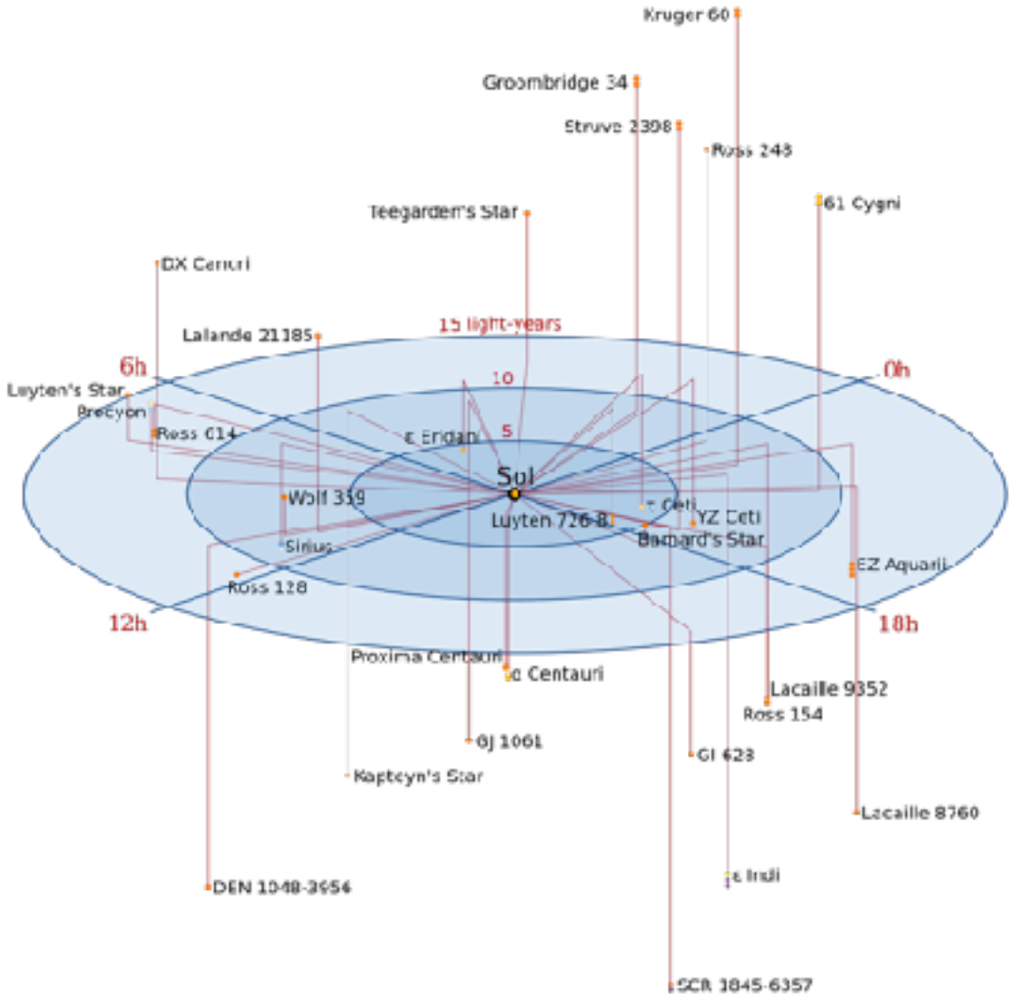

Jeffers et al. (2020)

M dwarfs

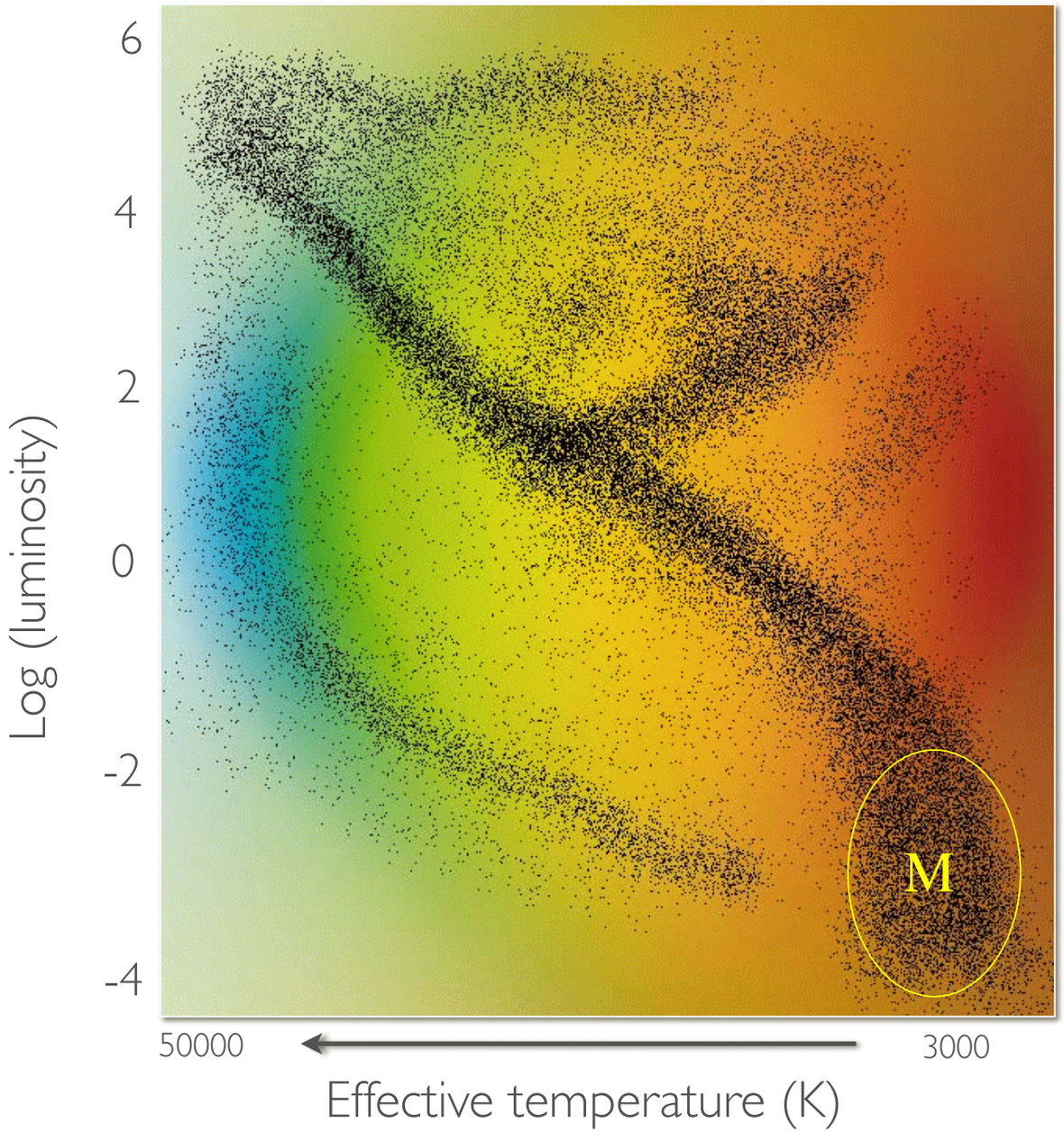

- low temperature

  $2100\ K\ \leq\ T_{eff}\ \leq\ 3800\ K$

- intrinsically faint

  $5.10^{-4}\ \mathrm{L}_{\odot}\ \leq\ L_{\star}\ \leq\ 0.1\ \mathrm{L}_{\odot}$

M dwarfs

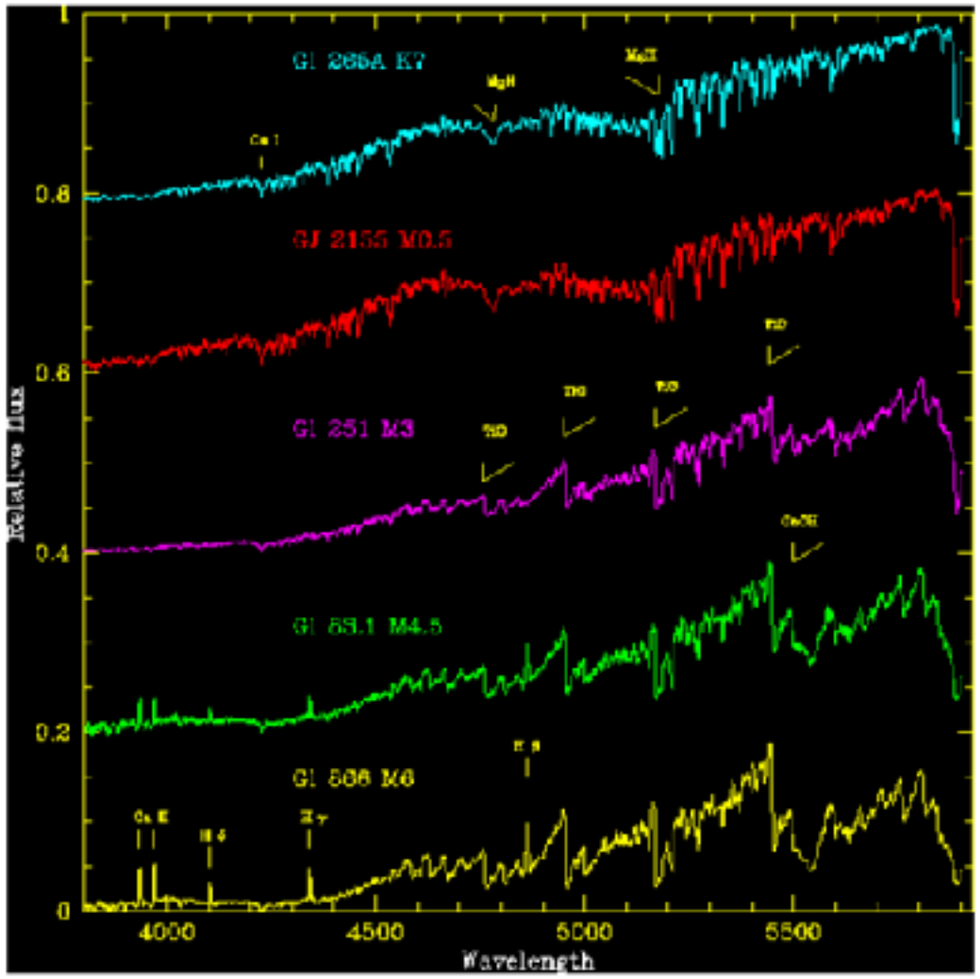

Figure II.1: *An M-dwarf spectral sequence for the blue-green region covered by the original MK classification scheme.*

Worth noting that M dwarfs are *actually* defined on how their spectra look like…

Copied from https://www.stsci.edu/~inr/

Spectral class M is characterised by the presence of strong absorption bands due to the diatomic molecule titanium oxide, TiO (Morgan, Keenan \& Kellman, 1943). The original classification scheme was based on photographic spectra of the blue-green region of the spectrum, reflecting the technology available at the time. At that tine, only a few M dwarfs were known sufficiently bright for high signal-to-noise spectroscopy, and all of those also have bright absolute magnitudes. As a result, while the M giant sequence was defined to spectral types M6, the original MK system extends only to M2 for main sequence stars. Another consequence of choosing (or being forced to choose) the blue-green region of the spectrum for classification purposes concerns TiO absorption: while M0 is formally defined as marking the onset of TiO absorption at blue-green wavelengths, absorption bands due to that molecule are already strong at red wavelengths. Thus, K7 and even K5 dwarfs can have noticed TiO 7050\AA absorption.

M dwarfs

They emits most in the infrared…
… and might thus be better measured at these wavelengths

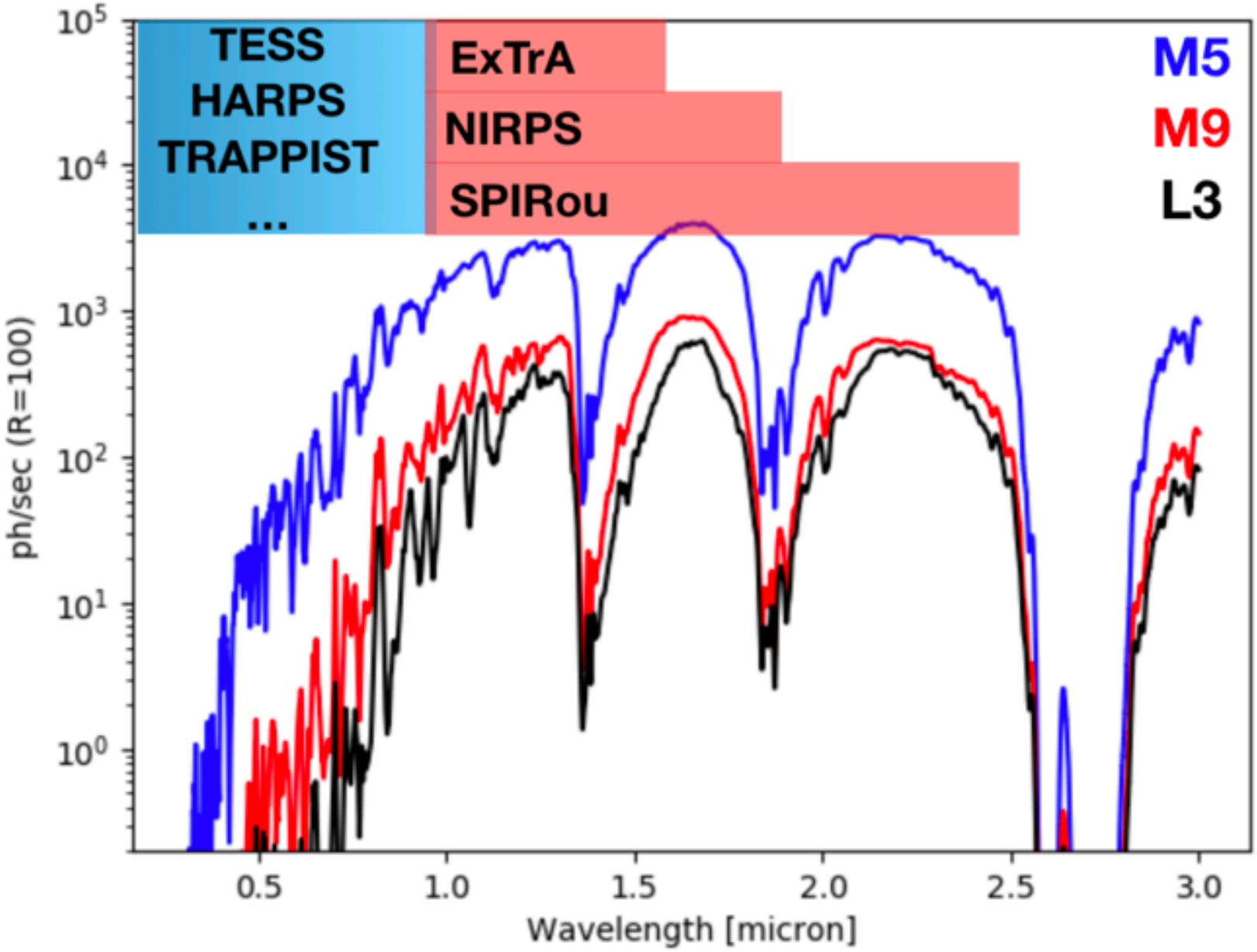

Motivations

- Dominant stellar (and possibly planetary) population of the Galaxy

- We see a different outcome of the planetary formation and we, therefore, probe the sensitivity of the planet formation to different conditions

- But… they are also practical targets…

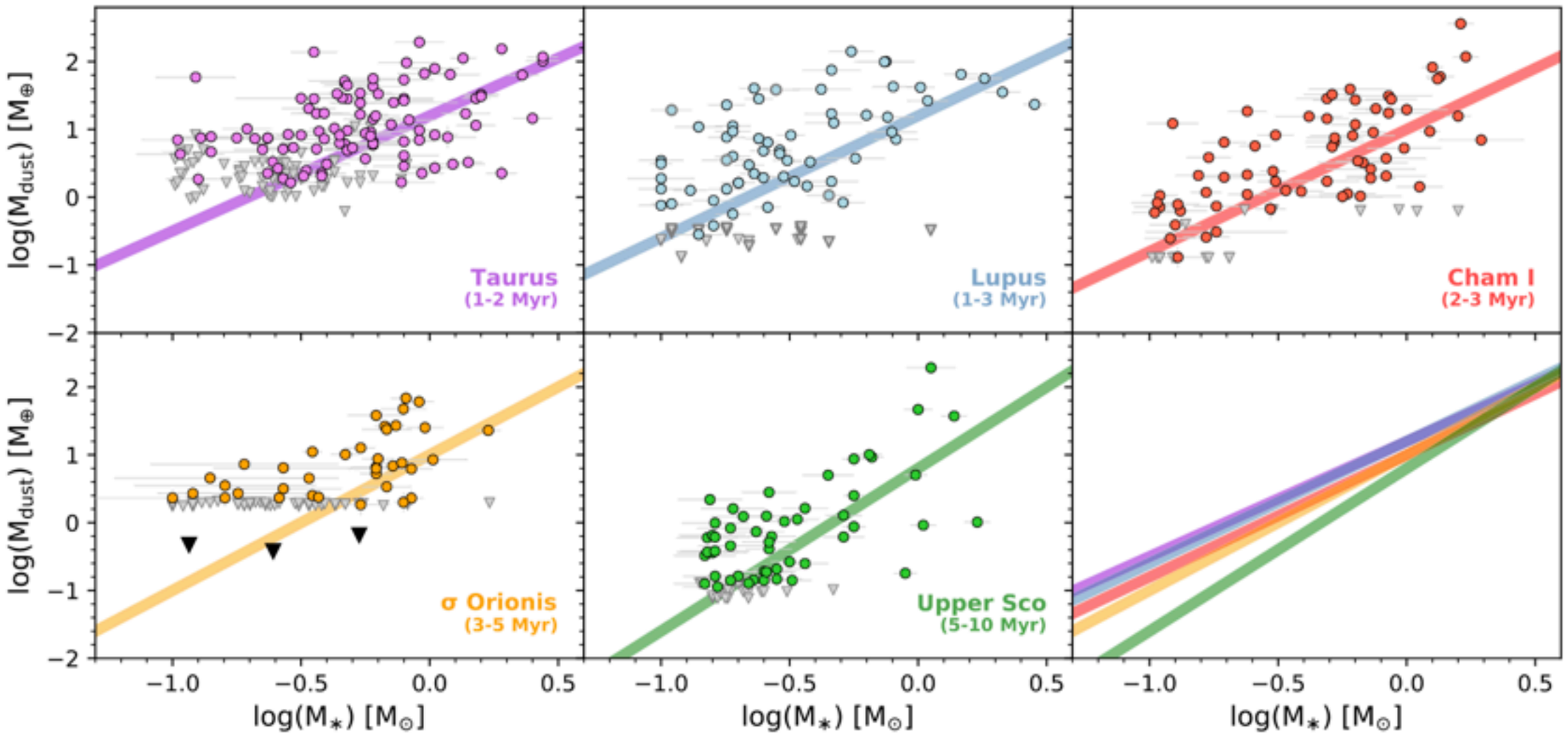

Figure 7. Disk dust mass ($M_{\rm dust}$) as a function of stellar mass (M_*) for disk populations in five star-forming regions with ages spanning the disk dispersal timescale (~1–10 Myr). Colored circles are (sub-)millimeter continuum detections and gray triangles are 3σ upper limits. For σ Orionis, the black triangles indicate 3σ upper limits from stacks of the non-detections in three stellar mass bins. For Lupus, the 20 sources with unknown stellar masses that were included in the analysis via an MC method (see Ansdell et al. 2016) are given representative values and identified by thick gray outlines. For each region, the solid lines show the Bayesian linear regression fits to the data, which take into account upper limits, intrinsic scatter, and measurement errors on both axes (Kelly 2007). The lower right panel compares the fits in all five regions, illustrating the ~1 dex difference in $M_{\rm dust}$ between the youngest and oldest regions at low stellar masses, and the convergence in $M_{\rm dust}$ at high stellar masses.

Lower-mass stars have lower-mass disks, and shorter disk lifetimes

See also Pascucci et al. (2016) : $M_{\rm dust} \propto (M_\star)^{1.3-1.9}$

Early targets

The 1st known claim for an exoplanet discovery is around 70 Oph (not a M dwarf) : Jocob et al. (1855, MRAS)

On certain Anomalies presented by the Binary Star 70 Ophiuchi.
By Capt. W. S. Jacob, Madras Astronomer.

The following, and probably more famous, was a planet around the M dwarfs Barnard's star (and the next around the M dwarfs Lalande 21185)

van de Kamp (1963) : astrometric discovery of 1.7 Mjup planet questioned by Gatewood (1973)

If some doubts persisted after the dispute, the possible planets were excluded with more recent HST astrometry.

With this story, astrometry did lost some credit as a discovery method… If not redeemed by now, it will be with GAIA. Perryman et al. (2014, ApJ 797, 14) predict >70k planets after a 10yr mission (!)

Barnard's star remains prone to false positive… (see claims by Ribas et al. 2018, Nat 563, 365); disputed to be a 1-yr alias by Lubin et al. 2021, AJ 162, 61)

They have always been in planet search samples… GJ876b, 1st M-dwarf planet in 1998 Marcy et al. (1998); Delfosse et al. (1998)

Practical motivations

Xavier Bonfils

Advantages for velocimetry

$$K_\star = \left(\frac{G}{a(1-e^2)}\right)^{1/2} \frac{M_p \sin i}{(M_\star + M_p)^{1/2}}$$

For equal semi-major axes…. K is **1.3x** for a **0.60x** lower-mass stars

……**3.8x**……**0.07x**…….

$$K_\star = \left(\frac{2\pi G}{P}\right)^{1/3} \frac{M_p \sin i}{(M_\star + M_p)^{2/3}} \frac{1}{(1-e^2)^{1/2}}$$

For equal orbital periods…… K is **1.4x** for a **0.60x** lower-mass stars

……**4.6x**……**0.07x**…….

Xavier Bonfils

Advantages for velocimetry

At same insolation / equilibrium temperature ?

$$T_p = T_\star (1-A)^{1/4} \sqrt{\frac{R_\star}{2a}}$$

$$a = \frac{1}{2} \frac{R_\star}{T_\star^2} T_p^2 \sqrt{1-A}$$

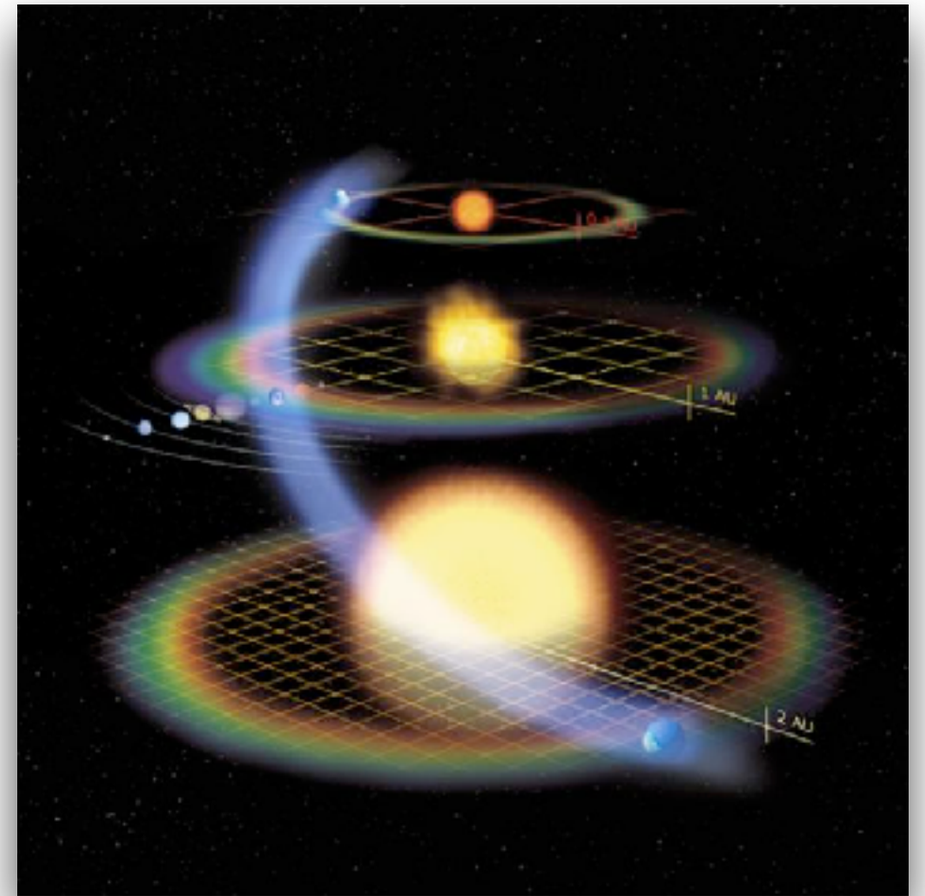

Planet is **4x** closer for a **M0** ($R_\star = 0.6 R_\odot ; T_\star = 3\,800 K$) star
…….75**x**……**M9** ($R_\star = 0.08 R_\odot ; T_\star = 2\,100 K$)…

Advantages for velocimetry

$$K_1 = \frac{28.4329\,\mathrm{m\,s^{-1}}}{\sqrt{1-e^2}} \frac{m_2 \sin i}{M_{\mathrm{Jup}}} \left(\frac{m_1+m_2}{M_\odot}\right)^{-1/2} \left(\frac{a}{1\,\mathrm{AU}}\right)^{-1/2}$$

$$K_1 = \frac{28.4329\,\mathrm{m\,s^{-1}}}{\sqrt{1-e^2}} \frac{m_2 \sin i}{M_{\mathrm{Jup}}} \left(\frac{m_1+m_2}{M_\odot}\right)^{-2/3} \left(\frac{P}{1\,\mathrm{yr}}\right)^{-1/3}$$

	a [AU]	Sun [m/s]	M0 (0.60M⊙) [m/s]	M8 (0.07M⊙) [m/s]
hot-Jupiter	0.05	127	165	483
Jupiter	5.2	12.5	16	48
hot-Neptune	0.05	6.8	8.8	26
Earth	1	0.09	0.12	0.34
Temperate Jupiter		28	76	954
Temperate Earth		0.09	0.24	3

Xavier Bonfils

Advantages for transit photometry

$$\delta = \frac{\pi R_p^2}{\pi R_\star^2} \qquad\qquad Pr \propto \frac{R_\star}{a}$$

Everything else equal… δ is **2.8x** for a **0.60x** smaller stars

……**100x**……**0.10x**……

Everything else equal… Pr **decreases** linearly with smaller stars

	a [AU]	Sun [mmag];%	M0 (0.60R⊙) [mmag];%	M8 (0.10R⊙) [mmag];%
hot-Jupiter	0.05	10 ; 9	30 ; 6	100 ; 1
Jupiter	5.2	10 ; <0.1	30 ; 0.05	100 ; <0.01
hot-Neptune	0.05	1.5; 9	3.5; 6	13 ; 1
Earth	1	0.084; <0.5	0.2; 0.3	8 ; <0.05

Advantages for astrometry

$$\alpha[arcsec] = \frac{M_p}{M_\star}\frac{a[AU]}{d[parscec]}$$

Everything else equal… α is 1.7x for a 0.60x lower-mass stars
……14x……0.07x……

$\sigma_{\mathrm{Hipparcos}} \sim 1\,\mathrm{mas}$ $\sigma_{\mathrm{Gaia}} \sim 25\,\mu\mathrm{as}$

@10pc	a [AU]	Sun [μas]	M0 (0.60R⊙) [μas]	M8 (0.10R⊙) [μas]
hot-Jupiter	0.05	1	1.7	14
Jupiter	5.2	500	850	7000
Earth	1	0.3	0.5	4.2

Xavier Bonfils

Advantages for characterization

Imagery ? (& Characterization)

Contrast ratio is more favorable, both in luminosity (for imagery or occultation spectroscopy) or surface ratio (for transmission spectroscopy)

μ-lensing ?

The lenses are distributed +/- like the stars in the Galaxy, and therefore tend to be M dwarfs.

Exoplanet Science Strategy (2018)
National Academy of Science (US)

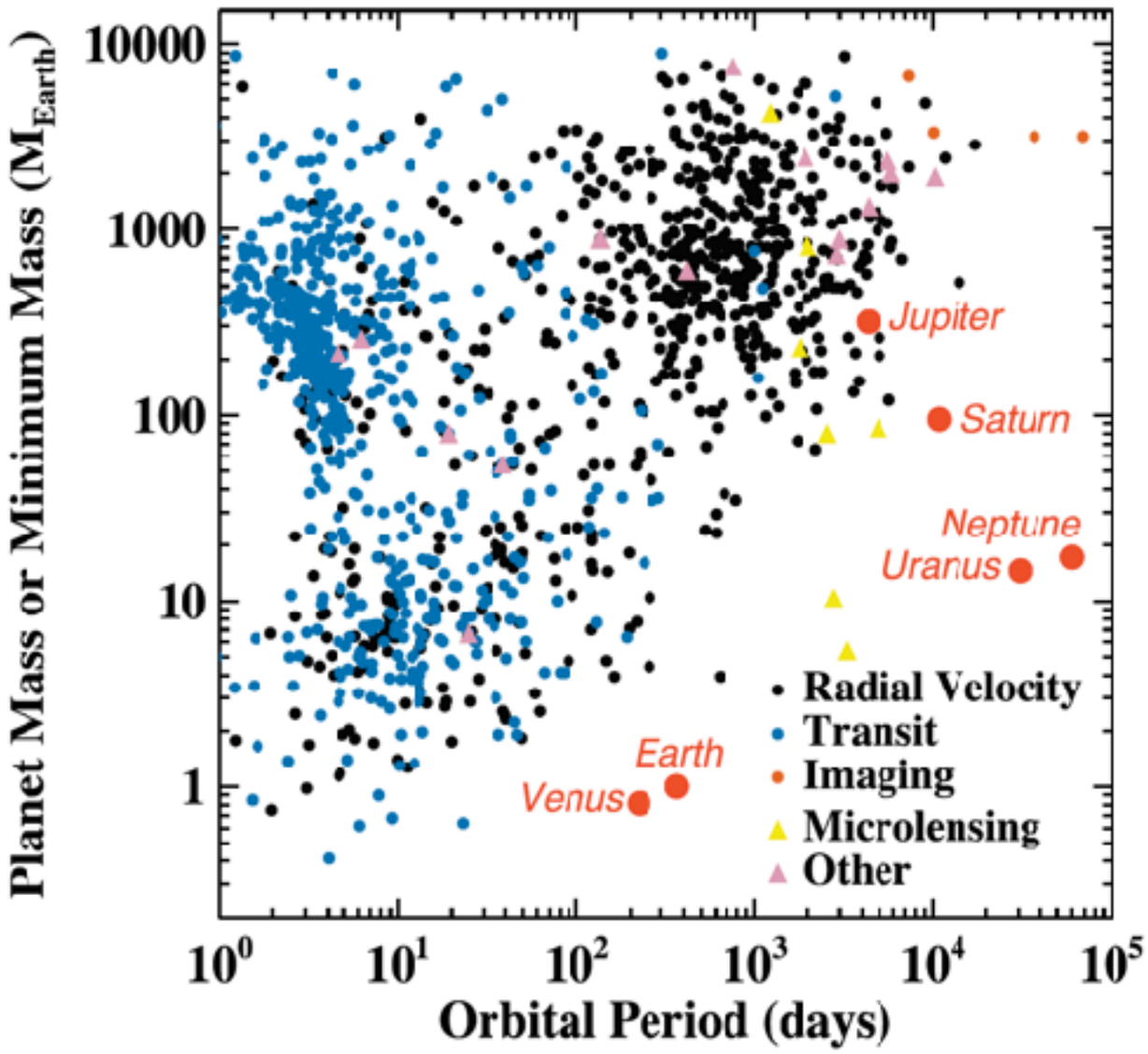

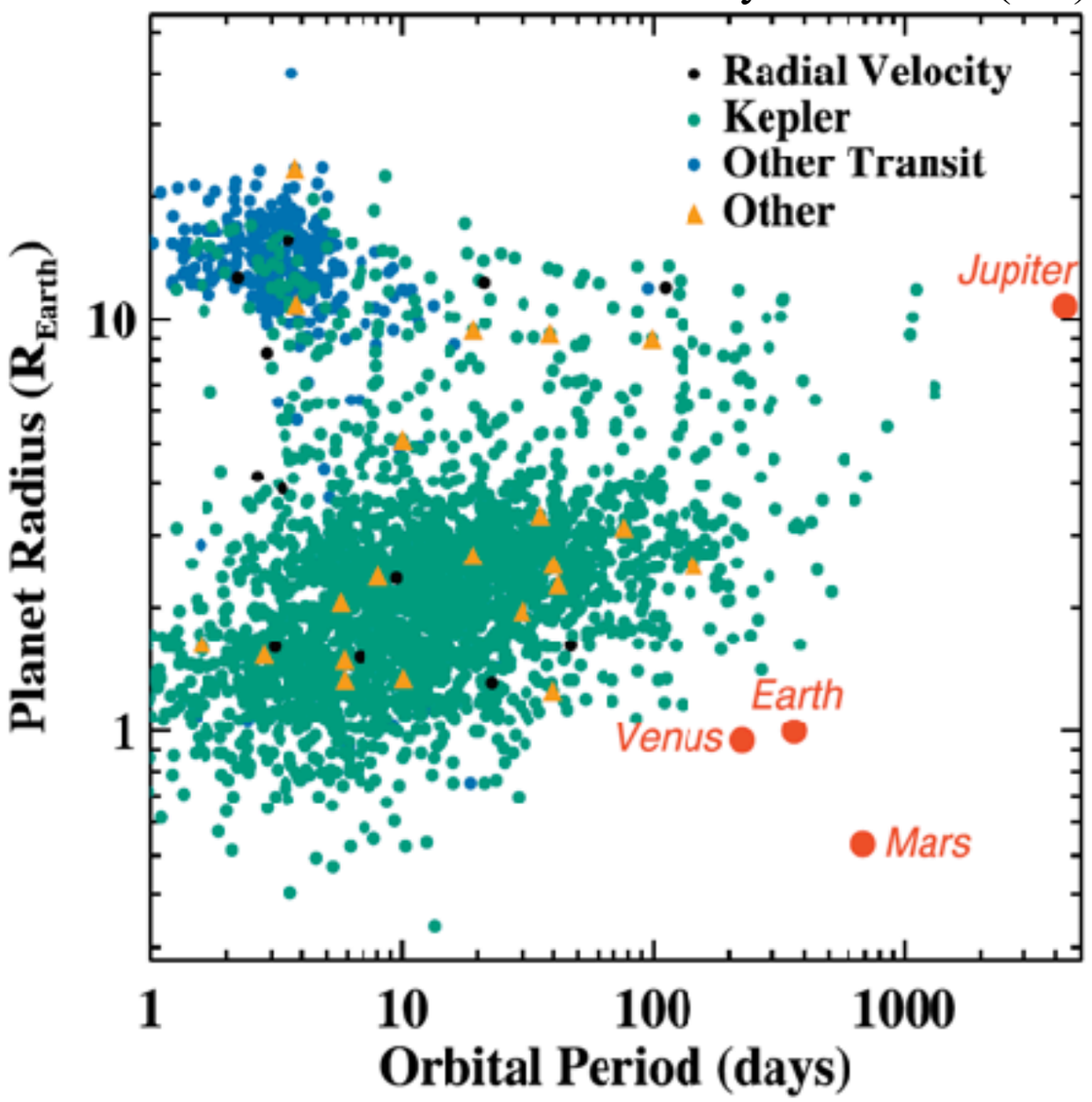

Earth-mass / Earth-size regime is probed by RV & Transit methods

Xavier BONFILS

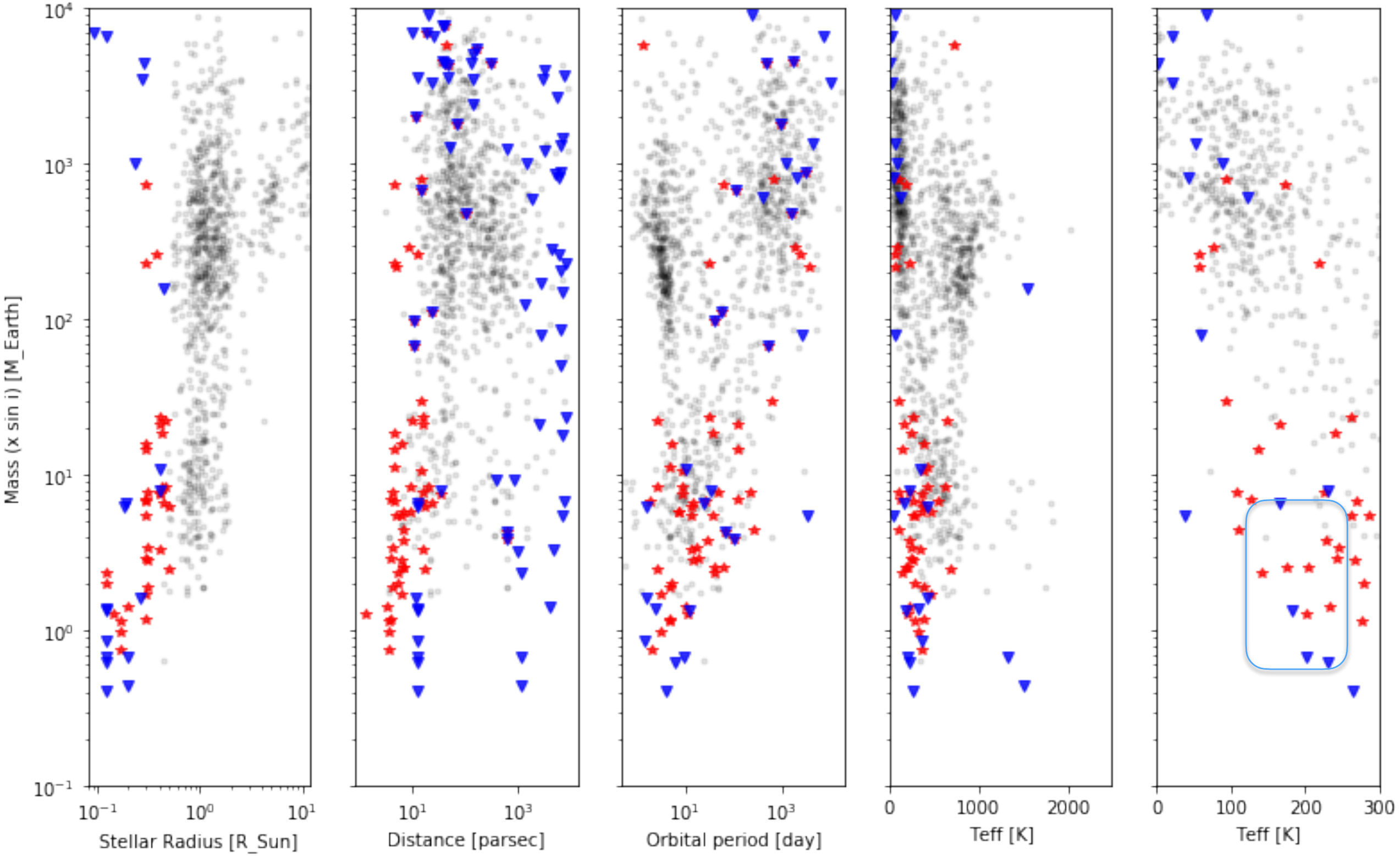

Xavier BONFILS

Drawbacks

Xavier Bonfils

Faint stars

1st and foremost : **they are faint**…

from a few % (M0) to $10^{-4} L_{\odot}$ (M9)

@ equal distances, M dwarfs require $10^2 - 10^4 \times$ higher collecting power compared to G stars

Since M dwarfs are more numerous, they tend to be close though… but only by a factor $10^{1/3} \sim 2 \times$ … and, therefore, not enough to significantly change how faint they are compare to Gs

⇒the low-luminosity penalty is comparable to the advantages highlighted earlier (!)

If signal gets a boost toward lower-mass, smaller stars, photon noise gets a boost too…

An example w/ Trappist-1

- Smallest ($R_\star = 0.12 R_\odot$), lowest-mass ($M_\star = 0.08 M_\odot$), coolest ($T_\star = 2'550 K$) planet host
- 7 planets $0.75 - 1.1\ R_\oplus; 0.41 - 1.4\ M_\oplus; 0.13 - 4.3\ S_\oplus$
- A scaled Earth would be between planet *d* and planet *e* (@ 0.023 AU)
- A priori transit prob (for such scaled Earth) ~ 2%; transit depth $\delta = 0.65\,\%$; $K_1 = 5\ m/s$
- For comparison, Earth around Sun : $p < 0.5\,\%$; $\delta = 0.0084\,\%$; $K_1 = 0.09\ m/s$
- V= 19 mag; and no RV confirmation yet…
- Masses were obtained w/ TTVs
- Even for transit photometry, the (S/N) cost benefit is little favorable to small stars

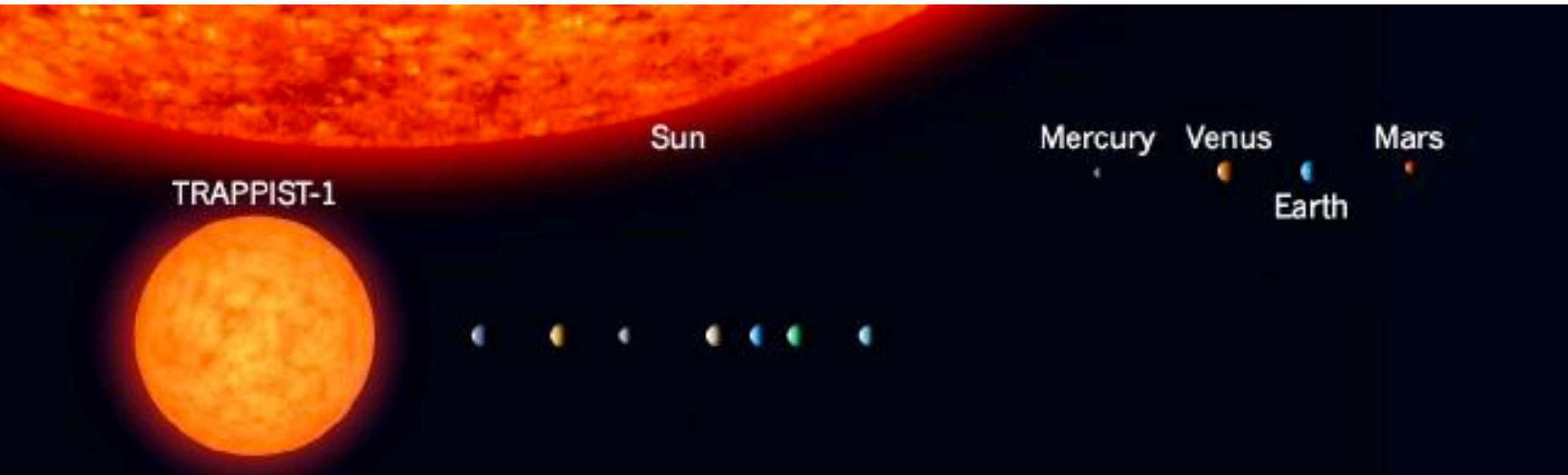

Noise regimes

- fundamental noise (photon noise)
+ white noise (Ron, dark…)

- systematics, correlated noise (floor noise)

- Instrumental (calibration, stability)
- Astrophysical scene (stellar activity, unaccounted effects)
- Atmosphere, astrometeorological conditions

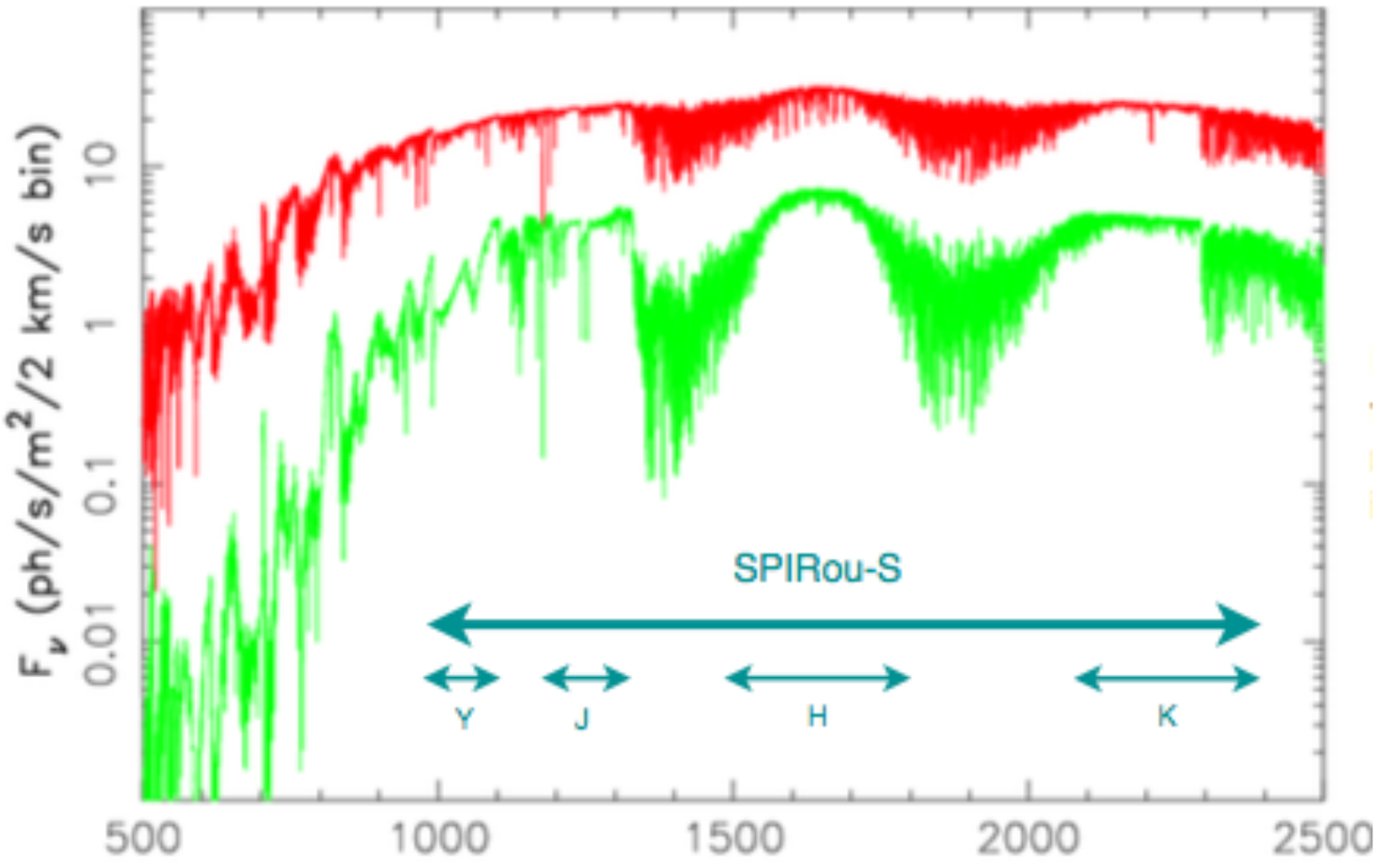

Infrared Velocimetry

SPIRou

carmenes

NIRPS
LOOKING FOR BLUE PLANETS AROUND RED STARS

HPF

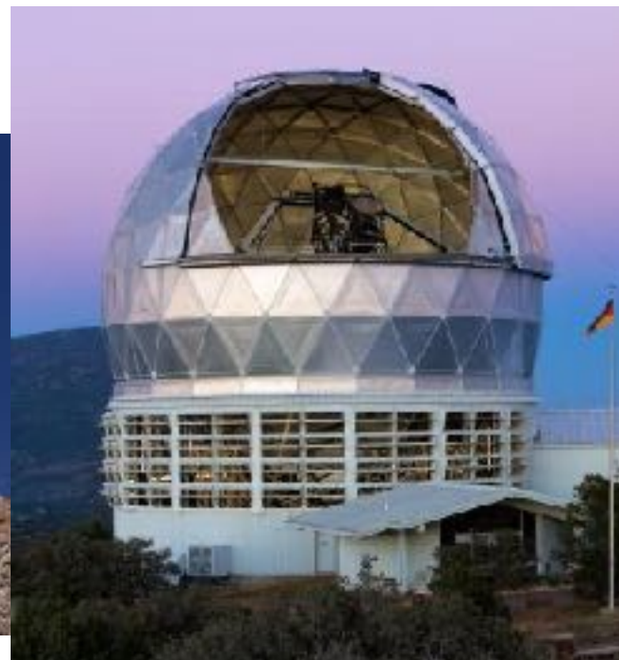

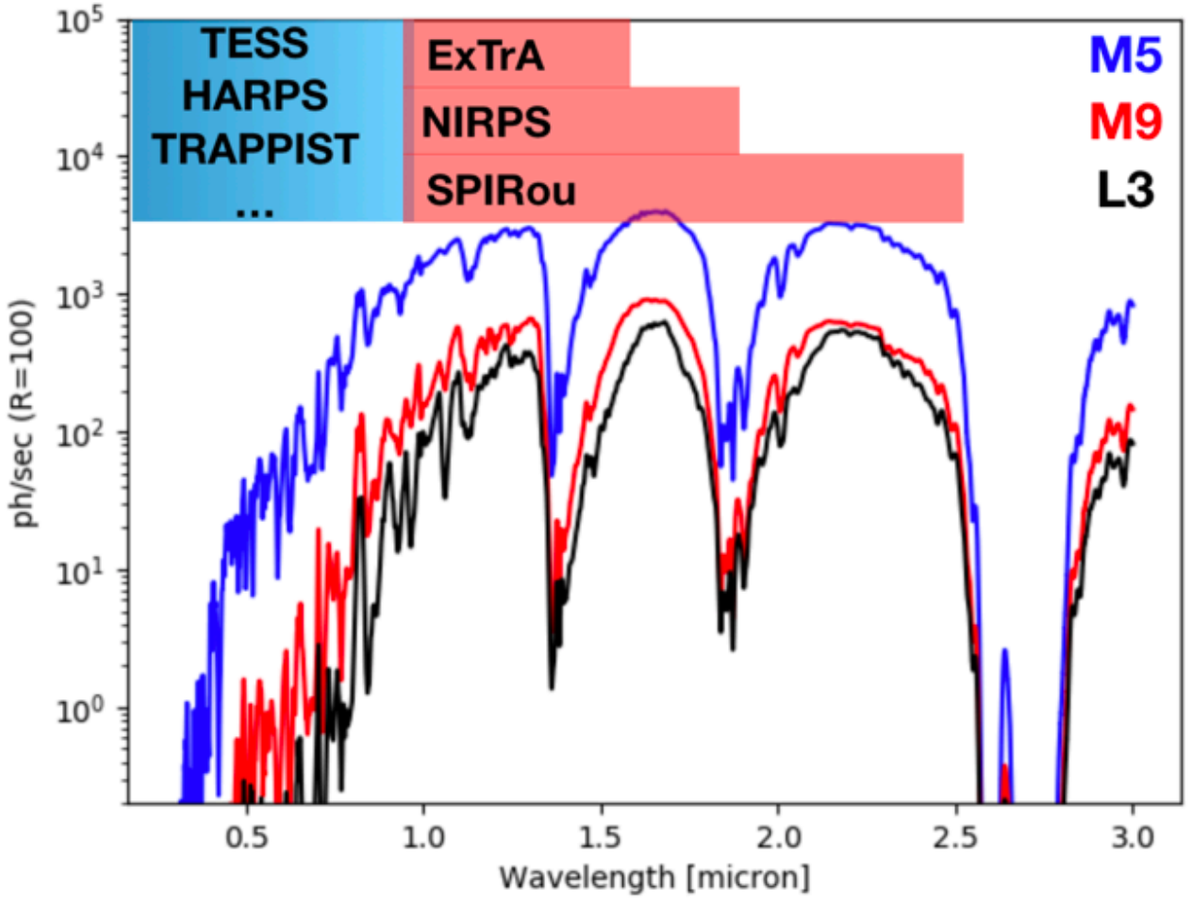

Infrared Photometry

Spitzer

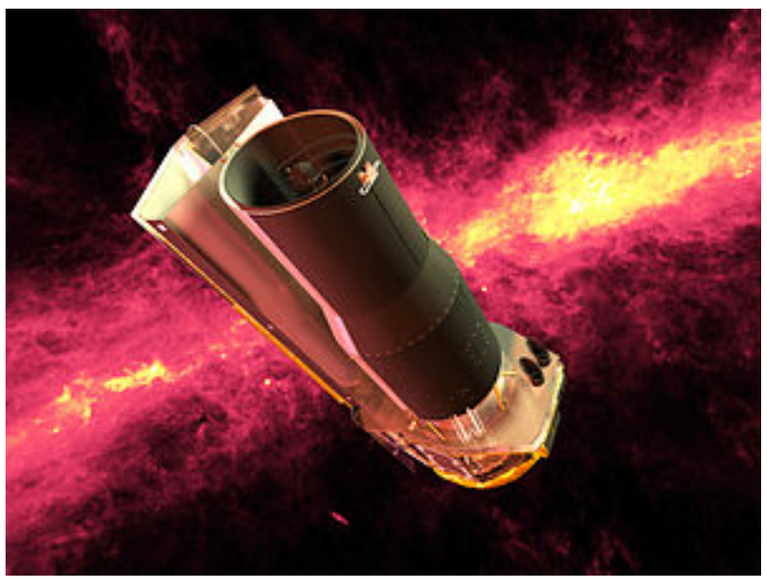

HAWK-I@VLT

ExTrA@La Silla

Xavier Bonfils

Doppler content

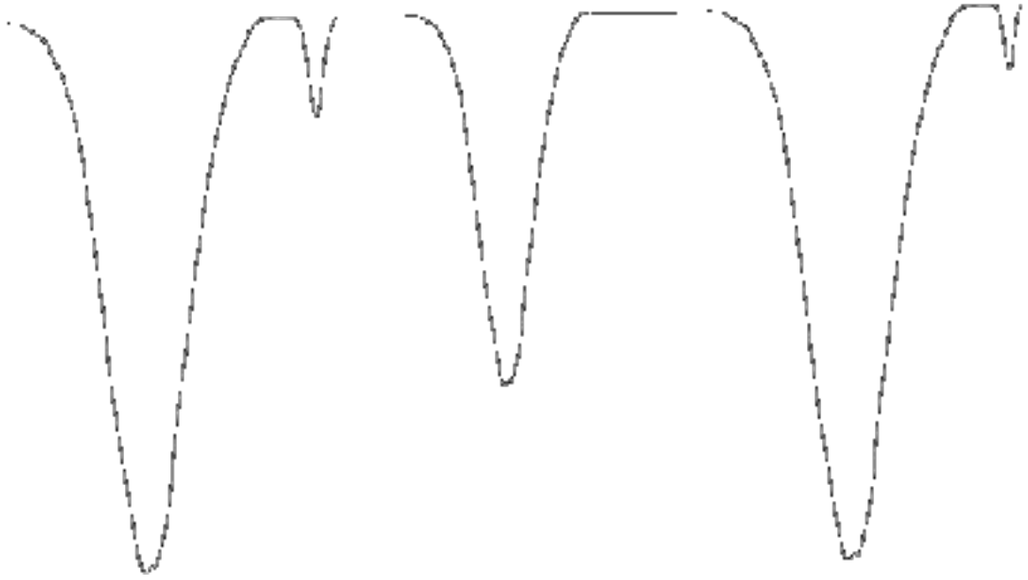

$$\delta V_{\mathrm{RMS}} = \frac{c}{Q\sqrt{N_{e^-}}}$$

- c: Speed of light
- δV_{RMS}: RV uncertainty
- Q: Quality factor
- N_{e^-}: # photo-electrons

All spectral elements do not contribute equally. Small velocity shifts produce larger change in spectral elements with larger slopes. The Doppler information content is therefore proportional to the slope.

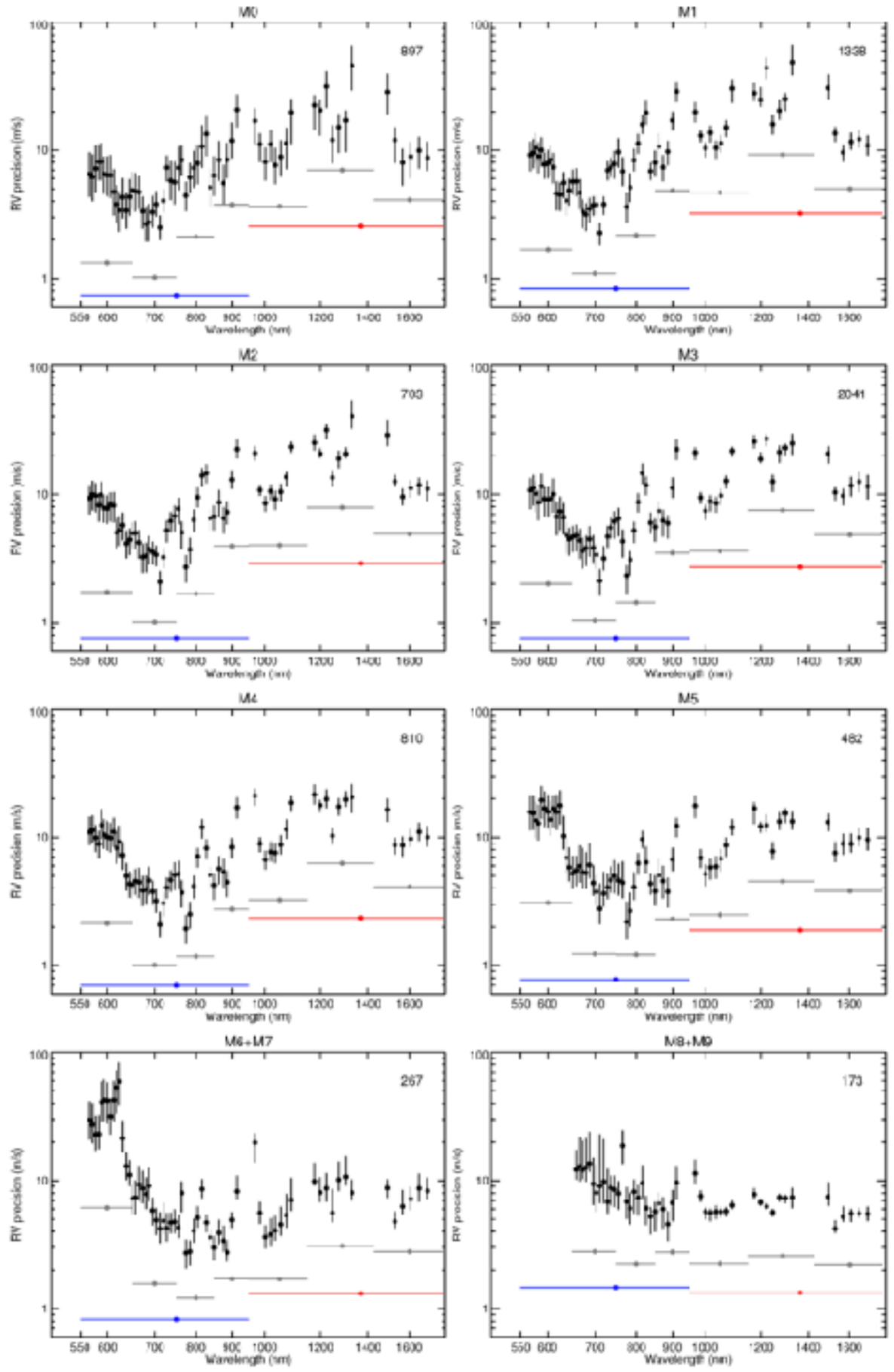

Reiners et al. (2010);

Xavier Bonfils

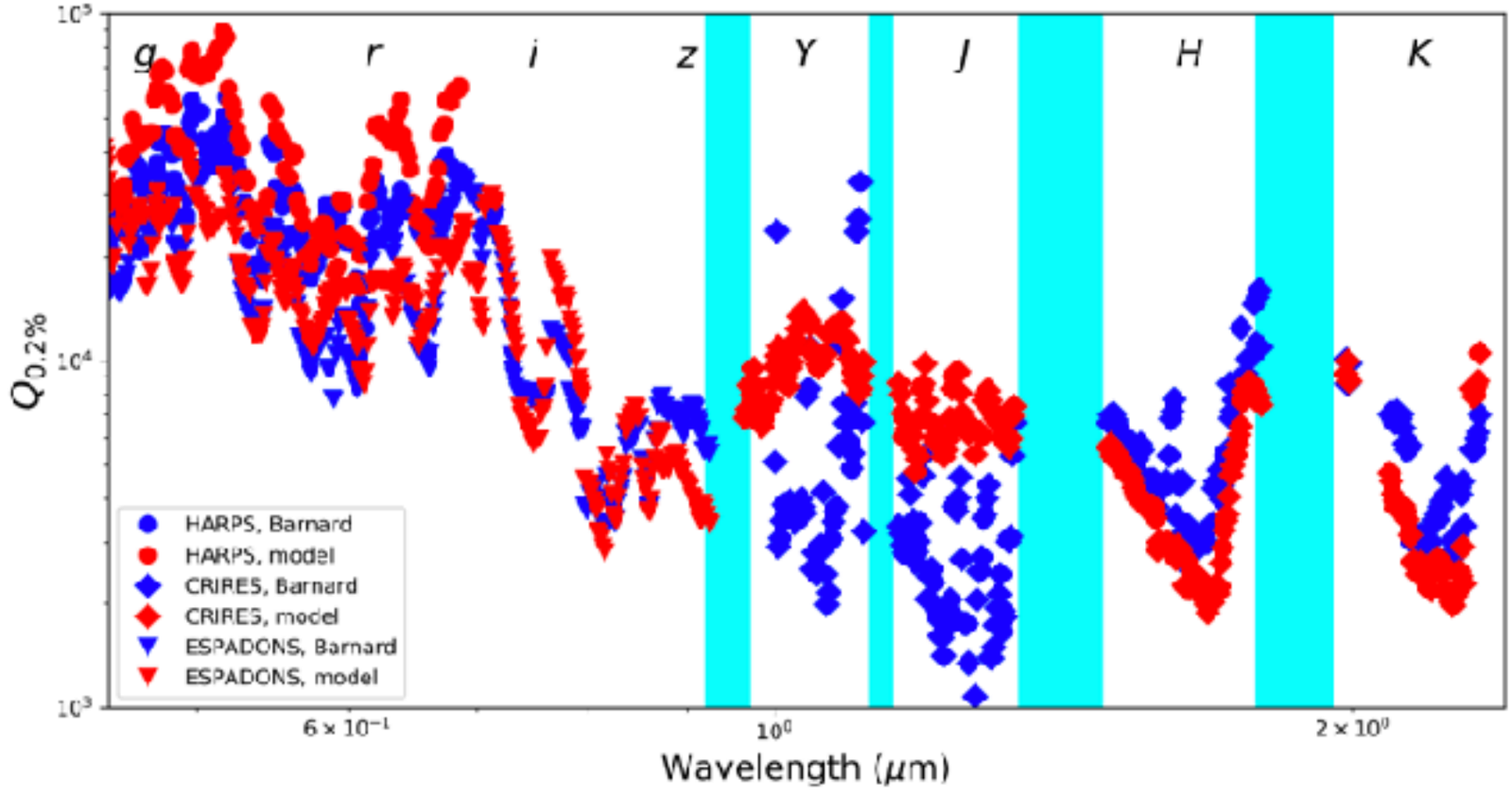

Artigau et al. (2018)

See also Reiners et al. (2010); Figueira et al. (2018)

Figure 2. (Top) Measured RV content of Barnard's star over the optical and near-infrared domain. Overall measured (blue) and model (red) RV density are well matched blueward of ~1 μm. The agreement is poorer in the near-infrared domain with an over-prediction of RV content in *Y* and *J* bands and an under-prediction in *H* and *K*. (Bottom) Ratio of observed to model $Q_{0.2\%}$ values. Areas unusable for RV measurements because of strong telluric absorption are filled in light blue.

Xavier Bonfils

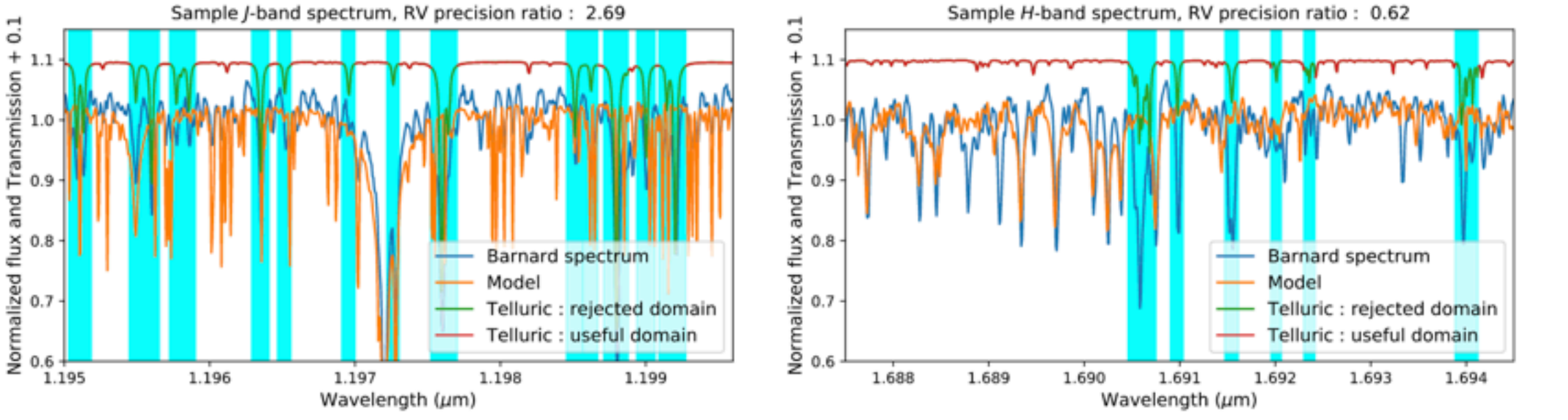

Figure 5. Spectrum of Barnard's star from the CRIRES data set (blue) and models (green) in representative regions of the J (top) and H (bottom) bands. The offset telluric absorption spectrum is shown, with regions included (teal) and excluded (red with cyan background shading) from the determination of Q. Within the J band, a large set of lines have over-estimated depth compared to estimations of the RV content. Within H, a numerous lines appear to be missing from models, leading to an under-estimation of the RV content. For the J-band sample spectrum domain shown here, the RV precision ratio is 2.69; for that wavelength domain, the RV precision limit reachable at a given S/N will be degraded by that amount.

Artigau et al. (2018)

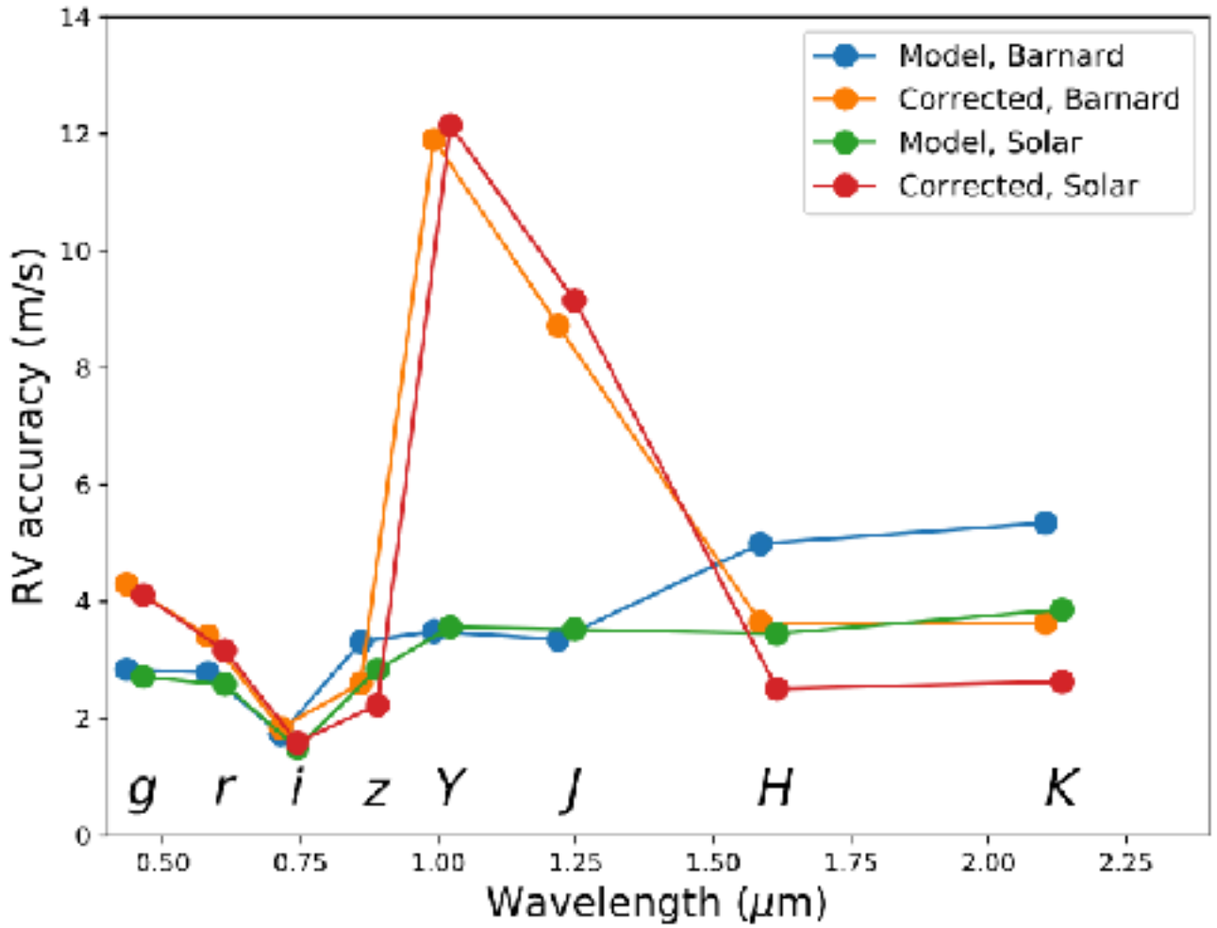

Figure 7. Per-bandpass radial velocity achievable for an S/N = 100 in J for a $\lambda/\Delta\lambda = 10^5$ resolution element. Models for Barnard's ($\log g = 5.0$, metal $= -0.5$ dex) and solar ($\log g = 5.0$, metal $= 0.0$). The correction factor measured for Barnard's star is applied to all models to derive corrected RV precision. Changes are small in the optical between models, and corrected values change the predicted sensitivities only a little. In the near-infrared, models predict comparable contributions from the Y, J, H, and K bands for the solar model (i.e., $\sim$3–5 m s^{-1}), while corrected values indicate much more accurate measurements in H and K compared to the Y and J.

Actual IR gain is a factor of a few

Xavier Bonfils

Stellar activity

Stellar activity & rotation

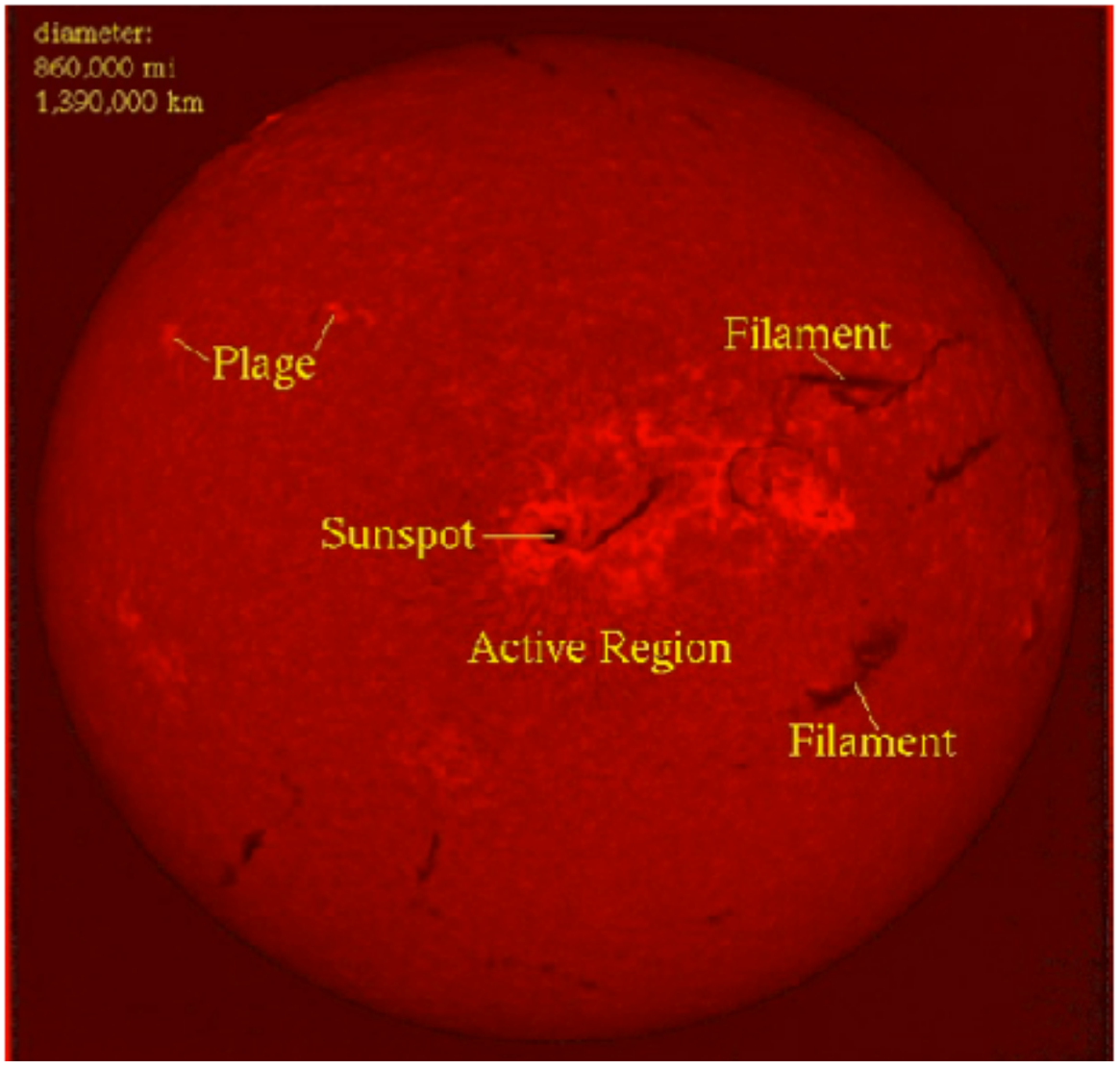

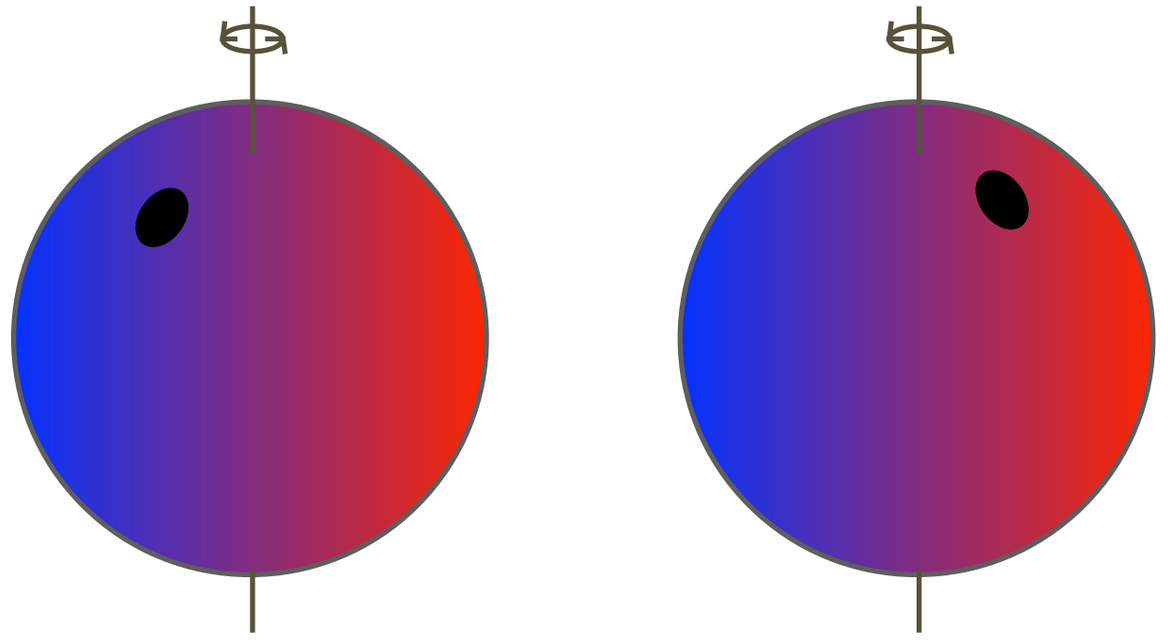

Xavier Bonfils

Stellar activity

GJ 674

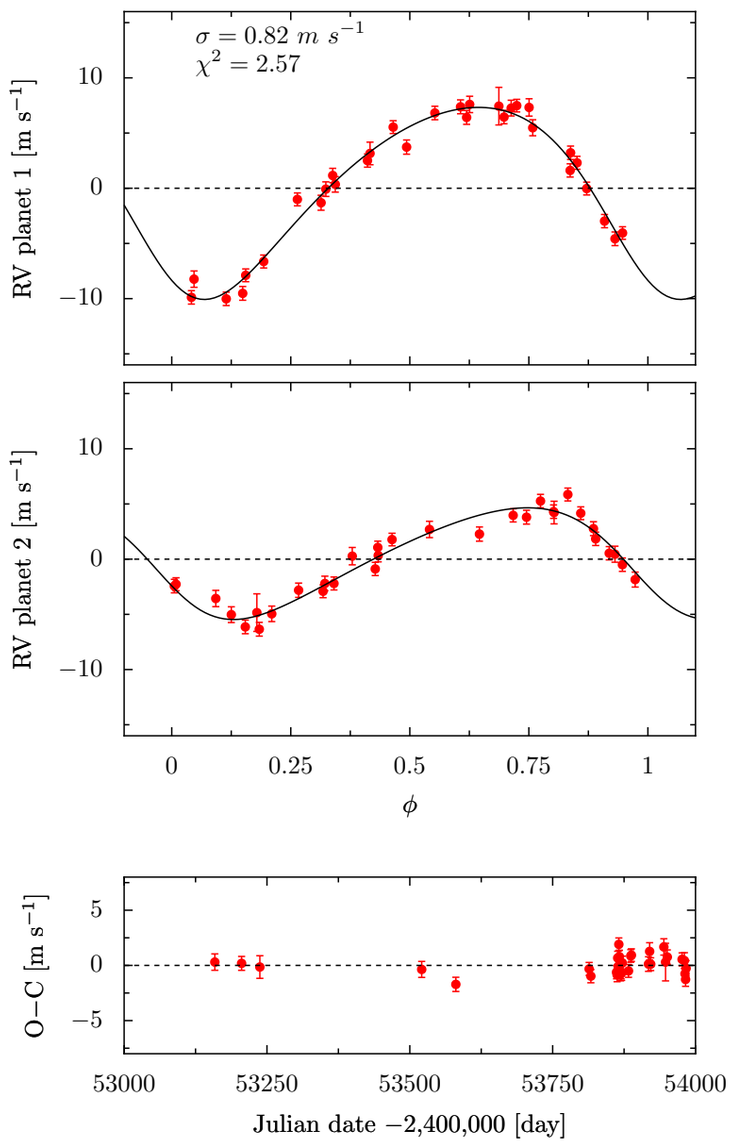

2-planet Keplerian model

Parameters		GJ 674 b	GJ 674 c
P	(day)	4.7	35
e		0.2	0.2
w	(deg.)	143	113
K	(m/s)	8.7	5.06
m2 sin i	($M_\oplus$)	11.1	12.6
a	(AU)	0.039	0.147

Xavier Bonfils

Stellar activity

GJ 674

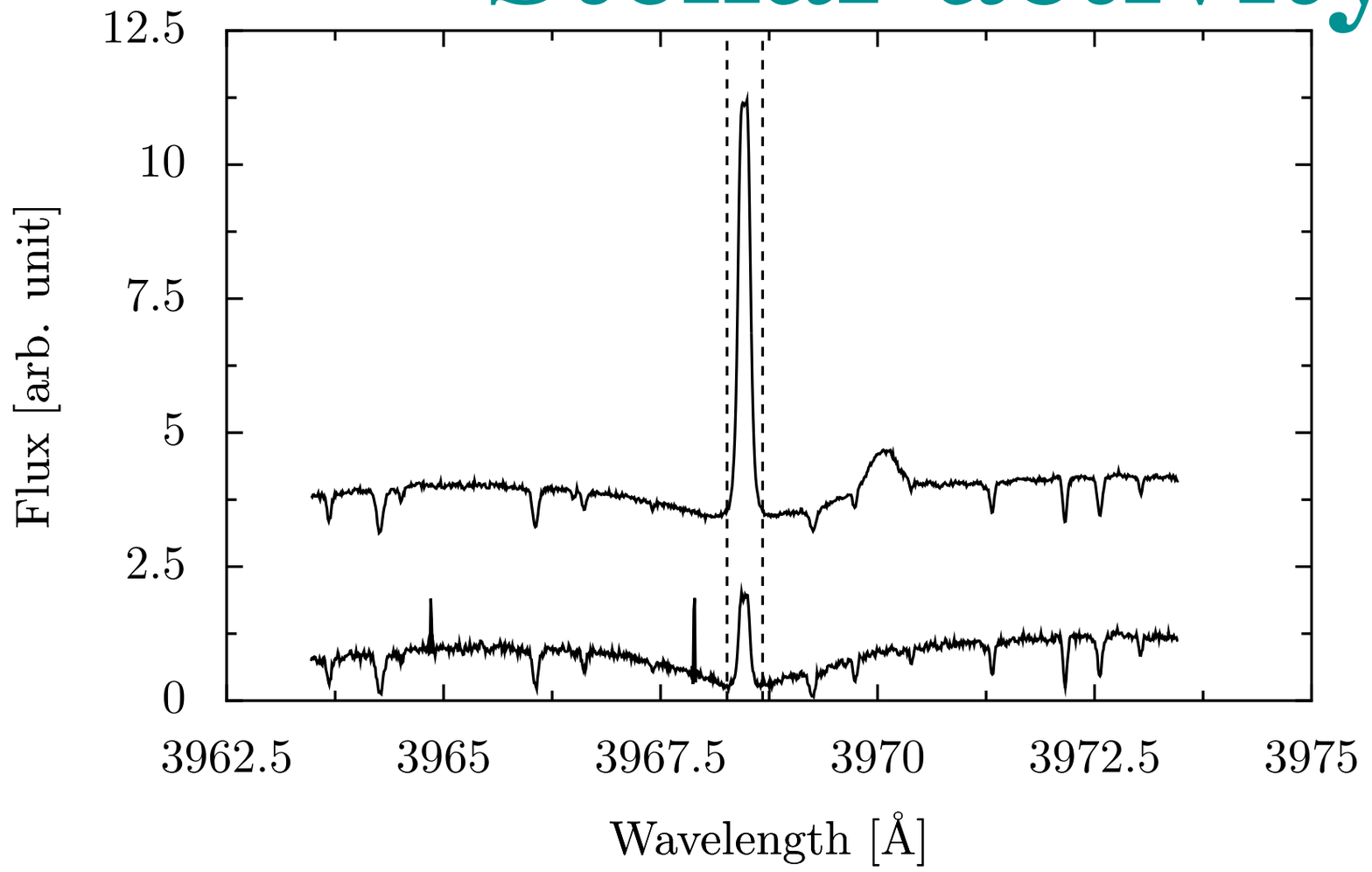

Activity preview

GJ 674's Ca II H&K lines have large emission reversals compare to other targets

→ prompt for an activity analysis

Xavier Bonfils

Stellar activity

GJ 674

Spectroscopy

Pvar ~ 35 days

→ 2nd signal is likely caused by a spot

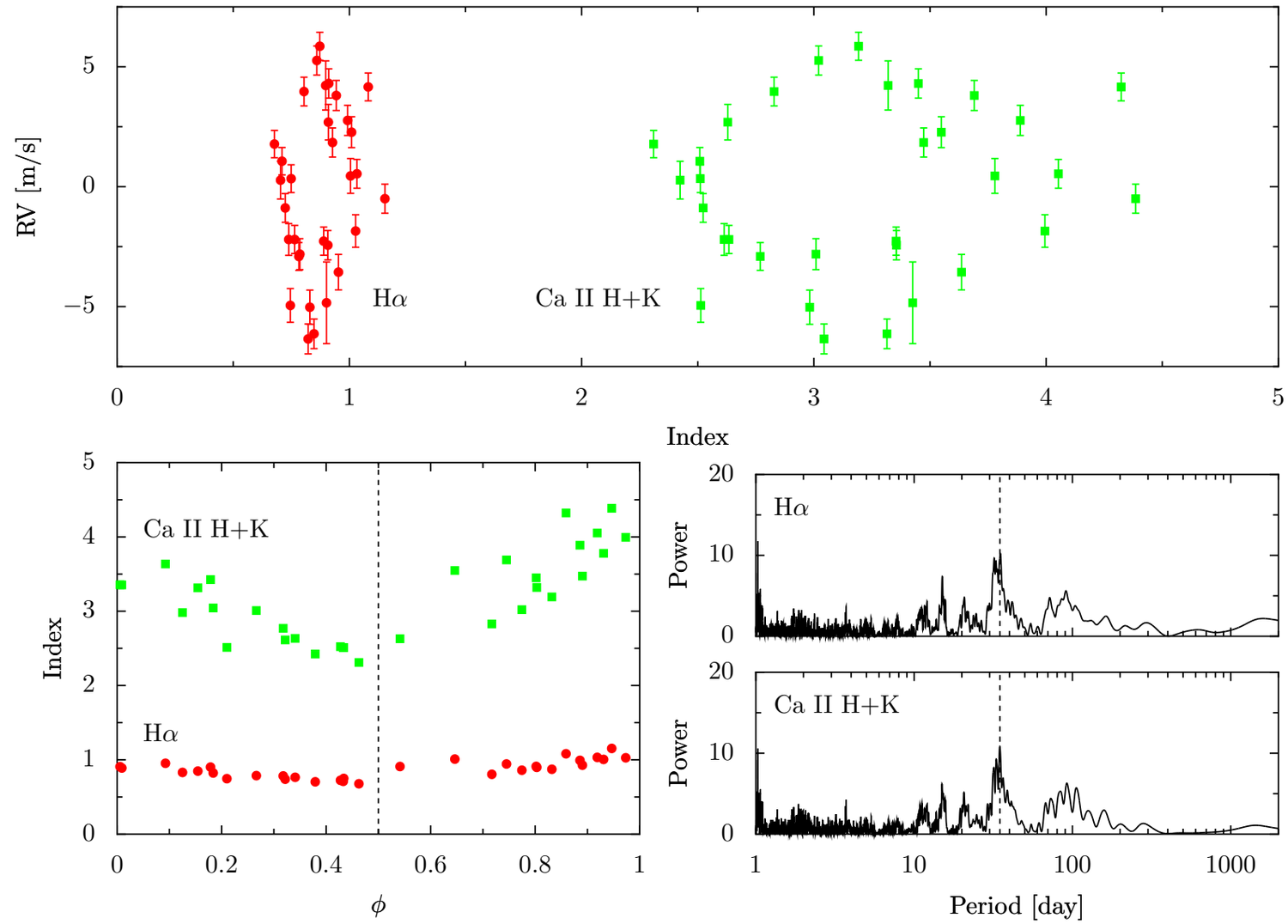

Xavier Bonfils

Stellar activity

GJ 674

Photometry

P_{var} ~ 35 days

2nd signal is likely caused by a spot

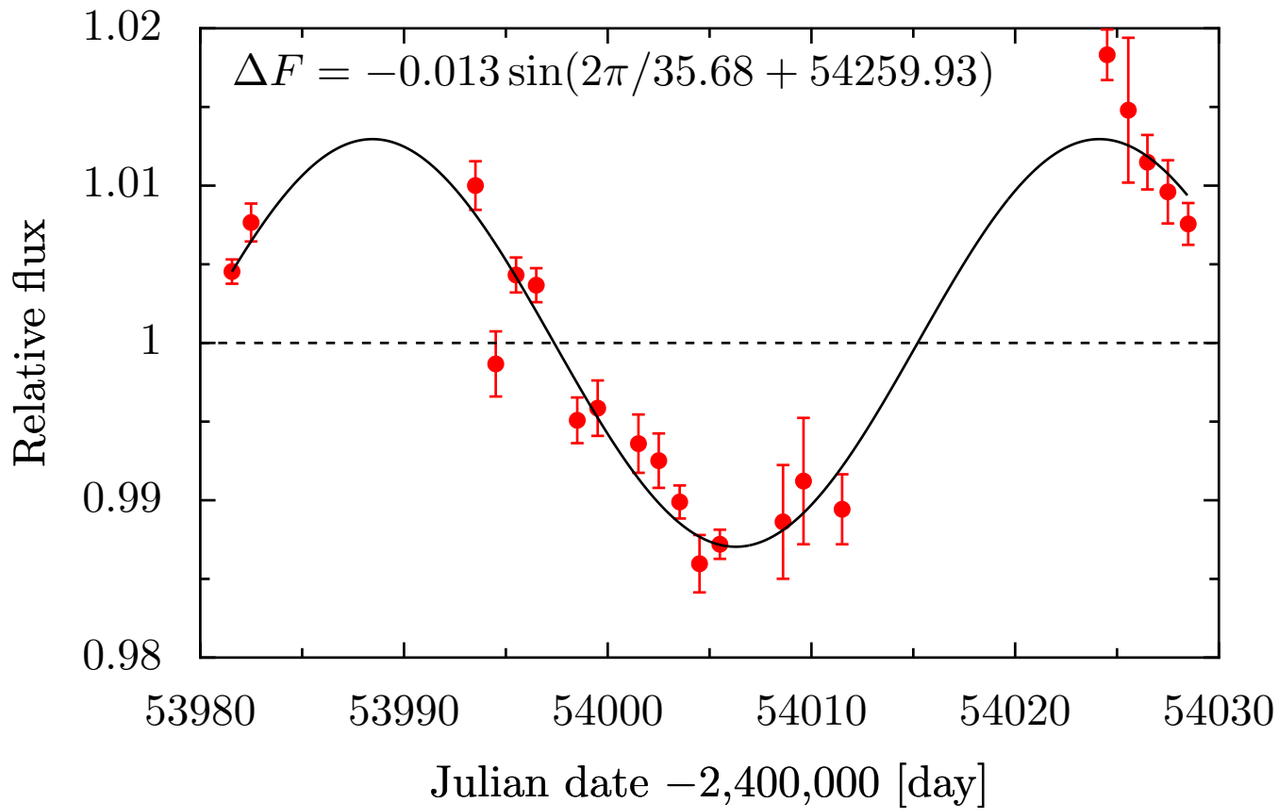

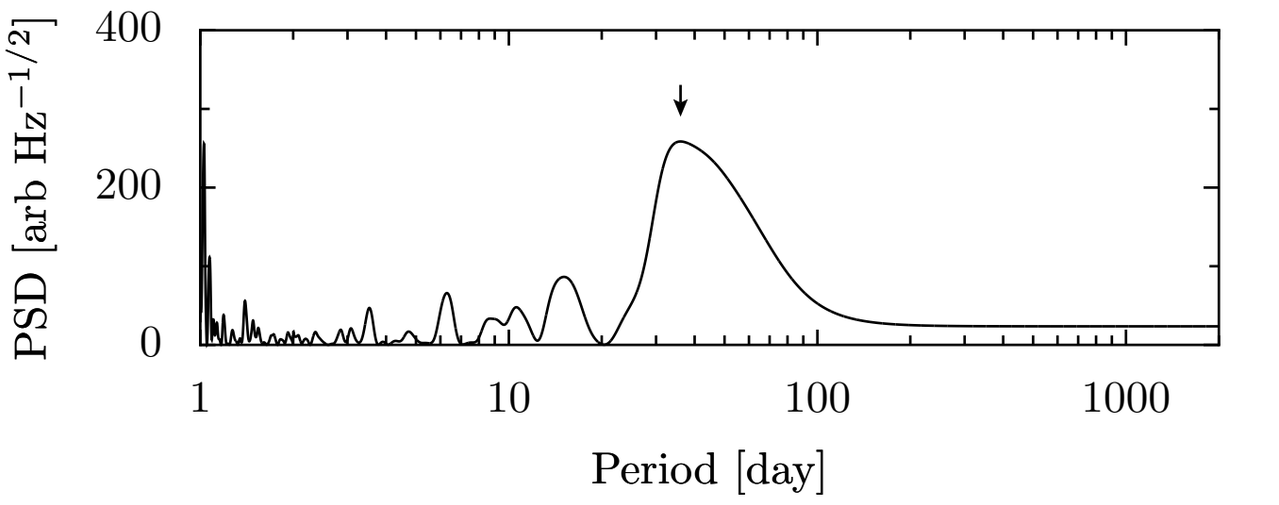

Xavier Bonfils

Stellar activity

GJ 674

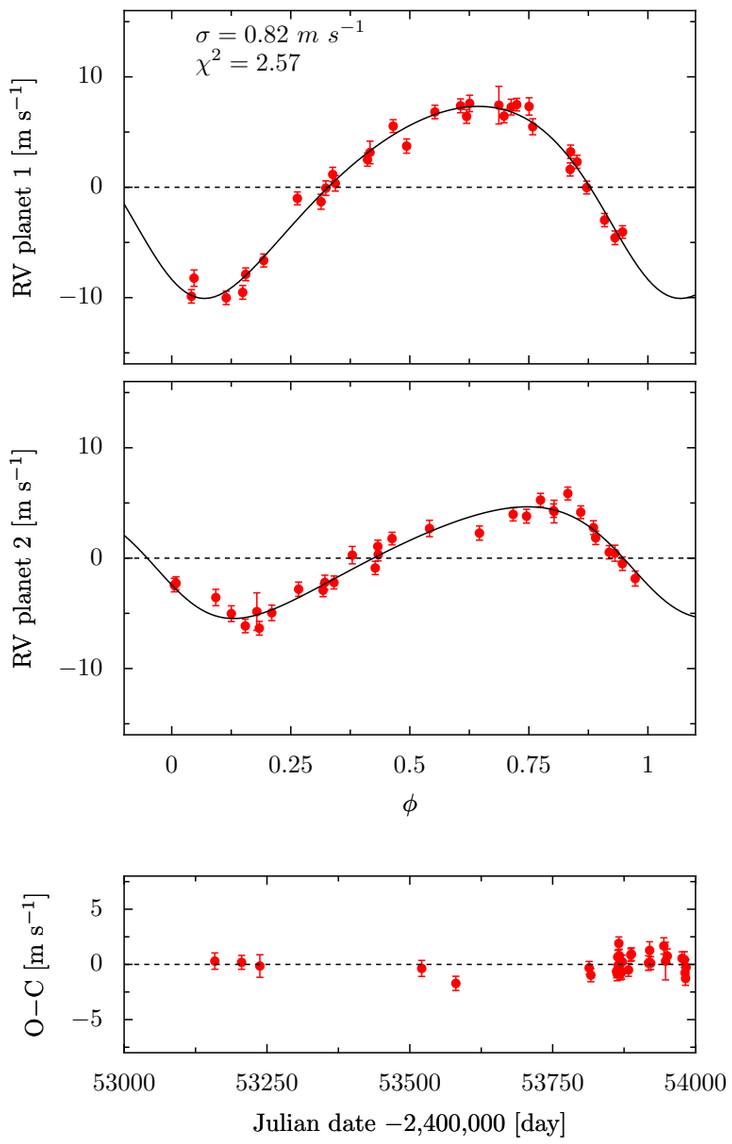

2-planet Keplerian model

Parameters		GJ 674 b	Spot
P	(day)	4.7	35
e		0.2	0.2
w	(deg.)	143	113
K	(m/s)	8.7	5.06
m2 sin i	($M_\oplus$)	11.1	12.6
a	(AU)	0.039	0.147

Bonfils et al. (2007)

Xavier Bonfils

RV noise of flares

100 m/s

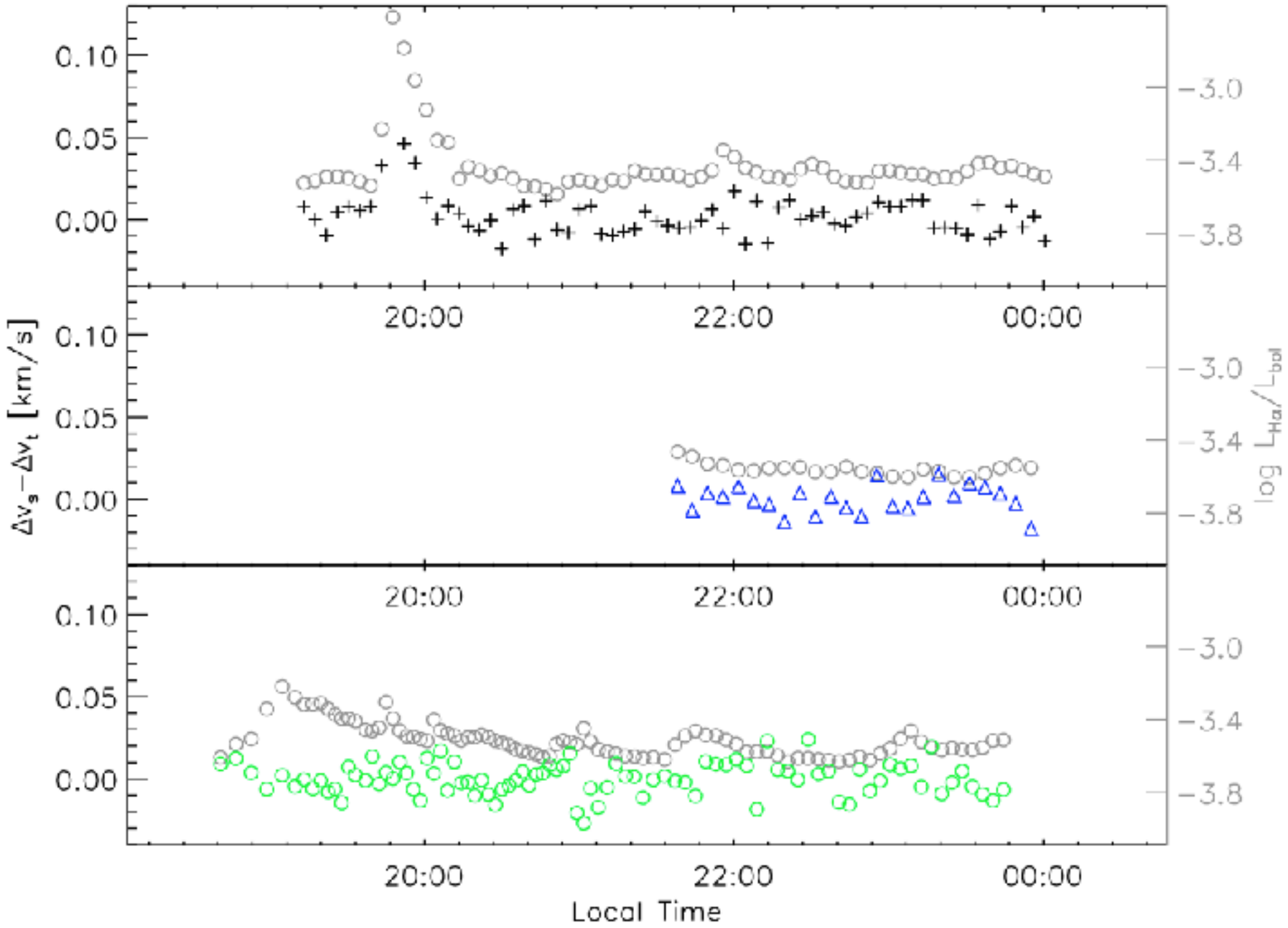

Reiners (2009)

H alpha

Proxima

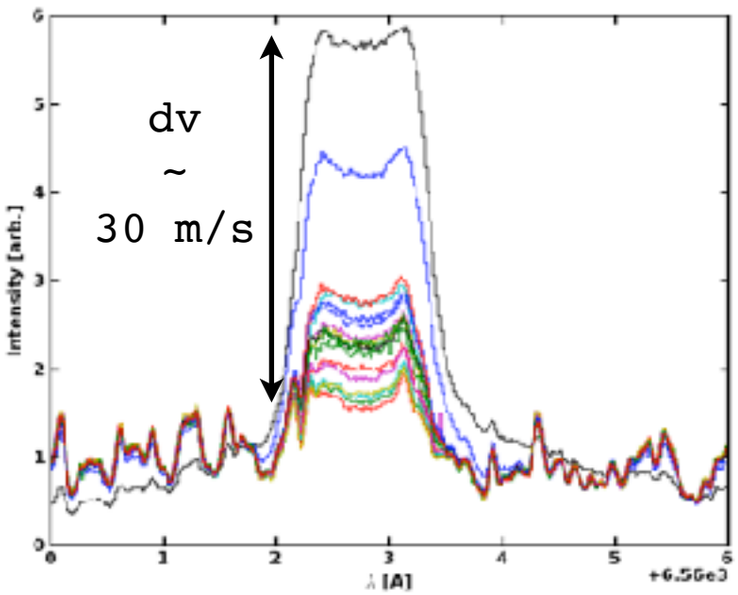

Barnard

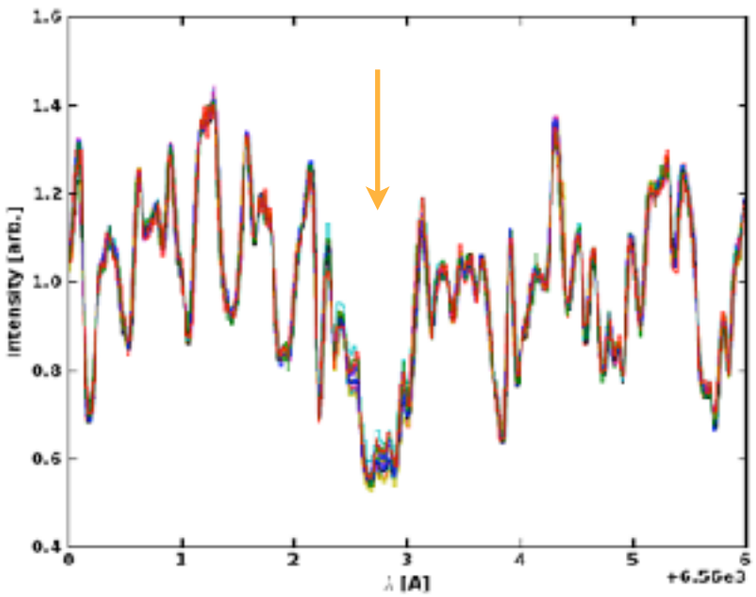

GJ 876

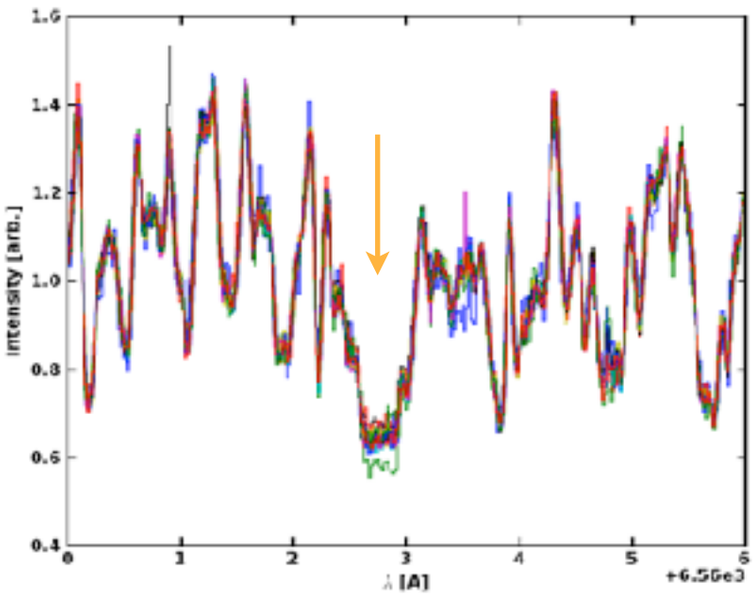

GJ 1214

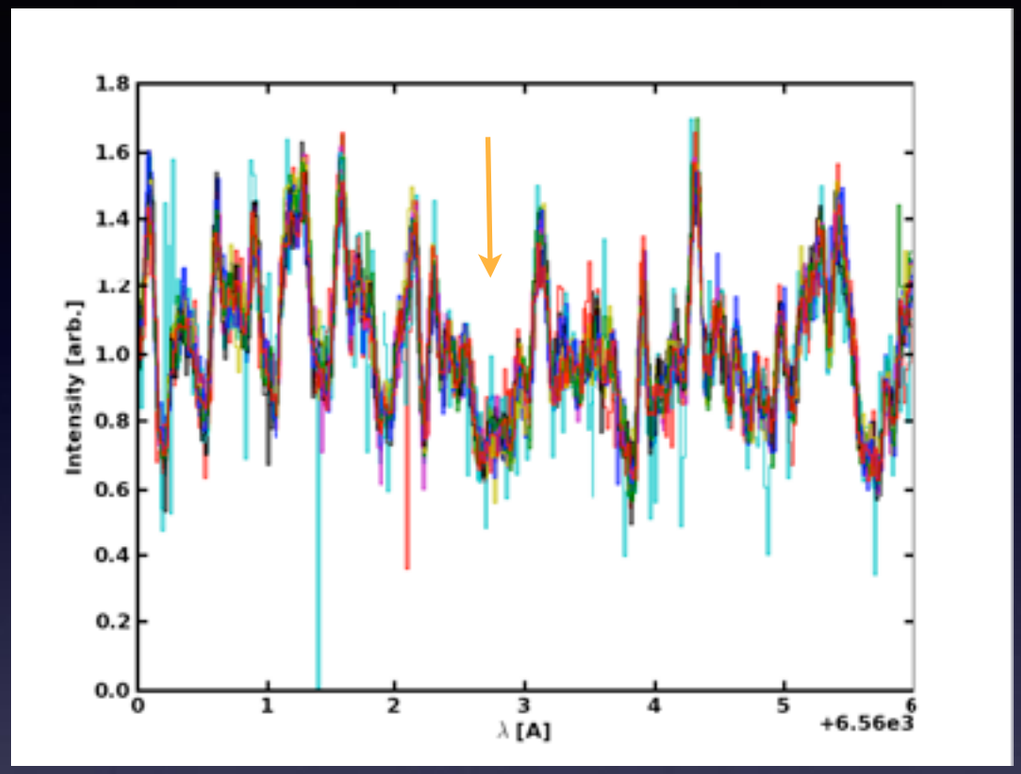

GJ 1214 Median

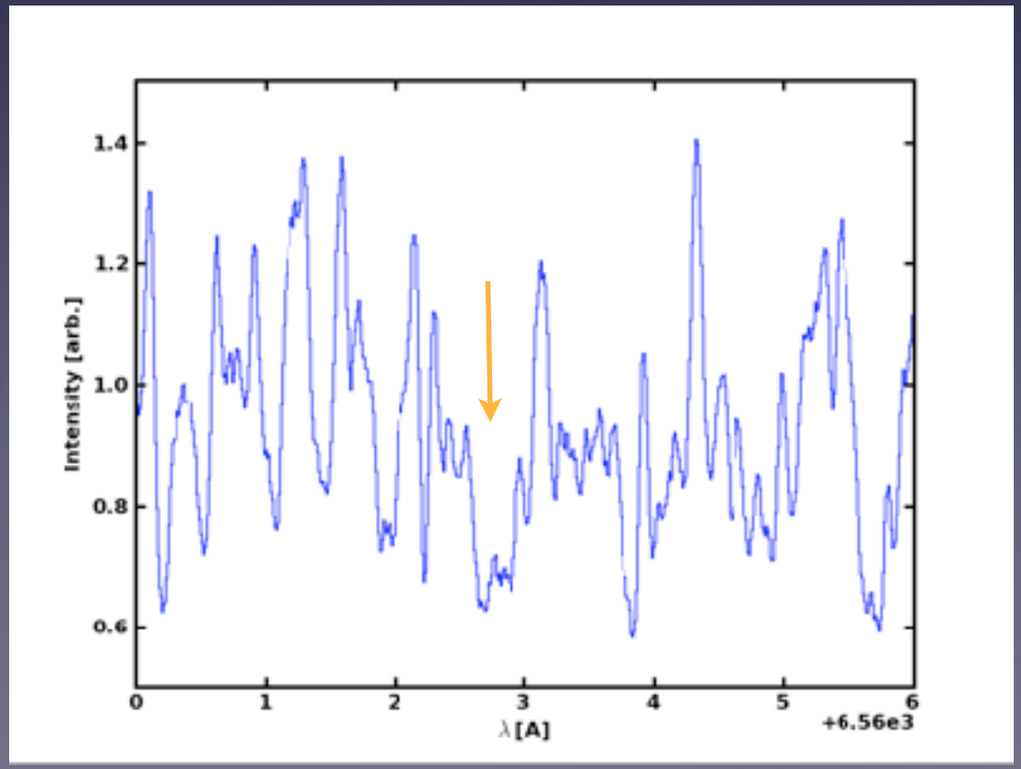

Na I D 1&2

Proxima

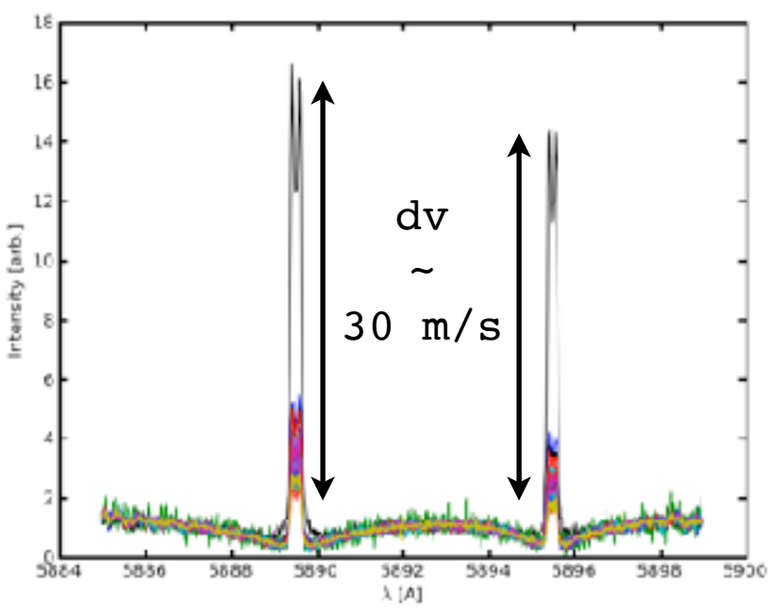

Barnard

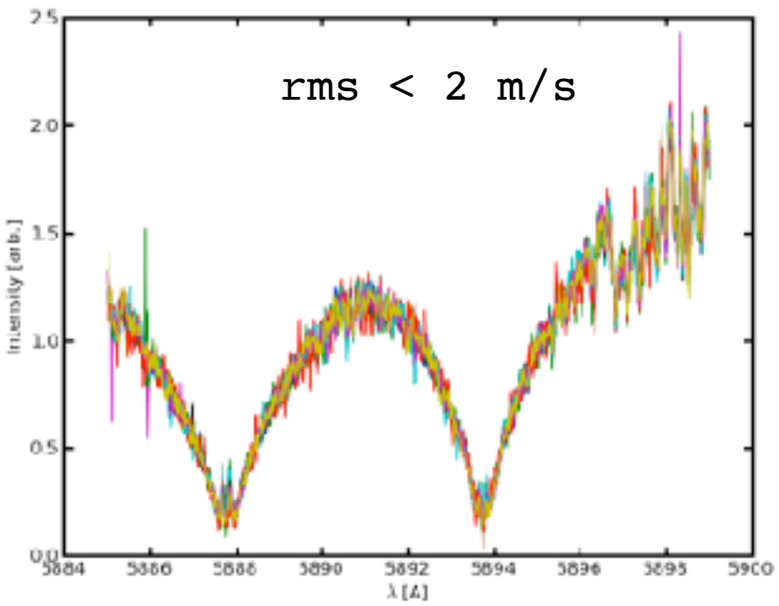

GJ 876

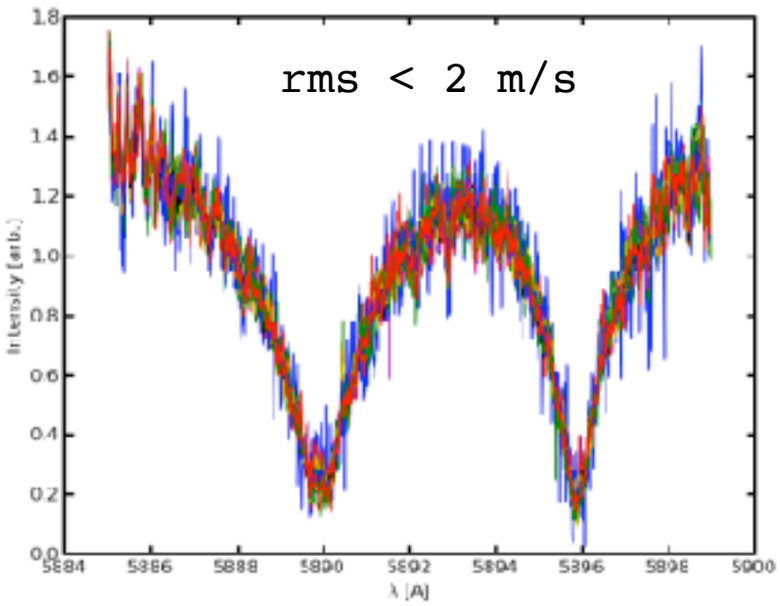

GJ 1214

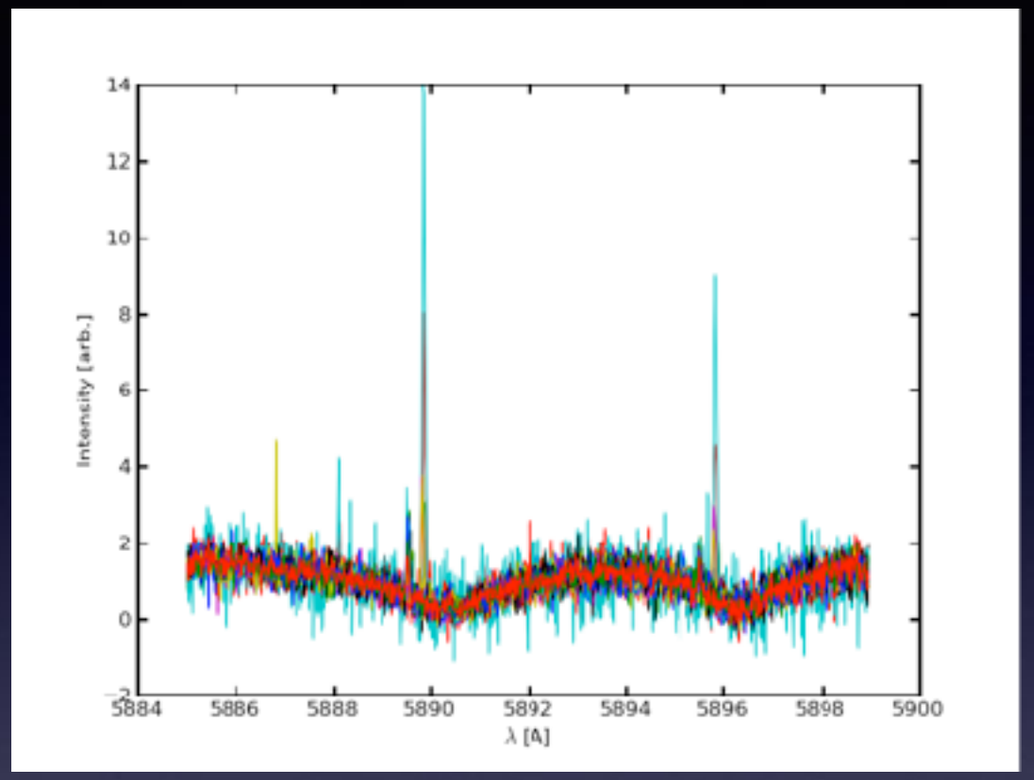

GJ 1214
Median

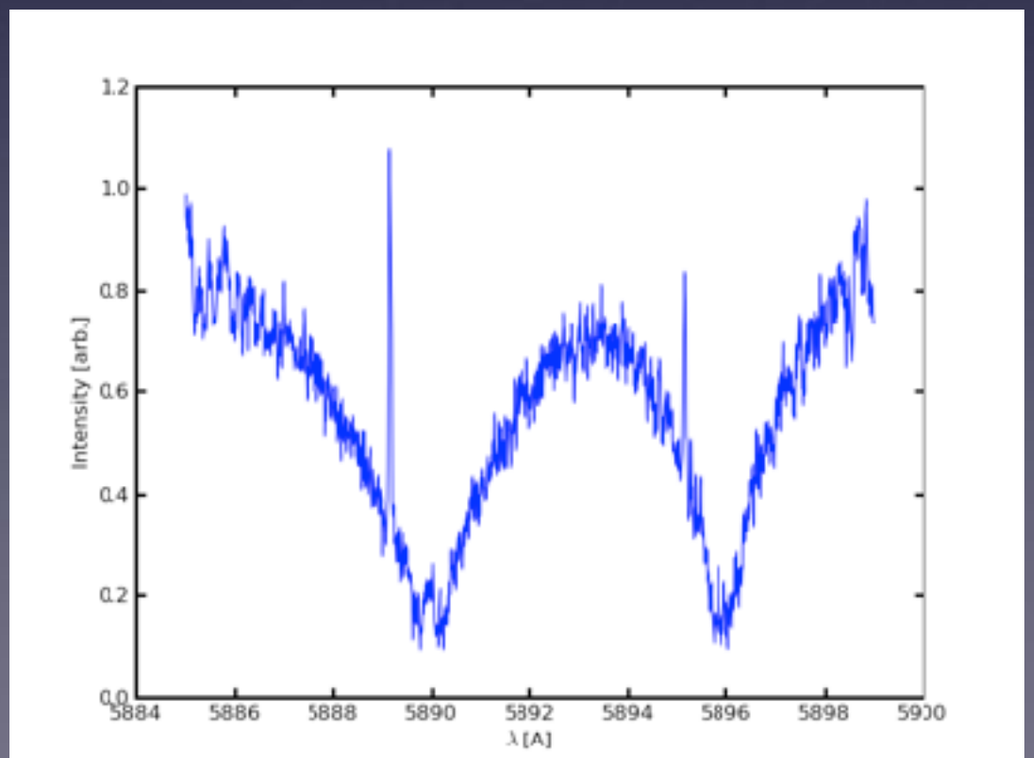

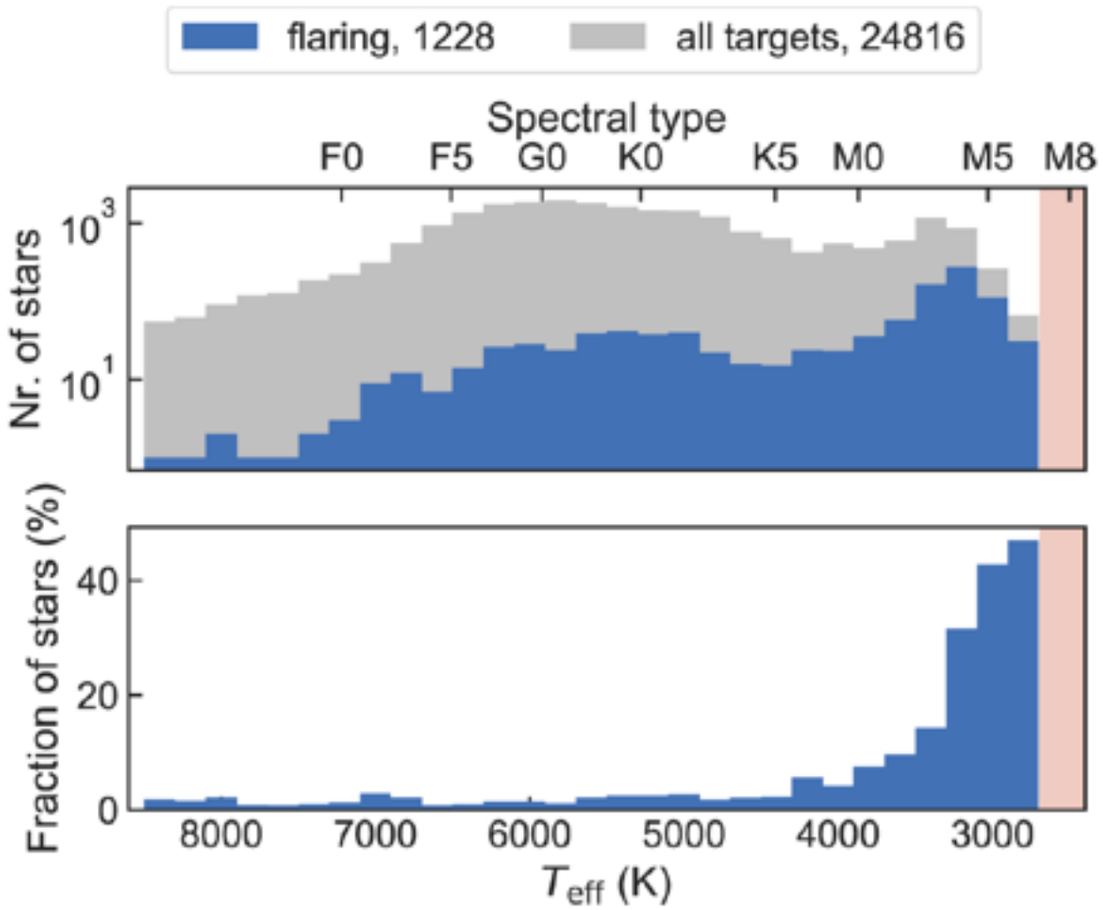

- Study w/ TESS by Gunter et al . (2020)
- mid-M and later types are most common flaring stars

- correlate well with Halpha
- easily diagnose in spectra

=> can be discarded easily from RV time series

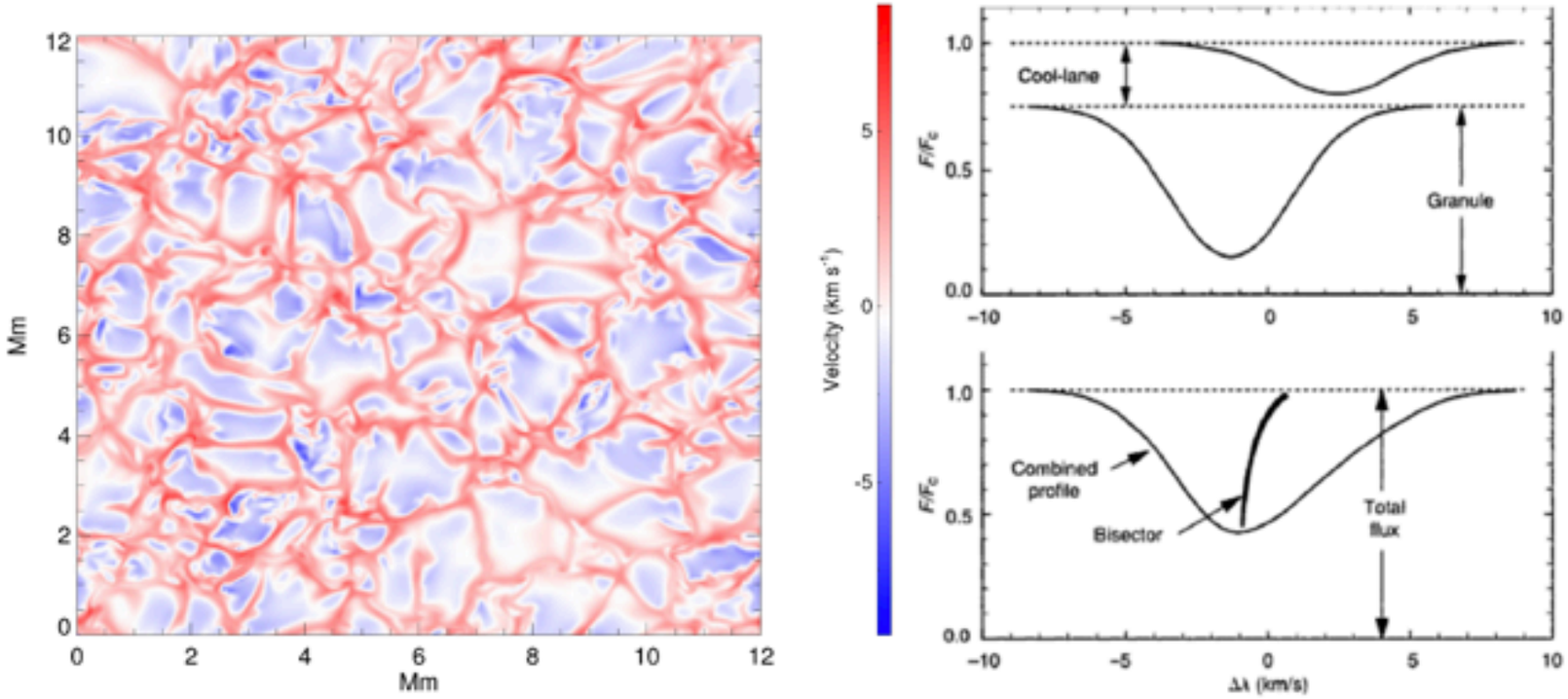

RV change due to change in the convection

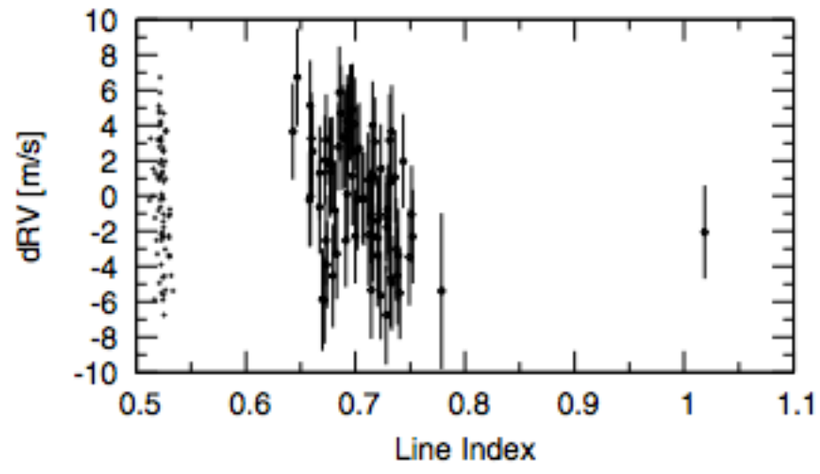

Fig. 8. Correlation of the Hα-index with the RV for Barnard's star (dots with error bars, $r_{H\alpha} = 0.42$). For comparison the CaI-index (crosses).

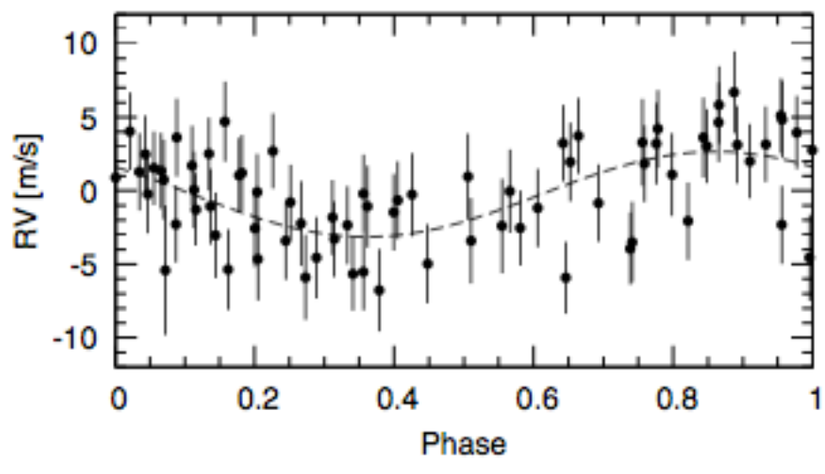

Fig. 5. Radial velocity time series for Barnard's star phased to the 44.9 d period and the best-fitting sinusoid.

Kuerster et al. (2003)

- anti-correlation Halpha-RV (not a loop)
- modulation is also on a shorter time-scale than rotation (believed to be ~130d)

- => change in the convective blue shift (which actually is a red-shift for Barnard's star) due to magnetic plages that locally inhibit convection

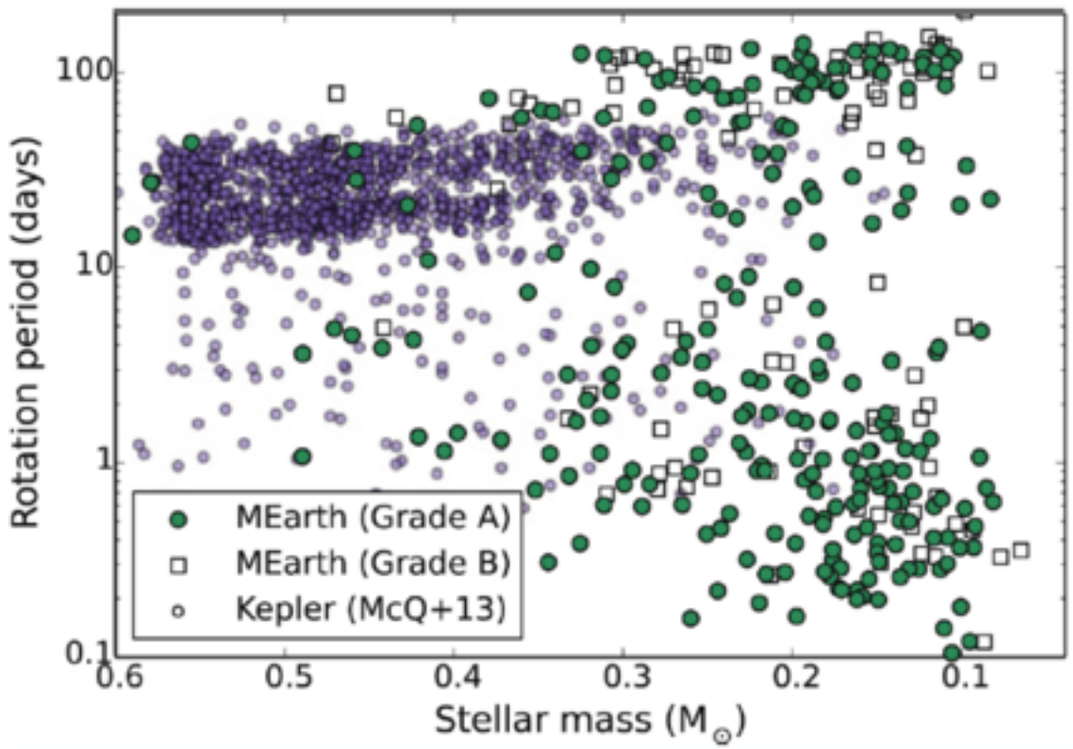

Newton et al. (2016)

- Evidence for 2 populations toward later types, fast and slow rotators
- And a lack of stars with intermediate rotation periods

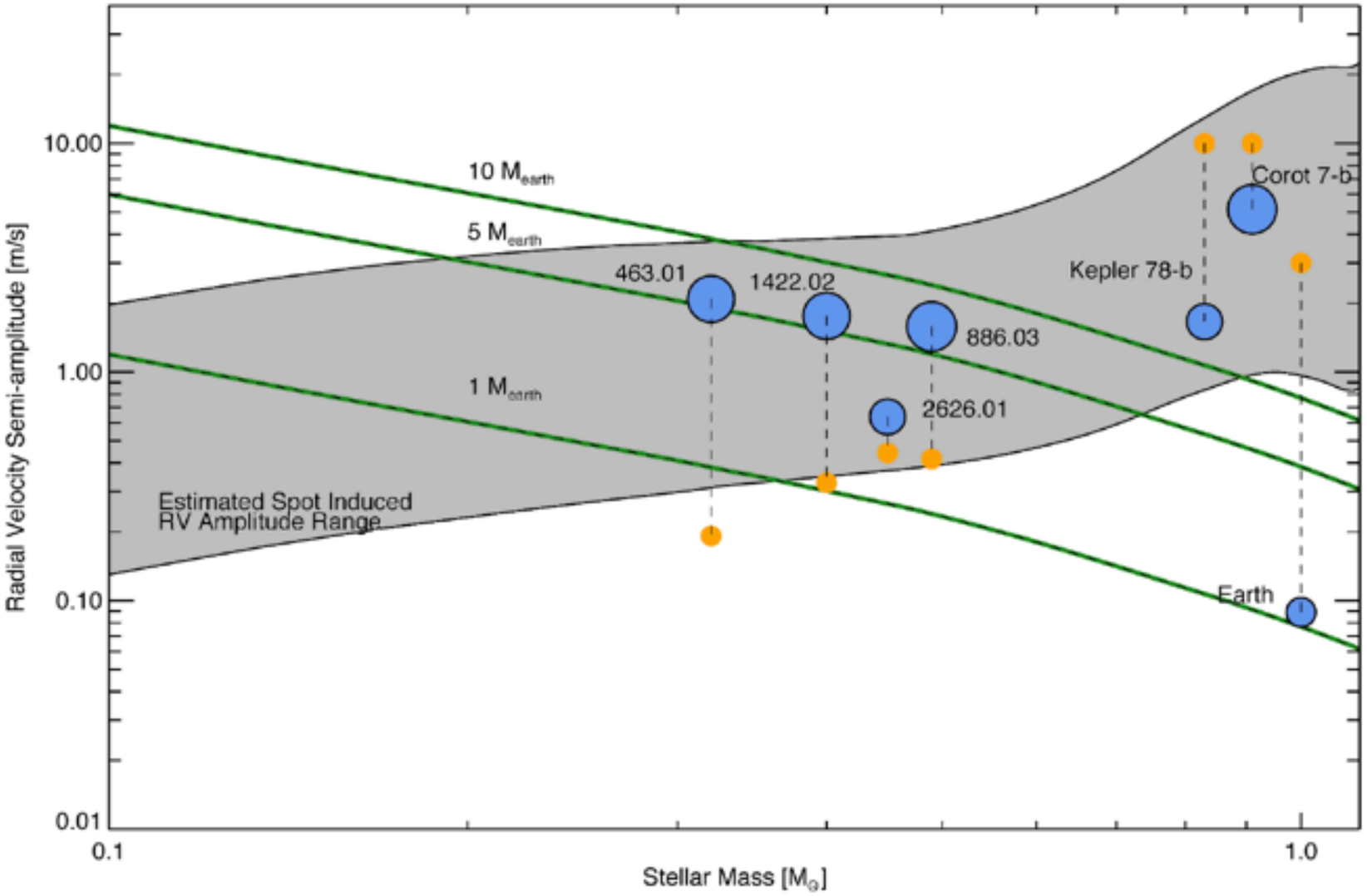

FIGURE 1.17— Estimated characteristic semi-amplitudes of radial velocity signals. The semi-amplitude of rotational modulations due to starspots as a function of stellar mass is shown in gray. The radial velocity semi-amplitude of exoplanets in the habitable zone of stars of various masses are drawn in green lines. Characteristic exoplanets are plotted in blue, with the size of the dot corresponding to the planetary radius. Each exoplanet plotted is connected by a thin dashed vertical line to an orange dot, corresponding to the predicted or observed radial velocity semi-amplitude induced by stellar rotation. Earth- and super-Earth-mass planets in the HZ of M dwarfs ($M_\star < 0.6\,M_\odot$) have radial velocity signals caused by planetary companions or active regions with the same amplitude. From Vanderburg et al. (2016).

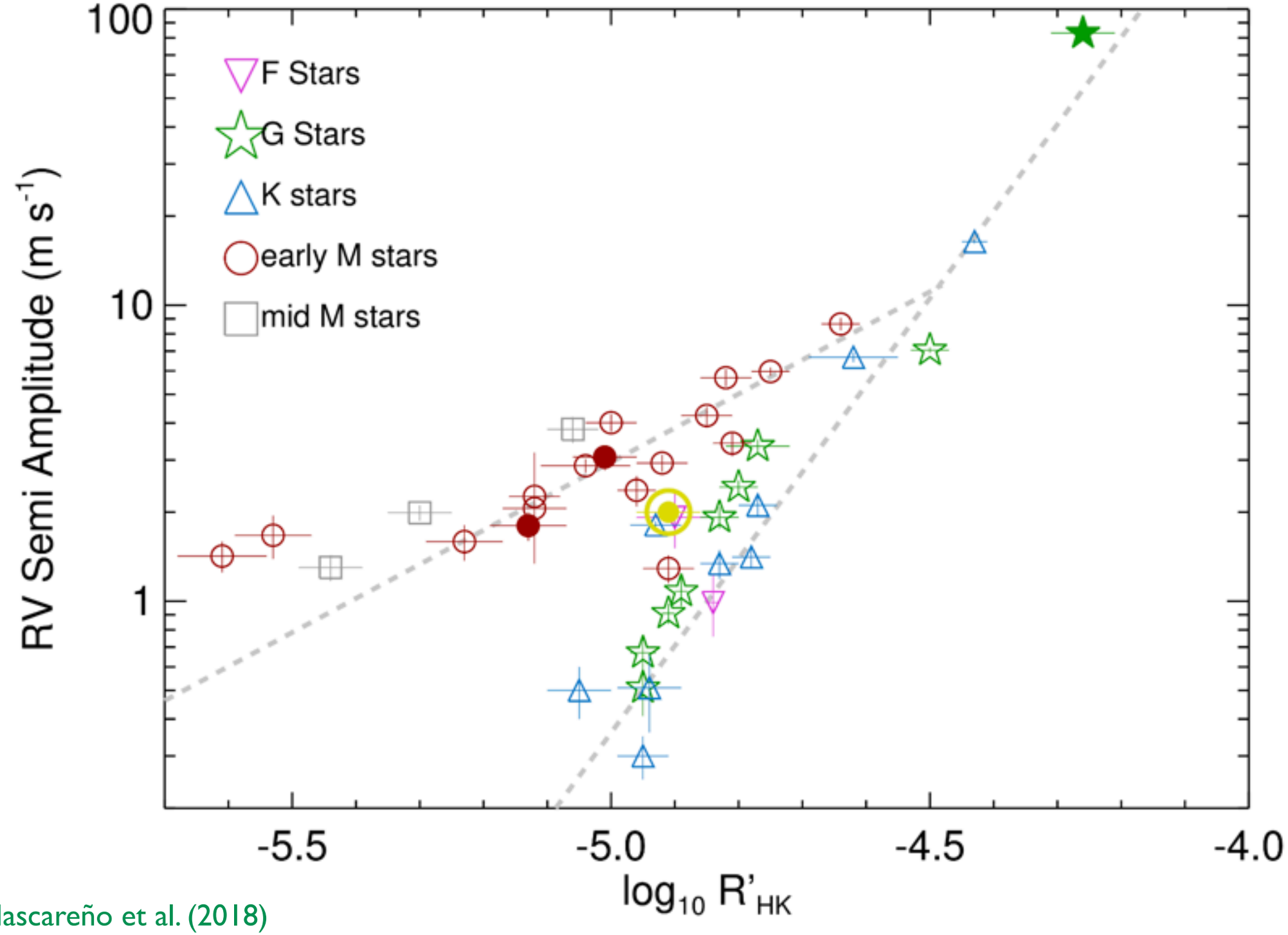

Suárez Mascareño et al. (2018)

Figure 9. Semi-amplitude of the rotation induced signal versus chromospheric activity level $\log_{10}(R'_{HK})$. Empty symbols correspond to our data, filled symbols the literature data. The grey dashed lines show the best fit to the date for the two groups of stars: FGK-type stars on one group, M-type stars on the other.

Strategies / tool box to address stellar activity

Xavier Bonfils

Linear fit w/ activity proxy

A&A 379, 279–287 (2001)
DOI: 10.1051/0004-6361:20011308

Astronomy & Astrophysics

No planet for HD 166435

D. Queloz[1], G. W. Henry[2], J. P. Sivan[3], S. L. Baliunas[2,4,5], J. L. Beuzit[6], R. A. Donahue[4,5], M. Mayor[1], D. Naef[1], C. Perrier[6], and S. Udry[1]

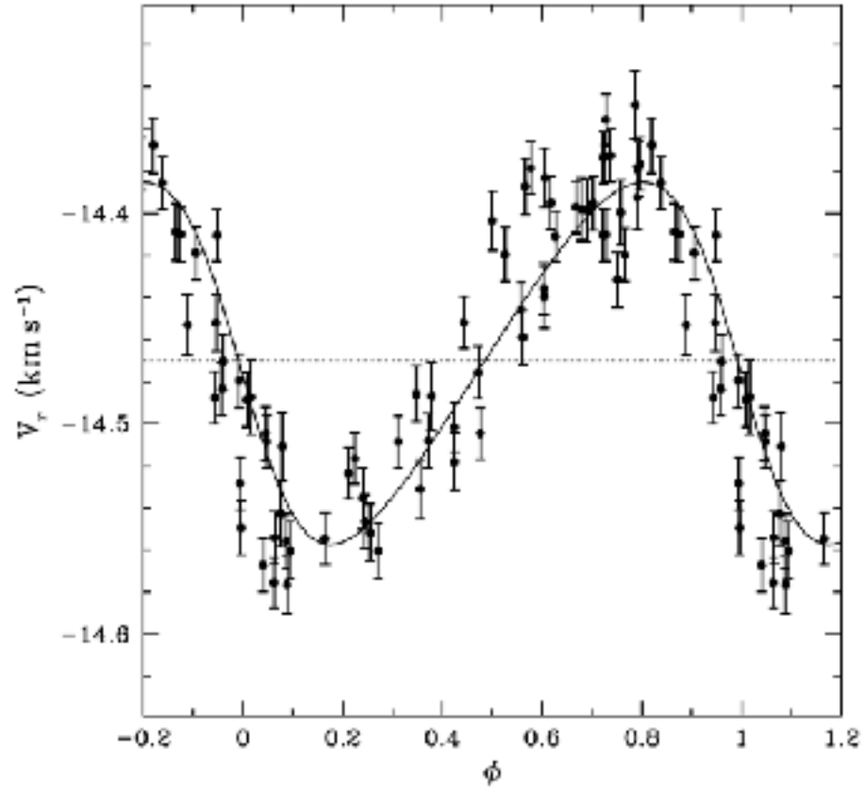

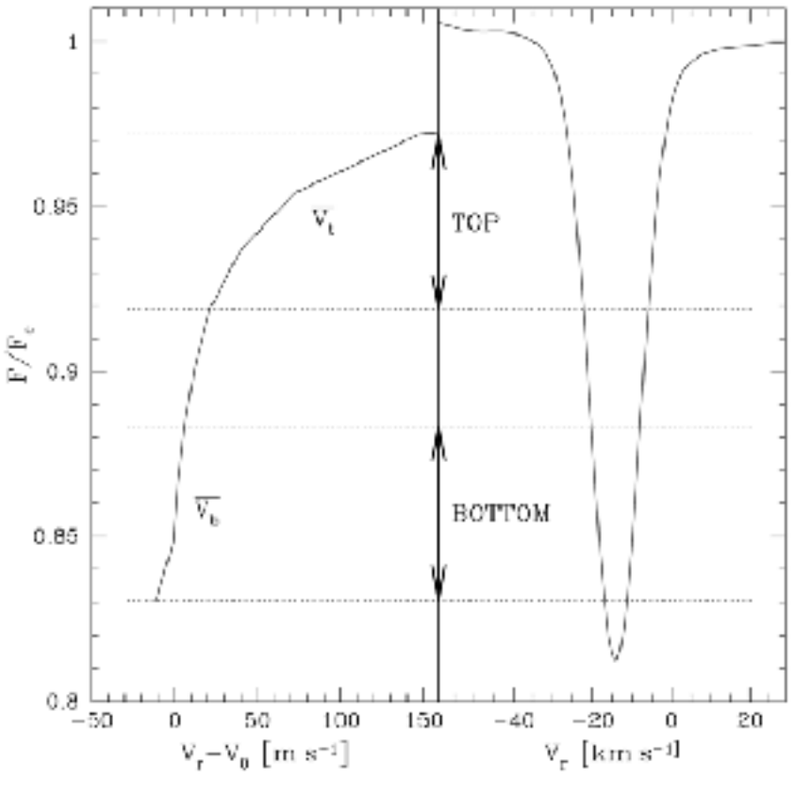

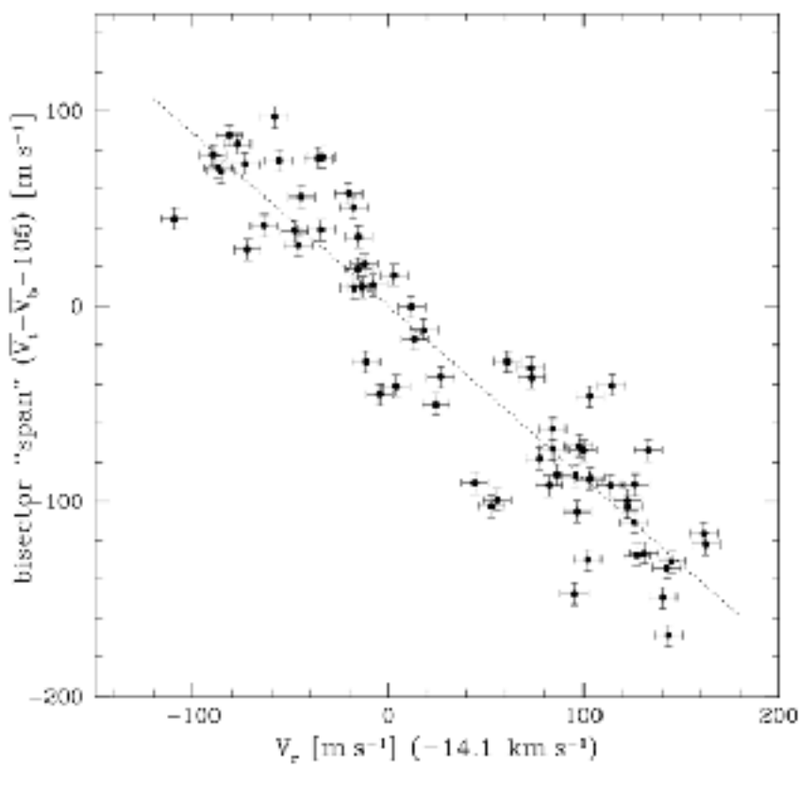

Queloz et al. (2001); also HD 41248 Santos et al. (2014)

Xavier Bonfils

Linear fit w/ activity proxy

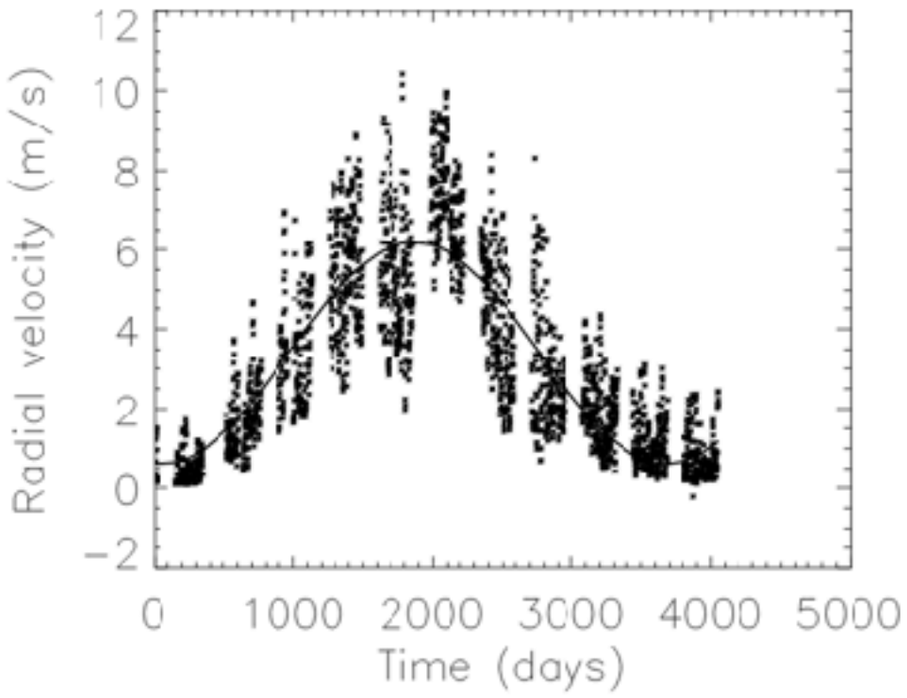

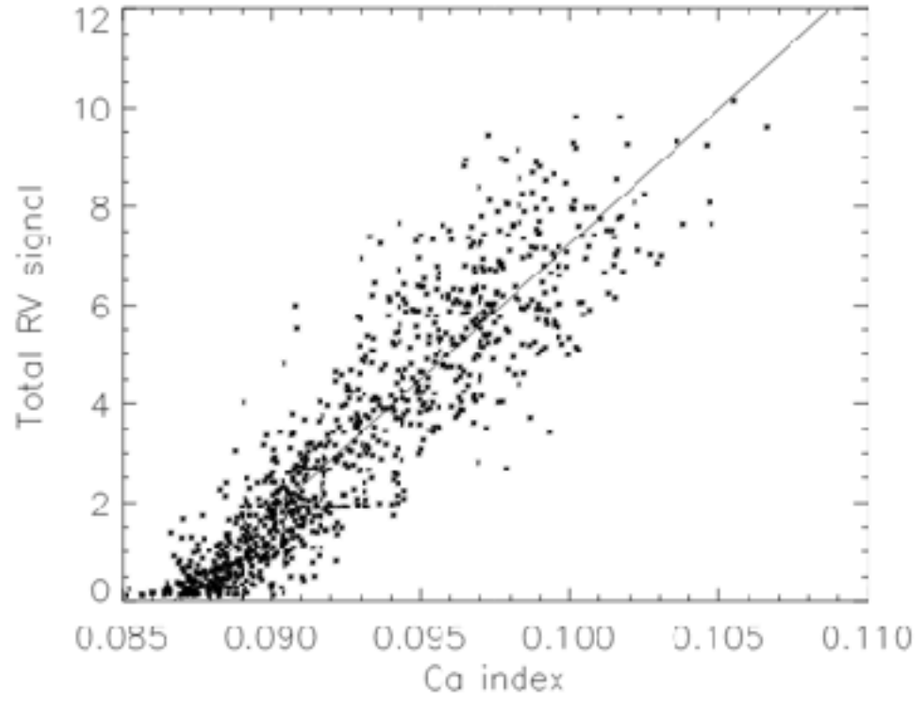

- On Sun data
- Main limit is convective noise
- Found to x10 larger than required to detect an Earth twin

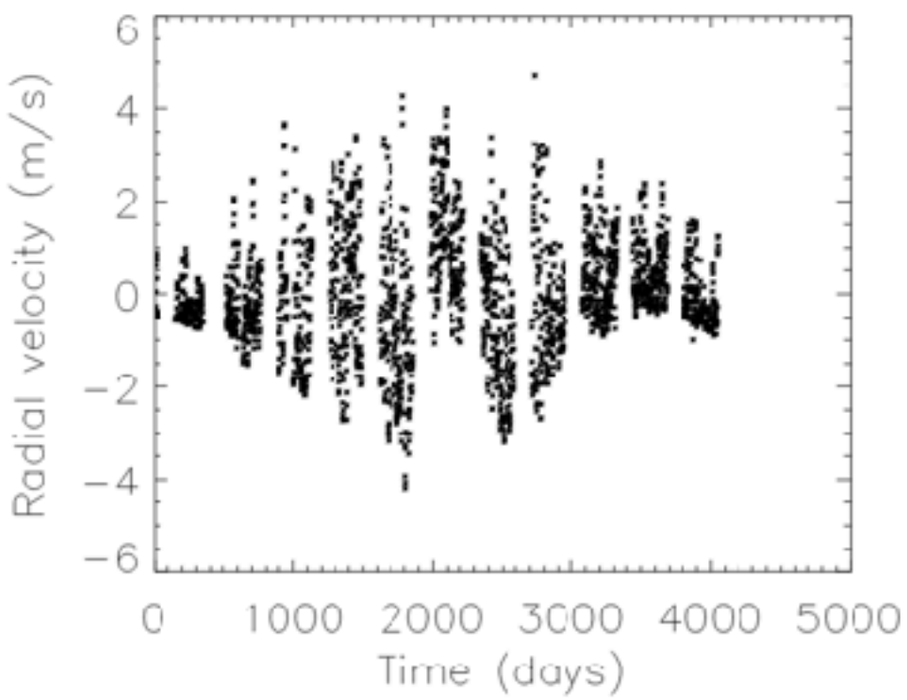

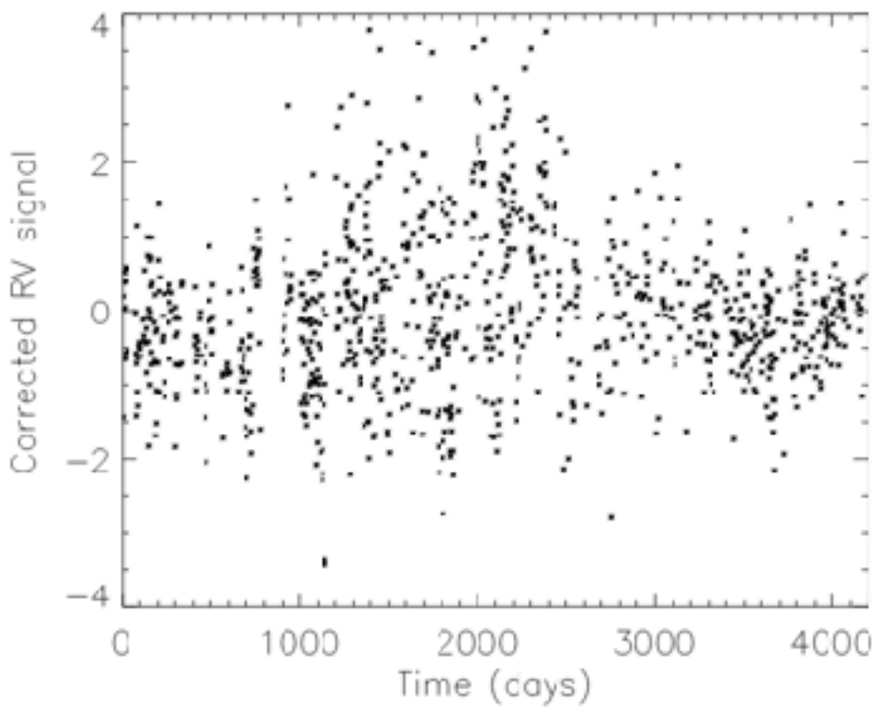

Meunier & Lagrange (2013);

Keplerian/sine fit

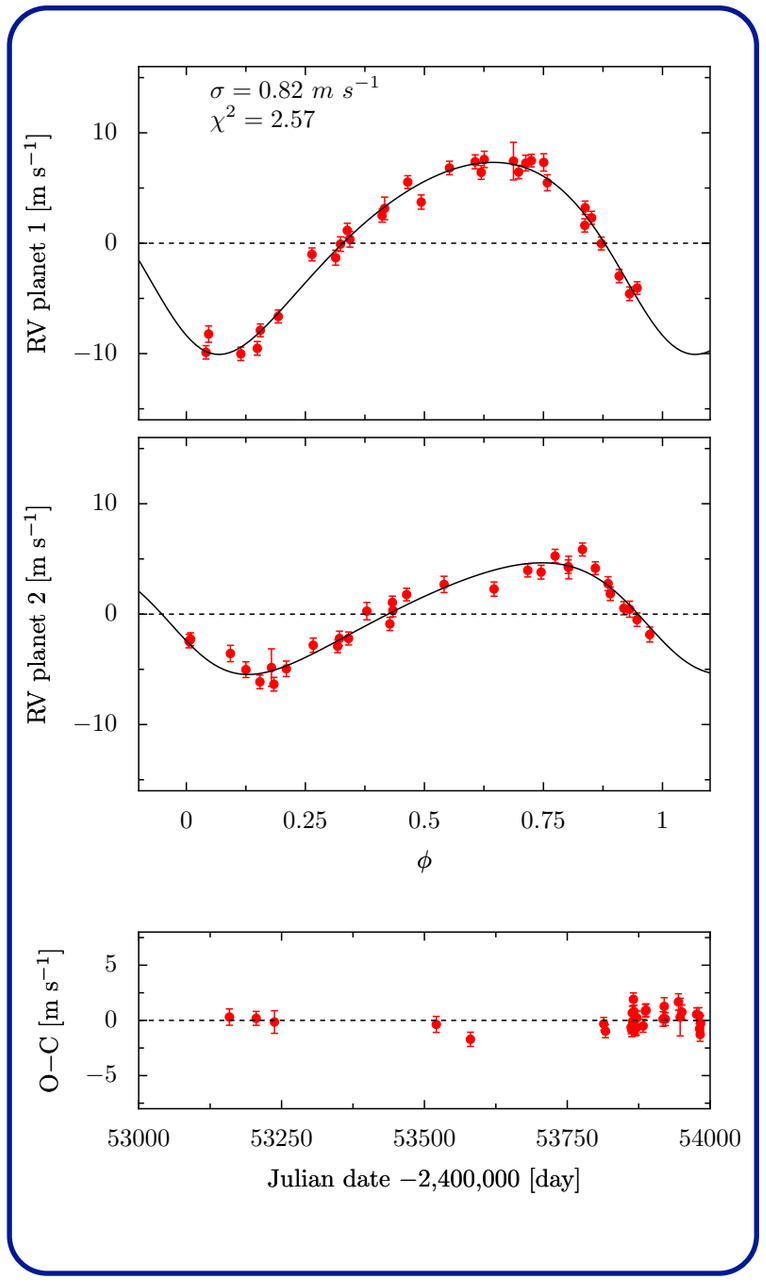

Bonfils et al. (2007)

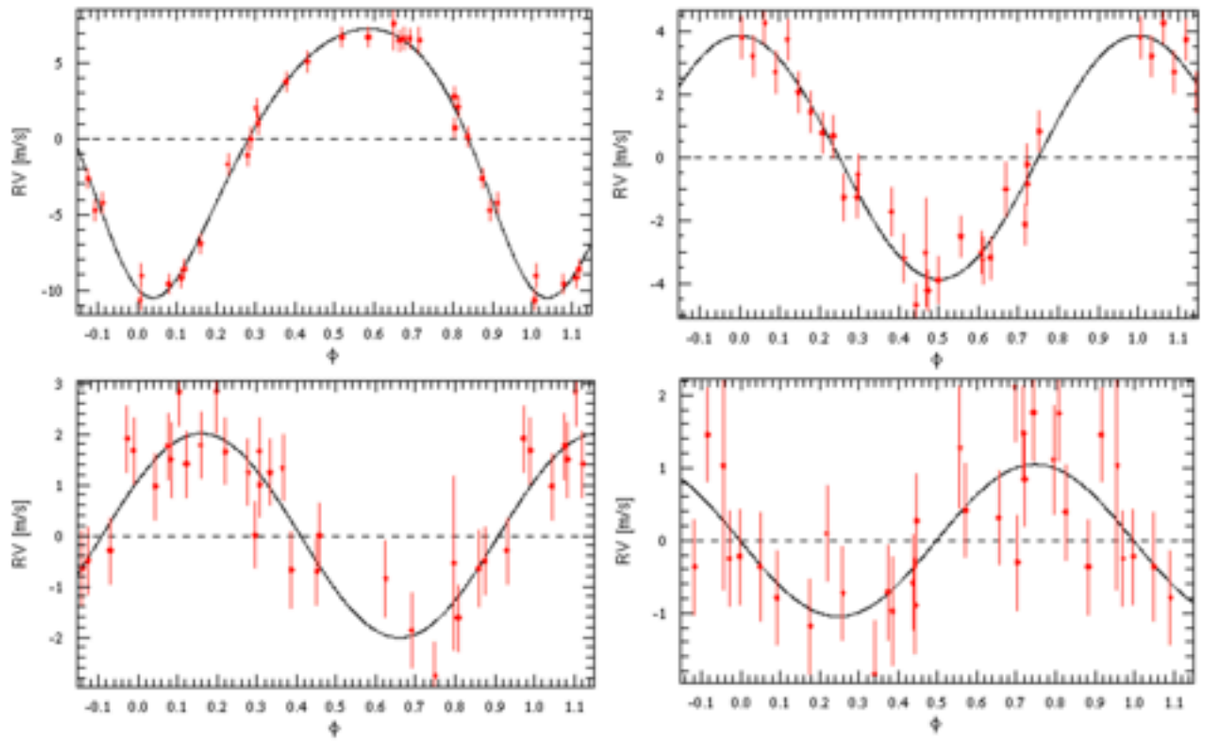

Fig. 16. Fit of the HARPS RV of GJ674 with one Keplerian and three sinusoids fixed to the rotational period (*top right* P_{rot} = 34.85d) and the two first harmonics (*bottom left* $P_{rot}/2$ = 17.425d and *bottom right* $P_{rot}/3$ = 11.6167d). The Keplerian fit (*top left*) gives the planetary parameters. Each plot is given as a function of orbital phase after removing the other three signals. Individual error bars are also plotted.

Boisse et al. (2011)

Floating chunks

THE ASTROPHYSICAL JOURNAL, 743:75 (11pp), 2011 December 10

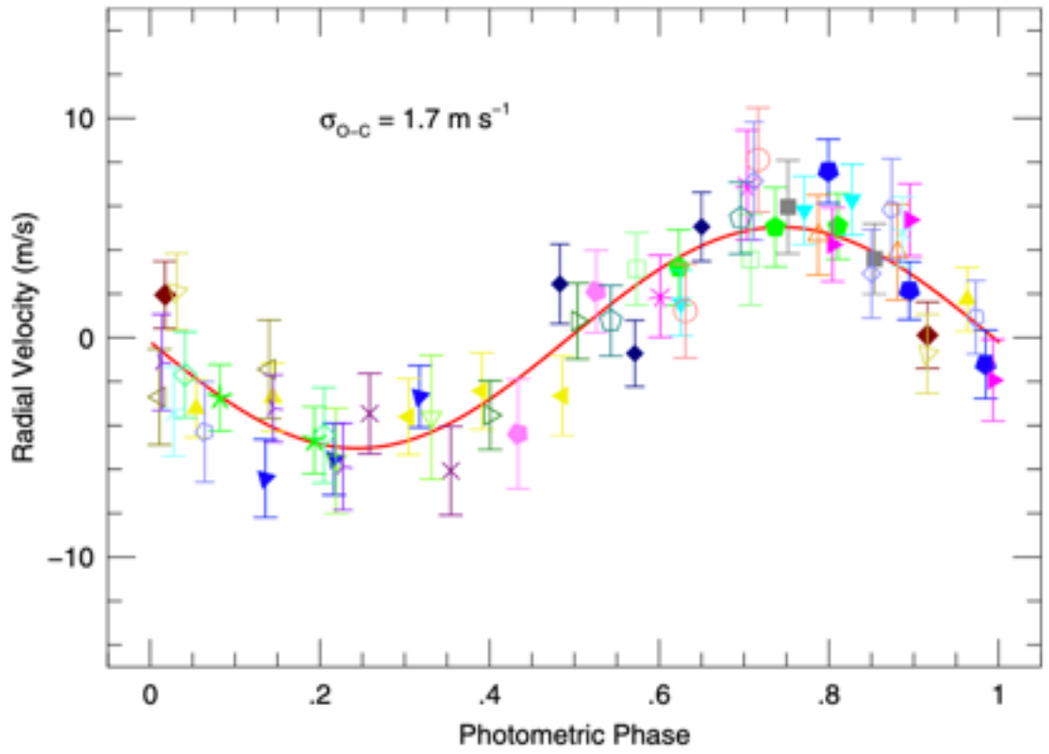

Figure 1. RV measurements for CoRoT-7b taken on the 27 nights listed in Table 1. On these nights, multiple observations were made separated by 2–4 hr. Values are phased according the CoRoT transit phase. Different symbols represent measurements for different nights. The line represents the orbital solution.

- Mass of CoRoT-7b
- One offset / night subtracted to filter RV change on time scales > 1 night
- Need multiple pets / night and a very short period orbit (!)

Hatzes et al. (2011); See also Hatzes et al. (2014); Dai et al. (2017)

Analytic modeling

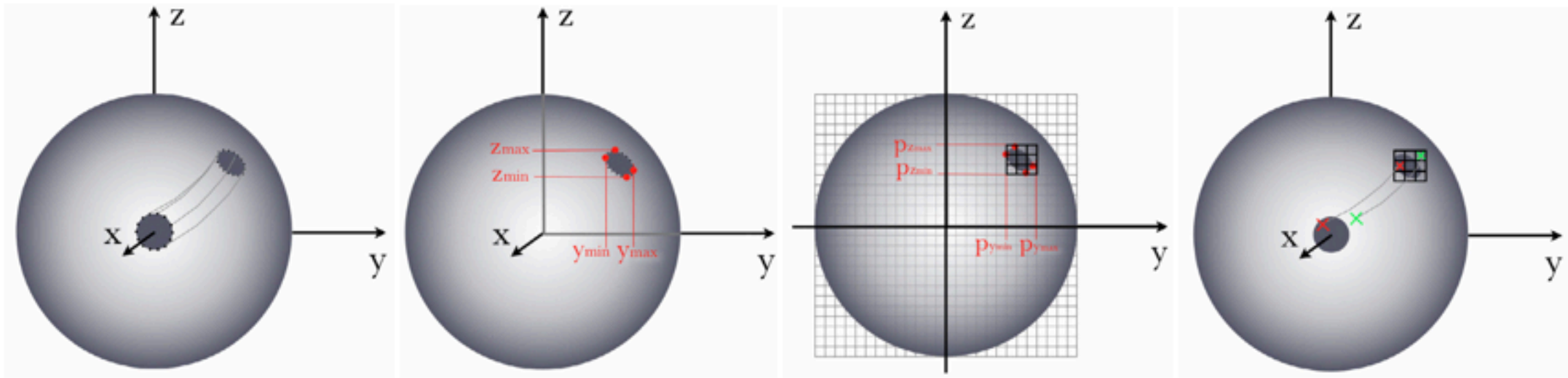

Fig. 4. *From left to right*: 1) according to the stellar inclination and to the spot's latitude and longitude, the *xyz* position of the *nrho* points on the spot's circumference are calculated in 3-D. 2) The maximum and minimum y and z determine a smaller area where the spot is. 3) These $\{yz\}$ positions (in 3D) are projected on the y-z plane, which gives (p_y, p_z) positions. 4) From these values, a smaller grid is defined. Each cell of this grid is scanned. A reverse to that performed in step 1 rotation is performed to establish if the cell is inside the spot or not.

Boisse, Bonfils & Santos (2012)

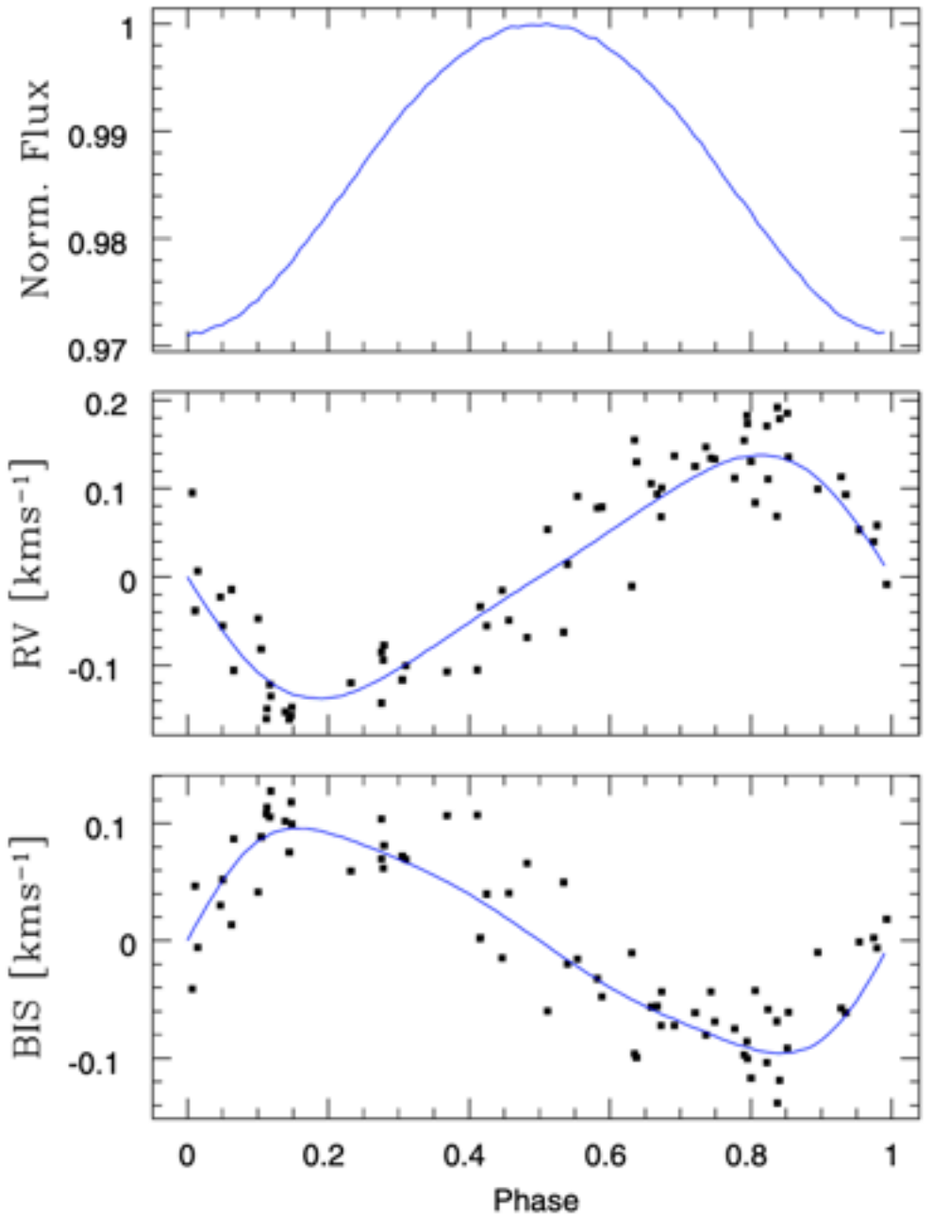

Fig. 11. SOAP simulation of a star with the same characteristics as HD 166435 observed with ELODIE with a spot of 2.02% of the stellar surface to reproduce the RV, BIS, and flux variations observed by Queloz et al. (2001).

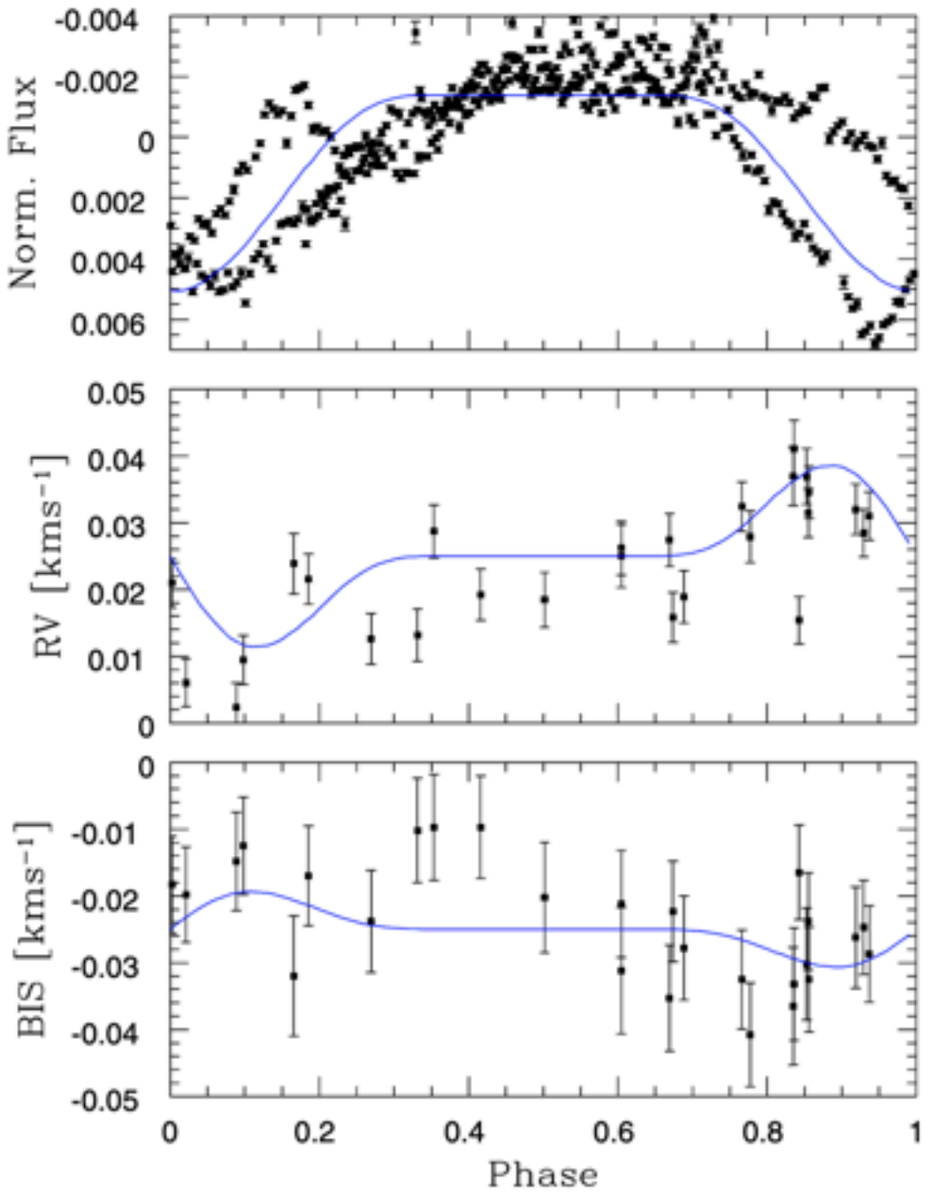

Fig. 12. In blue lines, SOAP simulation of a star with the same characteristics as HD 189733 observed with SOPHIE with a spot of 2% of the stellar surface to reproduce the RV, BIS, and flux variations observed by Boisse et al. (2009) (black data points).

Boisse, Bonfils & Santos (2012)

FF' method

Aigrain, Pont & Zucker (2012)

Fig. 2.10 The FF' method for a spot crossing the stellar disc. The RV variations induced by flux blocking ($\Delta RV_{\rm rot}$) and suppression of the convective blueshift ($\Delta RV_{\rm conv}$) are proportional to $F\,{\rm d}F/{\rm d}t$ and F^2, respectively Fig. By Haywood

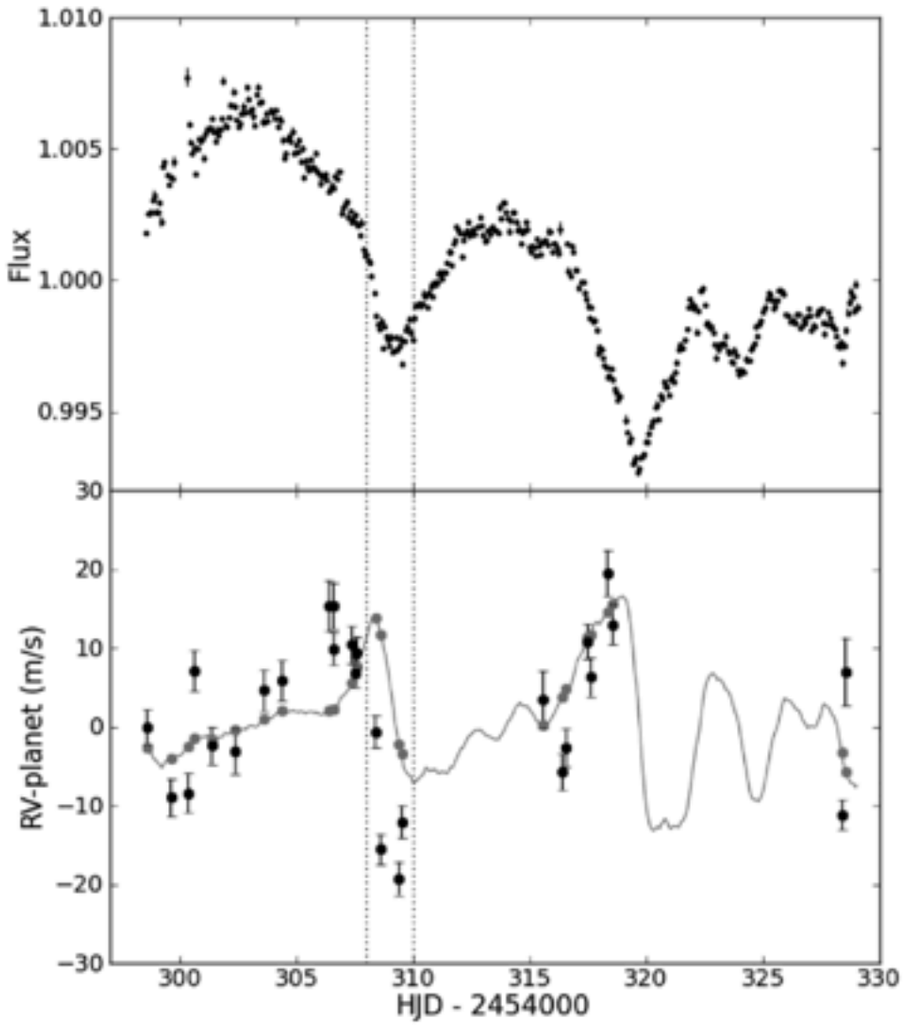

Figure 6. Photometry and RV time series for HD 189733. The *MOST* light curve (Boisse et al. 2009) is shown in the top panel and the observed and simulated RV data are compared in the bottom panel. The black dots with error bars show the SOPHIE data from Lanza et al. (2011) after removal of the best-fitting planetary signal, and subtraction of a constant 21.6 m s^{-1} offset. The grey line shows the RV curve simulated by applying the FF' method to the *MOST* light curve, and the grey dots show the same curve linearly interpolated to the sampling of the SOPHIE observations.

nature Vol 451|3 January 2008 doi:10.1038/nature06425

LETTERS

A young massive planet in a star–disk system

J. Setiawan[1], Th. Henning[1], R. Launhardt[1], A. Müller[1], P. Weise[1] & M. Kürster[1]

Visible

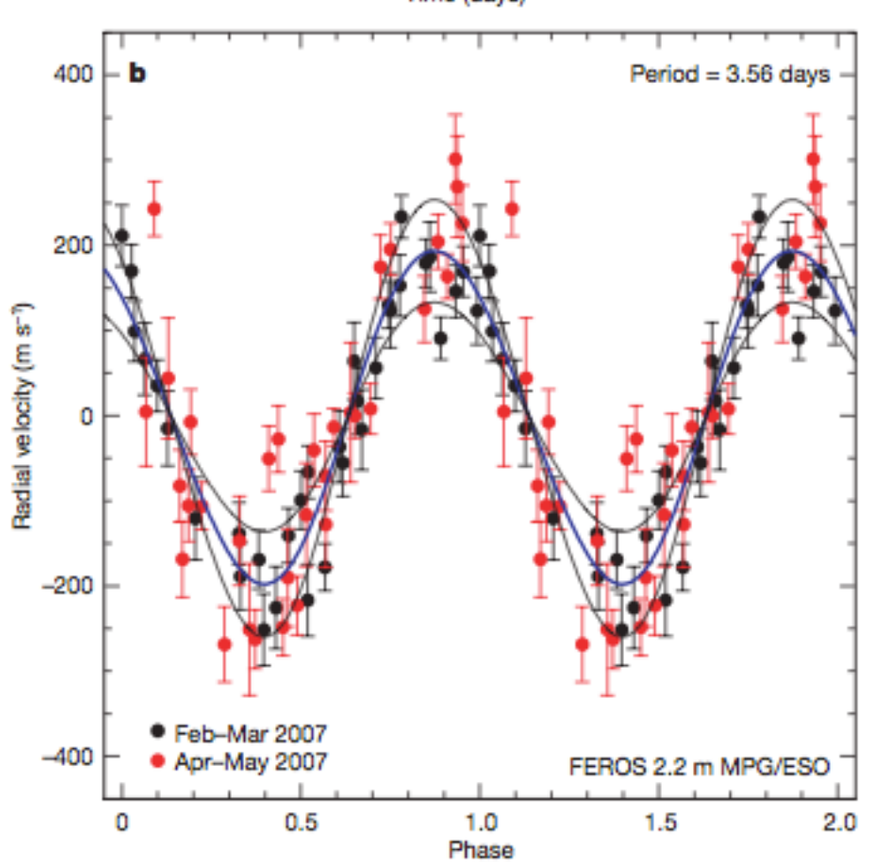

Figure 2 | Radial velocity variation of TW Hya. a, The RVs were obtained

A&A 489, L9–L13 (2008)
DOI: 10.1051/0004-6361:200810596
© ESO 2008

Astronomy & Astrophysics

LETTER TO THE EDITOR

TW Hydrae: evidence of stellar spots instead of a Hot Jupiter*

N. Huélamo[1], P. Figueira[2], X. Bonfils[3,4], N.C. Santos[3], F. Pepe[2], M. Gillon[2], R. Azevedo[3], T. Barman[5], M. Fernández[6], E. di Folco[2], E. W. Guenther[7], C. Lovis[2], C. H. F. Melo[5], D. Queloz[2], and S. Udry[2]

IR

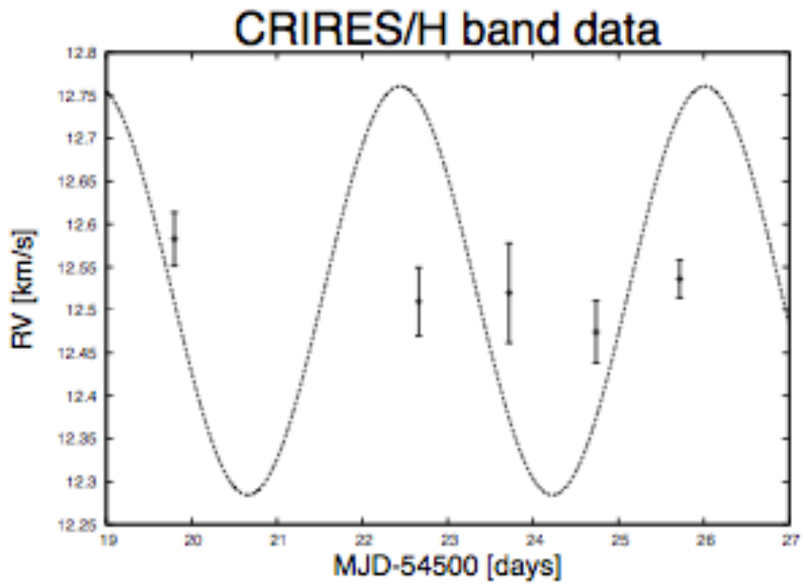

Fig. 4. CRIRES/*H*-band radial-velocity points overplotted on the fitted Keplerian function shown in Table 1. The error bars correspond to the quadratic addition of the errors bars on the RV standard and on TW Hya measurements.

(to mitigate RV-induced activity motivates new IR spectraograph, such as SPIRou)

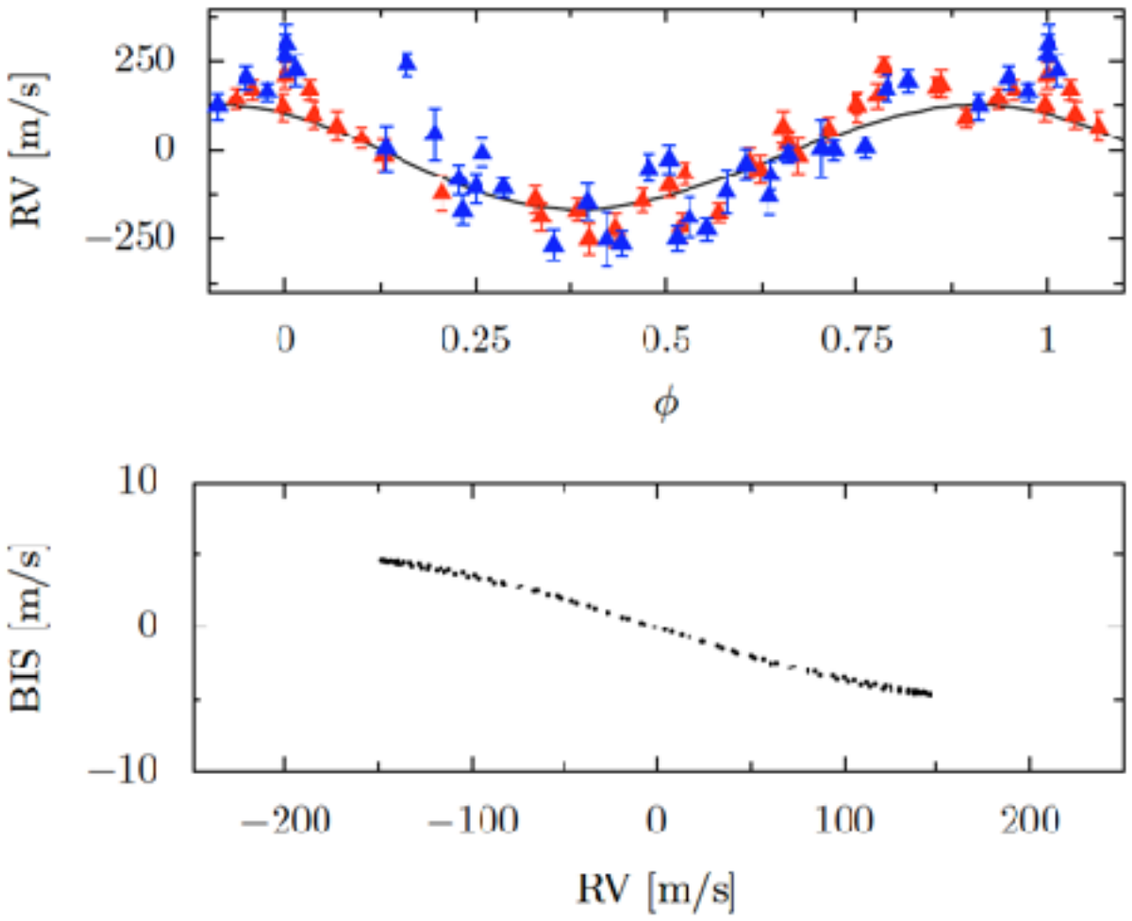
RV [m/s]
250
0
−250
0
0.25
0.5
0.75
1
ϕ
BIS [m/s]
10
0
−10
−200
−100
0
100
200
RV [m/s]

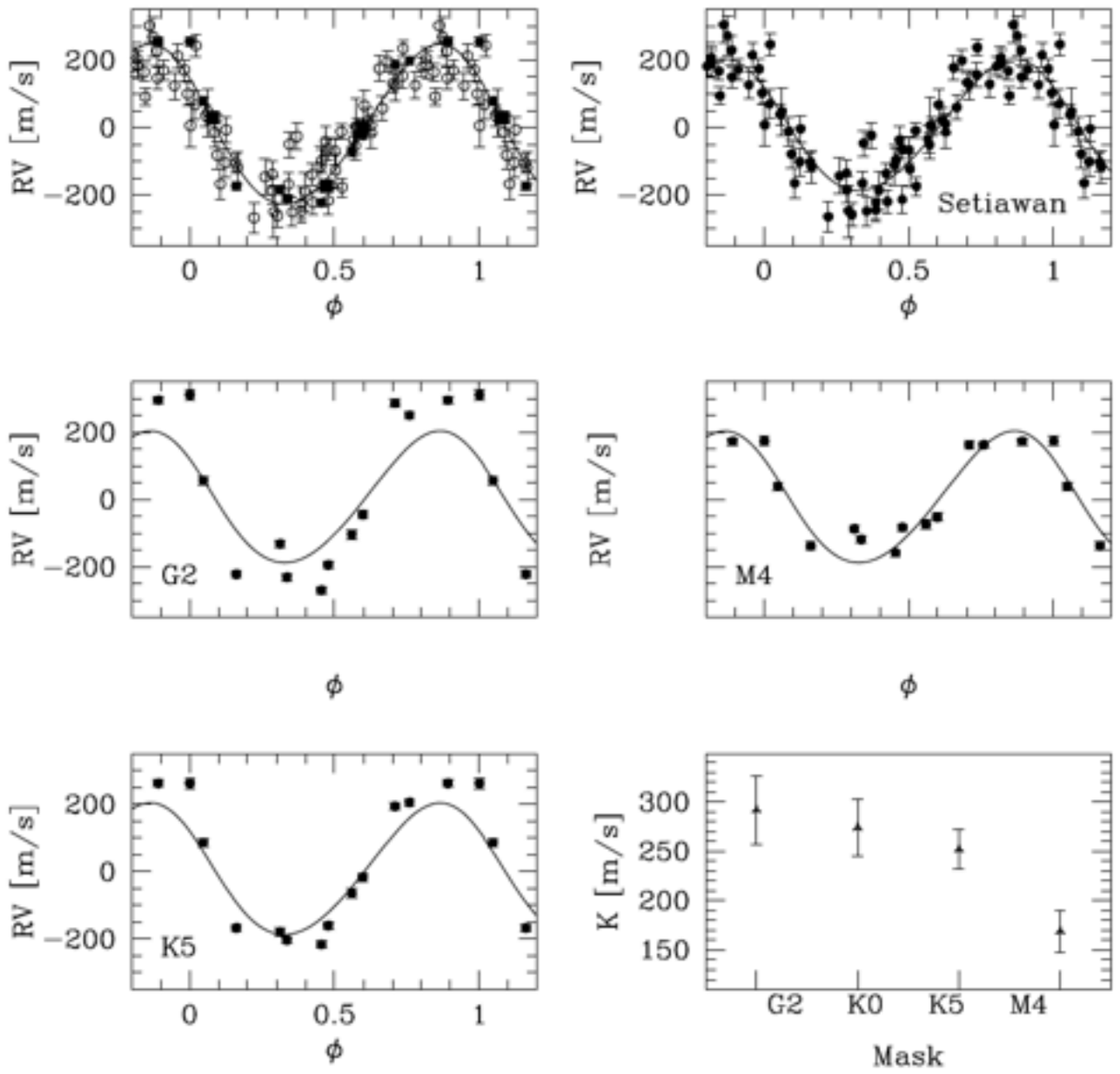
RV [m/s]
200
0
−200
0
0.5
1
ϕ
Setiawan
G2
M4
K5
K [m/s]
300
250
200
150
G2
K0
K5
M4
Mask

Gaussian Processes

$$\chi^2 = \sum_i \frac{(O_i - C_i)^2}{\sigma_i^2}$$

$$\chi^2 = r^T W r \qquad r = (O - C)$$

$$W = \begin{pmatrix} \sigma_1^2 & 0 & \cdots & 0 \\ 0 & \sigma_2^2 & \cdots & 0 \\ \vdots & \vdots & \ddots & \vdots \\ 0 & 0 & \cdots & \sigma_n^2 \end{pmatrix}$$

$$W = \begin{pmatrix} \sigma_1^2 & \sigma_{1,2} & \cdots & \sigma_{1,n} \\ \sigma_{2_1} & \sigma_2^2 & \cdots & \sigma_{2,n} \\ \vdots & \vdots & \ddots & \vdots \\ \sigma_{n,1} & \sigma_{n,2} & \cdots & \sigma_n^2 \end{pmatrix}$$

- Diagonal elements of the weight matrix correspond to uncorrelated noise
- Off-diagonal elements express the covariance between points
- >>N covariance values; cannot be free parameters
- GPs attempt to model the covariance matrix with a function (aka kernel) that has few free parameters

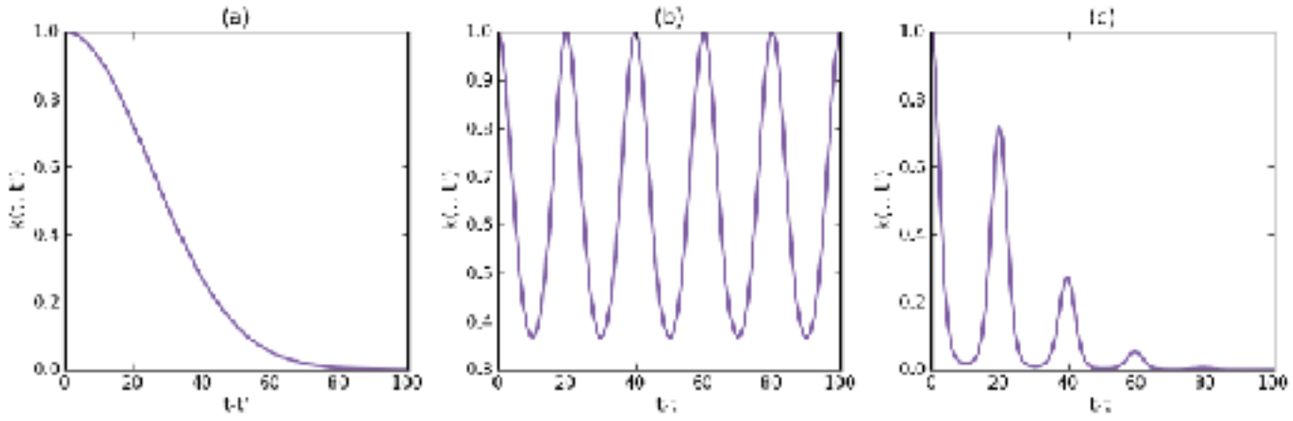

Figure 2.6: Different types of covariance functions: (a) square exponential, (b) periodic, and (c) quasi-periodic. The hyperparameters are: $\theta_1 = 1$, $\theta_2 = 35$, $\theta_3 = 20$, $\theta_4 = 0.5$.

$$k_4(t, t') = \theta_1^2 \cdot \exp\left[-\frac{(t - t')^2}{\theta_2^2} - \frac{\sin^2\left(\frac{\pi(t-t')}{\theta_3}\right)}{\theta_4^2} \right].$$

Haywood (2015)

GPs

- Prox Cen
- Espresso
- Anchored on FWHM

Suarez Mascareno et al. (2020)

Xavier Bonfils

Polarimetry

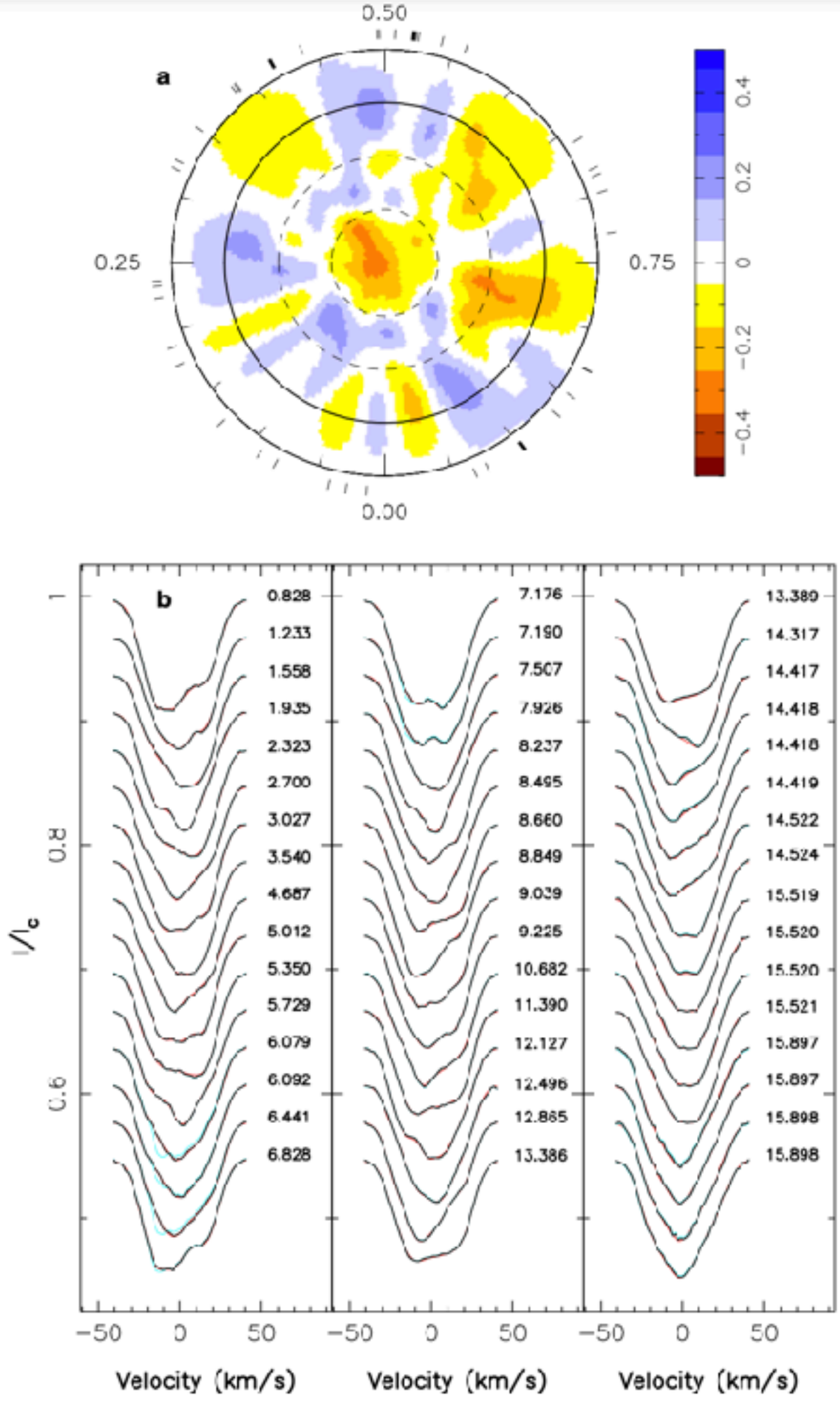

- Tomography
- Surface brightness => dRV
- e.g. young T-Tauri V830 Tau

Donati et al. (2016)

Xavier Bonfils

Polarimetry

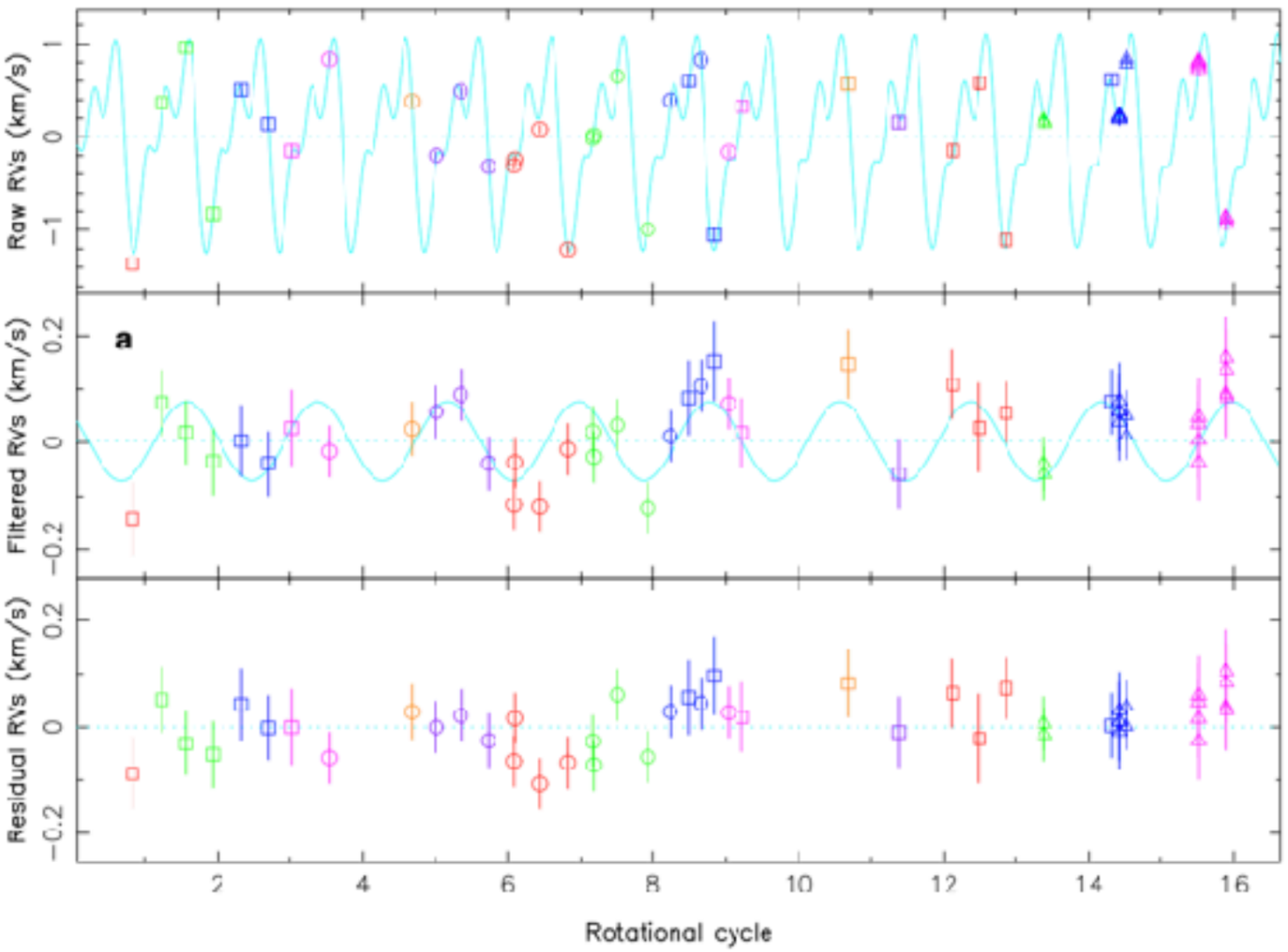

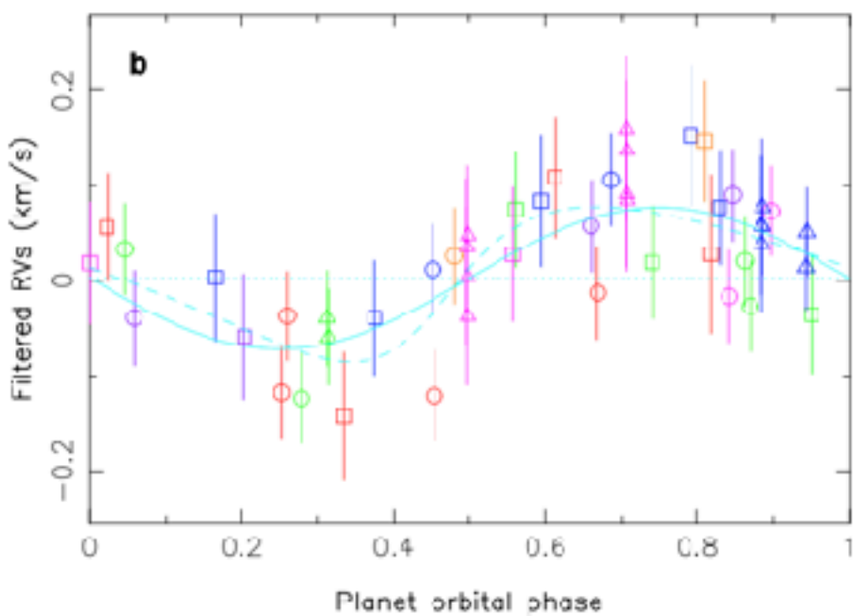

- Tomography
- Surface brightness => dRV
- e.g. young T-Tauri V830 Tau
- And its hot Jupiter
  P=5d; Mp=0.7Mjup

Donati et al. (2016)

See also Klein et al. (2020) with AU Mic b

Xavier Bonfils

|B| + FF'

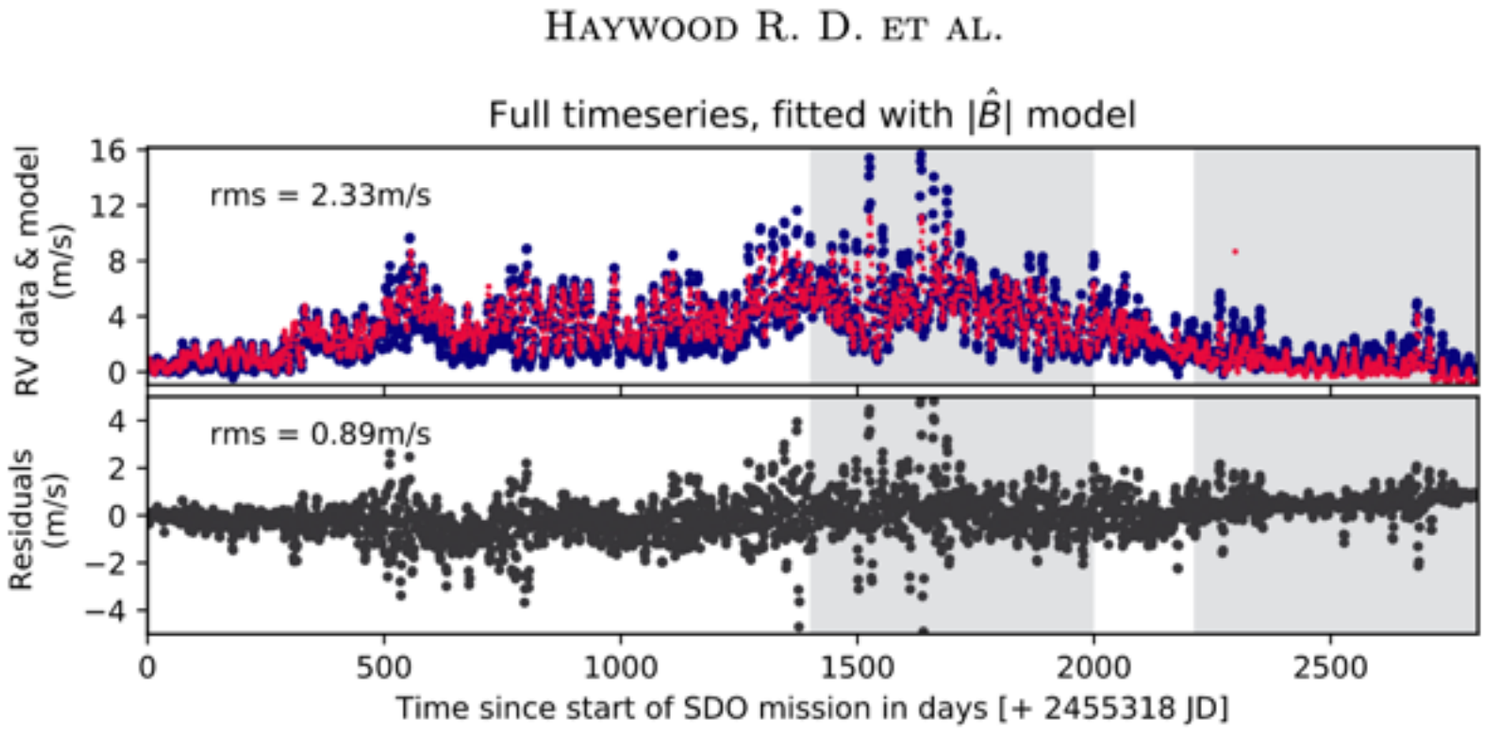

$$\Delta\ RV(t) = \alpha \frac{|\hat{B}_{\rm obs}|(t)}{\langle|\hat{B}_{\rm obs}|\rangle} + RV_0$$

- Observation of the Sun
- SDO/HMI data
- /w oscillation nor granulation
- $B_\odot \sim 20$ Gauss
- Feasible for other stars ?

Haywood (2020)

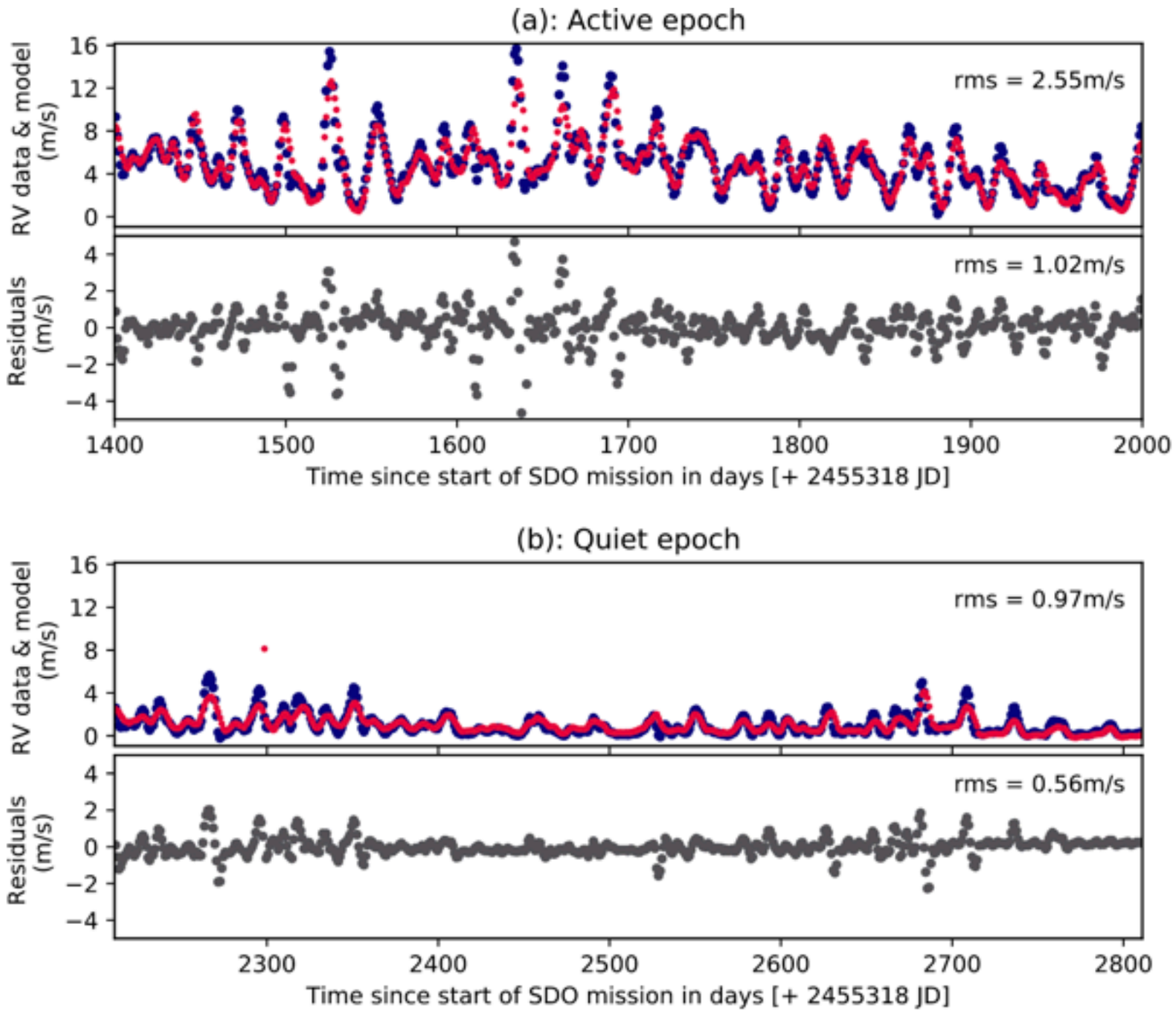

$$\Delta\ RV(t) = \alpha \frac{|\hat{B}_{\rm obs}|(t)}{\langle|\hat{B}_{\rm obs}|\rangle} + RV_0$$

- Observation of the Sun
- SDO/HMI data
- /w oscillation nor granulation
- $B_\odot \sim 20$ Gauss
- Feasible for other stars ?

Haywood (2020)

Take home

Searching planets around lower-mass stars probes a different outcome of the planetary formation

The signal to detect is often (much) larger that of lower mass stars

But so is the photon noise !

The true S/N advantages depends on the level of systematics.

Stellar activity is a chief concern.

Mitigation strategies is one of the most active topic of this field; with various (successful) strategies.